Experimental and Numerical Study of Axial-Feed Hot Gas Tube Forming of Polypropylene

Experimental and Numerical Study of Axial-Feed Hot Gas Tube Forming of Polypropylene

By

Galini Gavrilidou, B.Eng

A Thesis
Submitted to the School of Graduate Studies
in Partial Fulfillment of the Requirements
for the Degree
Master of Applied Science

McMaster University

MASTER OF APPLIED SCIENCE (2007) McMaster University

(Mechanical Engineering) Hamilton, Ontario, Canada

TITLE: Experimental and Numerical Study
of Axial-Feed Hot Gas Tube Forming of Polypropylene

AUTHOR: Galini Gavrilidou, B.Eng
(Azerbaijan State Oil Academy, Baku)

SUPERVISOR: Dr. Mukesh K. Jain
Department of Mechanical Engineering
McMaster University

NUMBER OF PAGES: xxi, 130

ABSTRACT

Polymeric materials have attracted a lot of attention for the past several decades. Different sectors of manufacturing industry, such as packaging, building and automotive industry have introduced polymeric materials in their applications. Common polymer manufacturing processes include thermoforming and blow molding.

In this research, characteristics of a new polymer manufacturing process, referred to as axial-feed hot gas tube forming (HGTF) are studied. Experimental studies were conducted to form a simple axisymmetric component from extruded polypropylene (PP) tube by varying several key process parameters such as internal pressure, temperature and axial feed. Tube shape and deformation characteristics were studied as a function of the above process parameters.

In addition, two constitutive material models have been utilized for finite element simulation of axial-feed HGTF of PP tube using a commercial FE code. One of them is conventional hyperelastic Ogden material model and another is more advanced viscoelastic-viscoplastic Augmented Hybrid material model (AHM), that has been recently developed. Simulation results from two models were analyzed and compared with the experimental results and good general agreement has been obtained. Results showed that application of more advanced AHM material model led to improved prediction of part shape and strain distribution over the part profile.

ACKNOWLEDGEMENTS

In presenting this thesis, I wish to express my gratitude to my supervisor, Dr. Mukesh Jain for his continuous guidance and support throughout this research, whose great enthusiasm and patience inspired me to pursue graduate work in this area.

I also wish to express my sincere appreciation to following individuals and organizations who have helped in its completion:

Dr. Jorgen Bergstrom from Veryst Engineering LLC for providing the User Material Subroutine and continuous collaboration and support throughout this research.

Dr. Don Metzger for the advice and guidance with finite element analysis in earlier stages of present work.

Dr. John Vlachopoulos from Department of Chemical Engineering and Dr. John MacGregor from Advanced Control Consortium for their interesting suggestions and comments, that gave me different perspectives on research improvement.

Dr. Mike Bruhis for his valuable assistance in carrying the experimental part of this research.

My contacts in industry: Keith Ward from Decoma International Inc. and Yihai Shi from Novelis Global Technology Centre, for their help with the experimental facilities and data collection as well as FE modeling work.

I would also like to thank my friends and colleagues Alexei Nikandrov and Young Suk Kim for their help with FE modeling and computer software.

Lastly, I would like to acknowledge the continuous support and encouragement from my family, who made the completion of this work possible.

Table of Contents

List of Figures

List of Tables

Nomenclature

$\bar{\lambda}^p$	Effective chain stretch backstress network
$\dot{\gamma}^p$	Plastic flow rate
$\dot{\gamma}_0$	Pre-exponential factor
$\dot{\gamma}_B$	Magnitude of plastic flow rate of network B
$\dot{\gamma}_B^{\mathrm{v}}$	The rate of viscoplastic flow of the time dependent network B
$\dot{\gamma}_i$	Combined pre-exponential factor
$\hat{\varepsilon}$	Reference scalar effective strain
κ_A	Bulk modulus
λ^e	Second Lame's constant
λ_B^p	Effective chain stretch of the viscous component of the deformation of network B
λ_{lock}^p	Locking chain stretch of network A
λ_1, λ_2, λ_3	Deviatoric stretches
λ_A^{lock}	Locking chain stretch of network A

μ	Coefficient of friction
μ^e	Second Lame's constant
μ^p	Shear modulus of the backstress network
μ_0	Initial shear modulus
μ_A	Initial shear modulus of network A
μ_k	Coefficient of friction (kinetic)
$\overline{I}_1$	The first deviatoric strain invariant
$\overline{I}_2$	The second deviatoric strain invariant
$\phi(x)$	Distribution function for activation energies
τ	Shear stress
τ_B^{base}, m_B	Material parameters
τ_C^{base}	Material parameter
τ_C	The effective shear stress
τ_{base}	Reference shear stress
$\mathbf{B}^p$	Distortional portion of the left Cauchy-Green tensor of the backstress network
$\mathbf{B}_B^p$	Finger tensor of the plastic part of of network B
$\mathbf{B}^*$	Distortional portion of the left Cauchy-Green tensor
$\mathbf{E}^e$	Logarithmic strain
$\mathbf{T}$	Cauchy stress (true stress)

$\mathbf{T}^*$	Tensorial stress driving plastic force
$\mathbf{T}^p$	Backstress
$\mathbf{T}_N$	Nonlinear elastic process associated with the deformation of the crystalline phase
$\mathbf{T}_{12}$	Strain energy function
$\mathbf{T}_{8chain}$	Eight chain model
θ	Absolute temperature
ε	Scalar effective strain
A	Shear activation volume
C	Strain exponential factor used in the BB model
C_{10}, C_{01}	Temperature-dependent material parameters
D	Tube diameter
D^p	Deviatoric stretching tensor of the backstress network
d_0	The outer diameter
d_1	The final tube diameter
D_c	Coefficient of compressibility
E_i	Shear modulus
F	Deformation gradient
F^e	Elastic part of the deformation gradient
F^p	Plastic part of the deformation gradient

F_a0	The initial axial force
F_a1	The subsequential axial force
F_B^e	Elastic deformation gradient of network B
F_e	Maximum compressive end force
F_f	Opposing frictional force
J	Volume change
J^e	Elastic volumetric change
J^{el}	The elastic volume ratio
K_0	The initial bulk modulus
k_B	Boltzmann's constant
L	Tube length
L_B^v	The velocity gradient of the viscoelastic flow of the backstress network
m	Stress exponential parameters
m_C	Material parameter
n	Chain density
P_a	Internal pressure
p_B	Material parameter specifying the transition rate of the distributed yielding event
p_f	The forming pressure
q_A	Material parameter

R_m	The tensile strength
s	Thermal shear resistance
s_0	The tube initial wall thickness
s_B	Dimensionless material property parameter
s_{Bf}	The final value of s_B reached at fully developed plastic flow
T	Material thickness
T_B	Cauchy stress of network B
T_C	The stress acting on the relaxed configuration convected to the current configuration
U	The strain energy per unit of reference volume
U_{TS}	Material ultimate tensile strength
V^e	Elastic left stretch tensor
w	Midpoint of the activation energy distribution
p_{i_j}	Internal pressure at point j

Chapter 1

Introduction and Objectives

1.1 Introduction

The automotive industry is a promising new sector for polymer applications after packaging, building and civil engineering. The automotive manufacturers have been quite successful in applying the polymeric materials to car manufacturing. The automotive parts that widely utilize polymers are instrument panels, dashboards, under the hood component, console and car exterior parts. For production of those parts, common polymer forming processes such as thermoforming and blowmolding are used (See Sections 2.2.1 and 2.2.2).

However, polymer use as structural components in cars has been limited. Many of the automotive components are presently being made from seam welded steel tubes via metal forming techniques such as hydroforming or hot gas forming (See Sections 2.2.3 and 2.2.4). However, to create lighter vehicles, automotive manufacturers have been turning to aluminum and polymers. Hot gas forming of polymer tubes is a promising new area to extend the application of high strength polymers to automotive structural

components. In particular, hot gas forming of polymer tubes into bumper beams can offer substantial saving in weight and simplify the manufacturing process. Also, plastic components may be able to attain forming strains higher than steel or aluminum thus offering more freedom in designing the parts. The example is Cadillac's new XLR, the plastic luxury car (see Figure 1.1). The entire car body is made almost completely of plastic, except the aluminum panel behind the convertible top.

Figure 1.1: Cadillac [1]

Axial-feed HGTF of polymer tube is a new technique and has been under development at McMaster University for the past three years. A system of axial feeding, rapid heating and cooling of dies has been developed to form simple shapes from polymer tubestock. In addition to investigation of forming behavior of extruded PP tubes during axial-feed HGTF, effect of depressurization (or unloading) in conjunction with cooling of the final part has been under investigation.

1.2 Objectives of Present Research

The objective of the present research is to carry out systematic experimental studies of axial-feed HGTF process as well as to model the axial-feed HGTF for extruded polypropylene (PP) tubes via the Finite Element(FE) method. Development of the

suitable FE model is very important, because it gives a better understanding of the process, material flow behavior, part, die and process design. It eliminates the need for a large number of experimental trials to optimize the process and can be used to establish a process window for good quality parts.

The specific objectives of the present research are:

1. Experimental study, to relate process variables to part characteristics.
2. Development of FE models of axial-feed HGTF process for the PP tube with suitable material constitutive models.
3. Assessment of the role of process variables on tube deformation characteristics and particularly the part thickness uniformity.
4. Comparison of FE simulations results from two different material models with experiments (thickness and strain distribution in the part).
5. Investigation of the effect of part unloading via an advanced material model in the FE simulations of axial-feed HGTF process.

The organization of the thesis is as follows; a literature review of the previous work on the polymer forming processes in general, as well as on the finite element simulation of the forming processes is presented in Chapter 2. Experimental setup and procedure is described in Chapter 3 and the results are presented in Chapter 4. Development of the FE models with Ogden and Augmented Hybrid material model formulations are explained in Chapter 5. Results and comparisons of various FE simulations from different material models with experiments are presented in Chapter 6. A comparison of numerical simulations results with experiments is discussed in Chapter 7. Conclusions and recommendations for the future work are given in Chapter 8. This is followed by References and Appendices.

Chapter 2

Literature Review

2.1 Introduction

In the last several decades, there has been an increasingly rapid growth of the polymer applications. The advantages of the polymers as a light weight, low cost materials, have attracted the attention of different industries. Nowadays, the polymers are widely used in industries such as automotive, packaging, food etc. The most widely used polymer forming processes are thermoforming and blow molding. The processes of polymer forming in most cases utilize the polymers in the near molten state.

Recently, a lot of attention had been drown to the solid state forming of polymers. One of the processes that has the ability to form the polymeric tube material to the required shape is hot gas forming. Hot gas forming is similar to room temperature water-based hydroforming that is widely used in the metal forming operations. An axial feed hot gas forming process has been developed at McMaster that combines axial feeding of the ends of the tubes, similar to hydroforming and employs hot gas in place of water, a method similar to thermoforming and blow molding. In this chapter,

a review of several topics related to the objectives of the present work, including the hot gas forming process, is briefly presented.

2.2 Related Polymer and Metal Forming Processes

There are a wide variety of the forming operations that have been successfully employed in industry and have been broadly introduced in literature. The research done on forming operations and introduced in this chapter is divided into polymer forming operations and metal forming operations. Polymer forming operations studies in thermoforming and blowmolding, mostly carried out by researchers in chemical processing engineering, are introduced in subsections 2.2.1 and 2.2.2. The research done on metal forming operations, such as hydroforming and hot gas forming is introduced in subsections 2.2.3 and 2.2.4.

2.2.1 Thermoforming

Thermoforming is a process of shaping plastic articles onto a male or into a female mold out of softened thermoplastic sheet [2]. The process consists of two stages. The first stage is heating the plastic sheet to the condition where is it soft and flow easily into a mold. The second stage is stretching the softened sheet against a cool mold surface. After touching the cool mold surface, the sheet cools rapidly and retains the shape of the mold.

Thermoforming behavior of PP was introduced with the two techniques for the food containers production [3]. These techniques include in-line melt phase thermoforming from hot sheet preform and solid phase thermoforming from cold sheet preform. High pressure and twin-sheet thermoforming are two recent advances to these pro-

cesses described in [4]. A hydraulic table-locking system is utilized to generate such high forces. Another interesting process named Thermo-And-Blow Forming (TAB Forming) is introduced in [5]. The process is developed to improve the twin-sheet thermoforming products. The process consists of two phases. The first phase is pre-welding the twin sheets. The second phase is heating and blowing the welded sheets into the desired mold shape. The final hollow part has a higher wall stiffness and rigidity compare to the conventional twin-sheet thermoforming products.

The advantages of thermoforming are that it utilizes only a single surface mold and relatively inexpensive mold materials. In addition, because thermoforming utilizes sheet material, there is no need for plastic to "flow" from one point to another, thus parts can be produced with a very high surface-to-thickness ratio. The disadvantages are that thermoforming begins with extruded plastic sheet, which adds the extrusion step into the process, and raises the production costs of the final part. Also, because thermoforming is "one-sided" process, the sheet during the process yields a part with a non-uniform wall thickness distribution.

The basic thermoforming operation involves simply heating the sheet and forcing it (stretching) against a mold. The heating and stretching consists of drape, straight vacuum and free forming. The illustration of straight vacuum forming is presented in Figure 2.1. In straight vacuum forming a thermoplastic sheet is heated in the mold to a temperature above its glass transition temperature and then quickly "inflated" into a mold cavity [6].

Although the basic thermoforming operations are simple and offer an easy way to form a plastic part, they yield locally unacceptable part wall thicknesses. To improve the uniformity of the thermoformed part, assisted thermoforming has been utilized. Assisted thermoforming consists of non-uniform heating, pneumatic preforming and

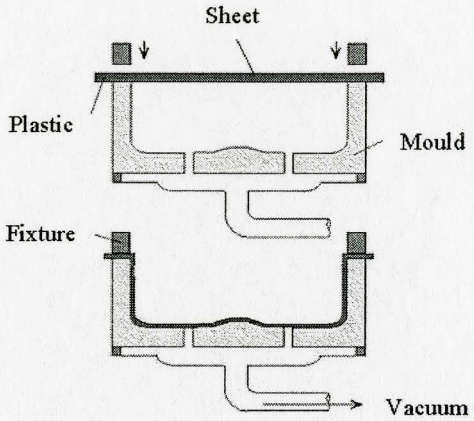

Figure 2.1: Straight vacuum thermoforming process [7]

plug assist thermoforming. In these operations, non-uniform or zonal heating, pre-stretching of initial material sheet and plugs of different shapes are used to achieve the maximum obtainable uniformity of the final part. The more advanced thermoforming techniques are twin-sheet forming, contact forming and diaphragm forming. In twin-sheet forming both sheets are clamped in a single frame with a blow pin between them. While heating, the space between the sheets is pressurized to keep them apart. Then the top sheet is formed into the top half of the mold and the bottom sheet is formed into the bottom half of the mold. After the sheets take the shapes of the mold, they are brought together to form the hollow or semi-hollow part.

In contact forming, very thin plastic sheets are heated by direct contact or trapped sheet heating. In place of heaters, non-stick metal surface contact heaters are used. The sheet can contact either one or two heated surfaces. In diaphragm forming, a diaphragm is used to support the hot sheet material. The diaphragm is usually a high-temperature rubber material such as neoprene. With this type of thermoforming operation, the uniformity of final part wall thickness is most acceptable.

2.2.2 Blow Molding

Blow molding is one of the most common plastic processing techniques. Blow molding is a method of forming hollow, thin wall articles out of thermoplastic materials. In the last two decades, blow molding has experienced a rapid growth due to an increased usage of molded parts in the new applications in automotive, transportation and packaging industries.

Blow molding is a process for producing hollow objects primary from thermoplastic materials [8]. Blow molding provides several advantages in the process of plastic part manufacturing. These include the possibility of reentrant curves (irregular), low stresses, possibility of variable wall thicknesses, and relatively low cost factors. Using blow molding it is possible to produce walls with thickness comparable to the thickness of a sheet of paper [8]. A typical blow molding process chart is shown in Figure 2.2.

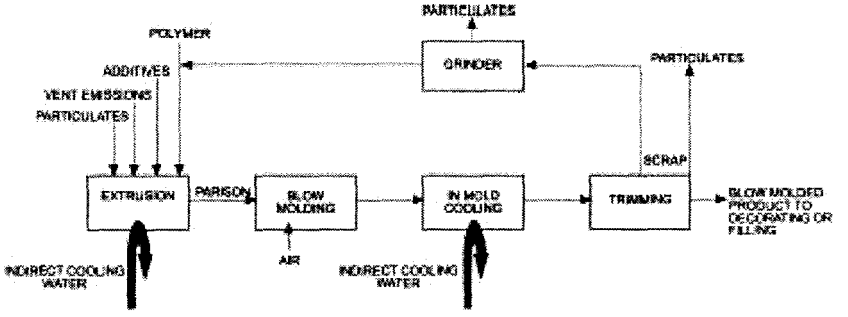

Figure 2.2: Blow molding process chart [9]

The process of blow molding can be described as follows. First, the original plastic perform or parison (a tube) is placed into a closed two-plate mold. The mold cavity represents the outside shape of the part to be produced. Then, air is injected into the heated parison to blow it out against the mold cavity. Finally, the expanded parison

is cooled, the mold is opened and the rigid blow molded part is removed. As material touches the chilled mould surface, it is quickly solidified, and the part maintains its formed shape as shown in Figure 2.3.

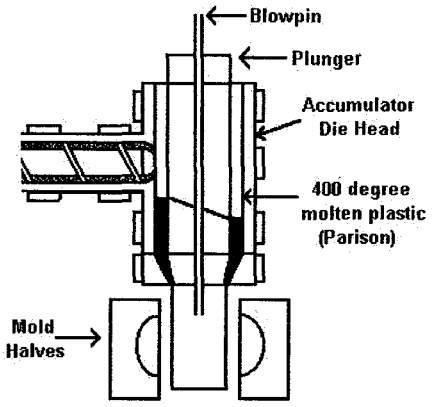

Figure 2.3: Blow molding process [10]

There are three main categories in the blow molding techniques: extrusion blow molding process that principally uses unsupported parison, injection blow molding process that uses a parison supported on a metal core pin and stretch blow-molding process. In extrusion blow molding, a parison is formed by an extruder. Various techniques are used to insert a parison into the die. It can be accomplished through the extrusion die mandrel, through a blow pin over, through blow heads applied to the mold and through the blowing needles which pierce the parison. In injection blow molding, there are three stages of operation. In the first stage, melted plastic is injected into a mold cavity to shape a preform parison. In the next stage, the air is blown into the parison to conform it to the shape of the part. The last part is ejection of the final part from the core rod. In stretch blow molding, the extrudate is biaxially stretched before it is chilled in the mold. This process aligns the molecules along two planes and provides an additional strength to the final part. This allows the use of lower material grades or thinner wall thickness.

Disadvantages of blow molding primarily include a high recycling scrap rate and limited wall thickness control or material distribution [8].

2.2.3 Tube Hydroforming

Tube hydroforming (THF) is a forming process in which a metallic tube is formed to the desired shape by expanding through the application of internal pressure. The internal hydraulic pressure is usually coupled with axial feeding of the tube in order to form complex shapes with small radii, to make the tube tight and pull the material into the forming zone (especially for the tubes with the small wall thickness) and to reduce the tube wall thinning. There are different types of hydroforming applications. A summary chart with various types of hydroforming processes is shown in Figure 2.4.

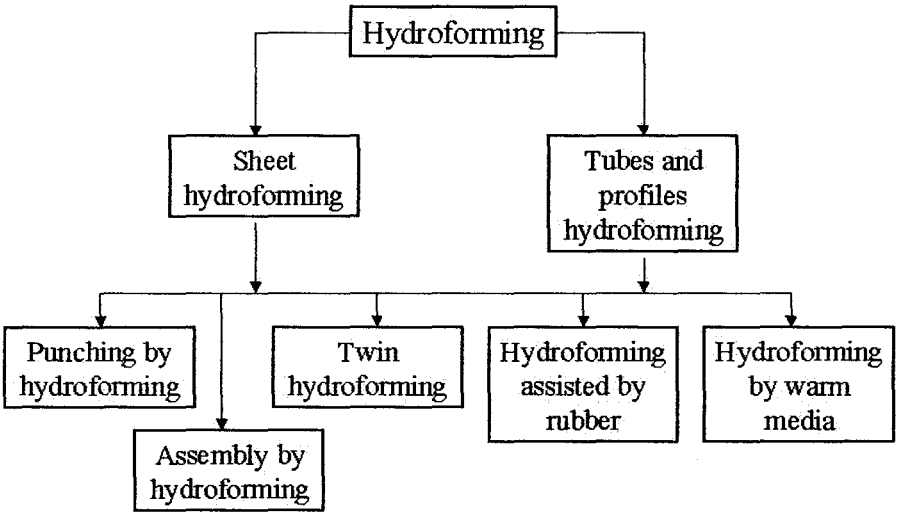

Figure 2.4: Hydroforming processes [11]

THF has been well known and widely used industrial application for more than a decade. However, the theoretical background and development of the techniques can be traced back to 1940. Between 1950 and 1970, America, England and Japan had

developed related patents and had been leading the research in this area. From 1970, Germany took a leading role in this area and applied the THF to produce structural auto parts for automotive industry [12]. Hydroforming research and practical applications are summarized in [13; 14].

Recently, THF applications are widely used in automotive and aircraft industries. Well-known automotive applications include exhaust parts, camshafts, radiator frames, front and rear axles, engine cradles (for Ford Contour), crank shafts, frame rails (for GM Corvette), seat frames, instrumental panel beam (for Chrysler Minivan), body parts and space frame (See Figure 2.5).

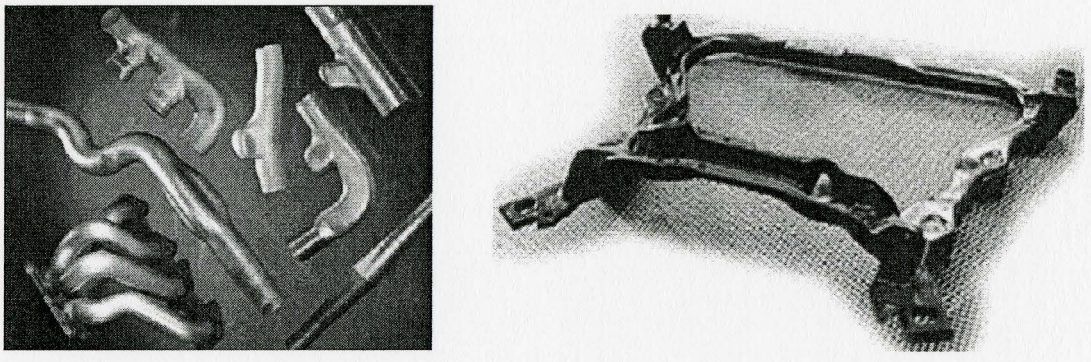

(a) Exhaust Parts (b) Engine Cradle

Figure 2.5: Parts produced by THF.

There are two variants of the THF process: high pressure forming and pressure sequence forming. In high pressure forming, the dies are closed and the tube is then calibrated by internal pressure only. In pressure sequence forming, the tube is formed while internally pressurized. As a result, a more uniform thickness variation can be obtained. Various hydroforming processes have been described by Lang et al. in [11].

2.2.4 Axial-feed Hot Gas Forming

HGTF is an innovative technique used generally in metal forming. HGTF process is very similar to THF, where instead of liquid, a gas (typically nitrogen) is used internally to pressurize the tube. HGTF is an outgrowth of super plastic forming (SPF) and hot blow forming (HBF) techniques developed by the aerospace industry to form aluminum and titanium structures. Hot metal gas forming is being developed by a consortium made up of several companies with their own areas of expertise [15; 16].

The advantages of HGTF process are that the process achieves large strain limits because it heats the initial material to 0.3-0.6 of melting temperatures, and the parts are formed at controlled pressure rates. Also, since the working material at near-melting temperatures is very soft, less internal pressure and axial force required to form the material into desired shape.

In tube forming, the term "axial feed" refer to pushing the end of the tube into the die during the forming operation [17]. Only a limited amount of material can be pushed into the die cavity during the forming process. Because of the section expansion, the component shape changes in the blank geometry and the appearing frictional resistance opposes the compressive forces along the length of the tube. There is a special point along the component where the total resistance force is equal to the compressive or buckling limit of the blank. Beyond this point, no more material can be fed without causing its wrinkling. The relationship between maximum compressive end force (F_e), the opposing frictional force (F_f), coefficient of friction between the tube and die surface μ, and the length (L) along the tube can be approximated by the following equations:

$$F_e = \pi(D - T)TU_{TS}$$

where D is tube diameter, T is material thickness and U_{TS} is ultimate tensile strength of the material.

Frictional force due to internal pressure (P_a) can be calculated as:

$$F_f = \pi D L \mu P_a$$

where L is tube length and P_a is internal feed pressure. From these equations it follows that the maximum value for tube length (L) beyond which material cannot be fed is:

$$\max L = \frac{T U_{TS}(1 - T/D)}{\mu P_a} \tag{2.1}$$

This equation shows that the maximum value of the tube length L beyond which material cannot be fed to expand the section without thinning can only be increased by either reducing the coefficient of friction μ or by keeping the feed pressure (P_a) as low as possible to avoid excessive thickening near the ends or material wrinkling.

2.3 Forming Process Parameters

Process parameters for room temperature tube hydroforming and high temperature gas forming are reviewed below. Each forming process has a set of process parameters that are mainly responsible for the quality of the final part. In these processes, a combination of internal pressure and axial feed at constant pressure and feed rate is used. The work piece is preheated and formed at the constant temperature approaching the melting point of the material.

For the THF and HGTF processes the critical forming parameters are internal pressure and axial feed, pressure rate, temperature and part geometry. Excessively high or low values can cause the material and part failure. The failure modes during tube

expansion include buckling, bursting, wrinkling or folding back. The relevant forming process parameters are discussed below.

2.3.1 Internal Pressure

In the tube forming process the major parameter that allows the tube to expand is internal pressure. The value of internal pressure in conjunction with the pressure rate are accountable for the deformation and thinning of the tube walls. Rapid application of high value of internal pressure, once medium level expansion has been attained, $d_1/d_o > 1.4$ (where d_1 is a final tube diameter and d_o is initial outer tube diameter), can cause a material failure or bursting [13].

Rimkus et al. in [18] described the application of the high internal pressure to tube manufacturing process in a technique referred to as hydrostatic-aided forming. He states that the pressure load-curve of the hydroforming process has two phases. The first phase is a process forming phase and the second phase is a process calibration phase. In the process forming phase, the expansion of the tube work-piece occurs, while in the process calibration phase, the expanded workpiece conforms to the small radii of the die cavity by constant internal pressure. The typical load-curve for the application of the internal pressure over time is shown in Figure 2.6, where forming phase occurs up to point 3 and calibration phase occurs after point 3 for about 0.03 seconds.

The pressure time history depends on several parameters. such as shell thickness, the outer diameter of the work-piece and the tensile strength of the material. The forming pressure was calculated by Rimkus et al. with the following formula:

$$p_f = \frac{2s_0 R_m}{d_0 - s_0}$$

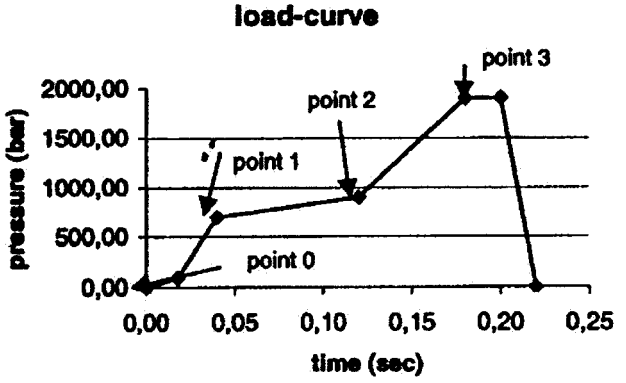

Figure 2.6: Load-curve for internal pressure vs. time [18]

where p_f is the forming pressure (N/mm^2), s_0 the tube initial wall thickness, d_0 the outer diameter of the work-piece and R_m the tensile strength (N/mm^2) of the material.

The internal pressure at point 1, according to [18] and based on practical experience, should be 10 percent smaller than p_f and the internal pressure at point 2 should be 20-40% higher than p_f.

$$p_{i1} = 0.9 p_f$$

$$p_{i2} = \left(\frac{1.2}{1.4}\right) p_f$$

2.3.2 Axial Force

With the axial force added as a process parameter, stress states in the deformation process can be better controlled. Axial feed parameter contributes to the process stability, improved part thickness uniformity and increased formability, leading to

opportunities for optimizing the deformation process.

The axial force, as introduced in [18], consists of two parts F_a0 and F_a1 (Figure 2.7). The initial axial force F_a0 is necessary in order to seal the tube with end plugs. The subsequent application of F_a1 pulls the material into the forming zone. There is no axial force applied during the calibration phase because of the high friction between the work-piece and the die caused by the high internal pressure.

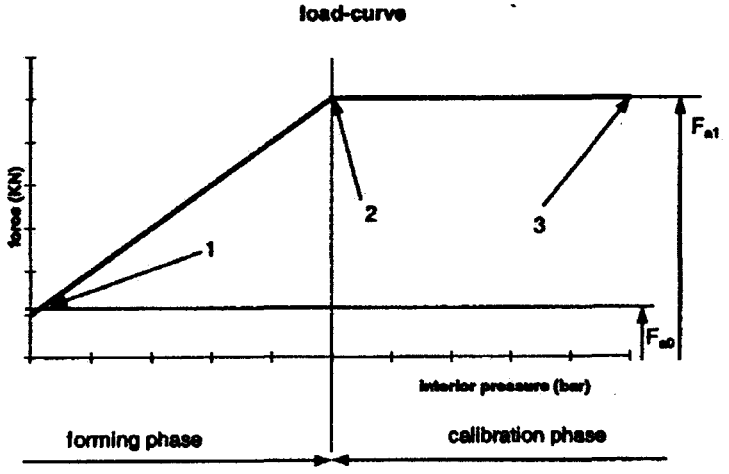

Figure 2.7: Load-curve for the axial force vs. pressure, with important points [18]

On the other hand, in case of excessively high axial force on the tube ends at the start of the process, buckling or folding back may occur. The acceptable buckling force at the start of the process is a function of the tube parameters and can be estimated theoretically [13]. For the prevention of such failure, the process should be controlled in such a way that the reduction in free tube length due to upsetting is coupled with a rapid increase in the section modulus of the tube cross-section.

Improper combination of internal pressure and axial feed may result in wrinkling. To prevent wrinkling, internal pressure in the final phase of expansion process should

be increased.

The success of tube forming process is dependent mainly on an appropriate combination of internal pressure and axial feed at the tube ends. Research shows that the axial pressure provides back support to the tube material. Excessive thinning and premature wrinkling can be prevented. Therefore, larger tube expansion can be achieved and more complex shapes can be formed.

2.3.3 Pressure Rate

Pressure rate control plays an important role in the forming process. After the dies are closed, internal fluid pressure is increased to force the material into the deformation zone. During this stage, axial feeding is also applied to the tube provide better shaping. To form small corner radii larger pressure must be applied at the end of the process. However, large inner pressure makes impossible further axial feeding because of large friction forces. As an alternative to this scenario, the die corners and small radii can be formed with less thinning if a low fluid pressure is provided during the die closure.

In tube forming, pressure rate is controlled simultaneously with axial feeding to improve formability of tubes. Pressure inside a part can be either a constant, or a function of the axial force of the feed cylinder or a function of the axial displacement of the feed cylinder or a combination of these conditions [17].

2.3.4 Temperature

Another critical factor for the polymer tube forming operations is forming temperature. Most of the metal forming operations are conducted at room temperature. In

polymer forming, since the polymeric material behavior is highly temperature dependent, the typical forming temperature is just below the melting point. Increase in forming temperature in general raises the material flow and improves the formability of the polymers.

2.3.5 Part Geometry

The part geometry is the starting point of tool design and eventually of the entire forming process, since the type and number of mechanical forces, which must be applied to a tube, are also dependent on the workpiece geometry. In this respect there is a distinction in hydroforming processes with straight initial tube and with a tube, which has undergone bending prior to forming [13]. The simplest case is when the initial tube has a straight axis. For such forming, the workpiece geometry is obtained through expansion, which can be either concentric without any counterdrafts or concentric with a number of counterdraft elements. The tube branches can be formed on to the starting tube, which are only connected to it over part of the tube shell surface. Hydroforming process is also able to form straight tubes into bent or gooseneck geometries of any type, which cover part of the workpiece length. If a tube has been pre-bent before forming (usually in one plane), then by means of internal pressure the tube is brought into full contact with the surrounding tool. To eliminate the shape errors resulting form the bending process and the wall thickness differential between the tension and compression zone of the bending arc, the pressure is introduced together with appropriate axial displacement on the ends of the tube. The aspect of workpiece geometry for tool design and for the type and number of mechanical forces that act for tube hydroforming applications is demonstrated in [13]. Two cases of the process in terms of part geometry are illustrated in [13]: the hydroforming process for tubes with a straight line and tubes with a bent center line.

2.3.6 Miscellaneous parameters

Some miscellaneous parameters of the process for polymers, such as heating rate, hold time to temperature, cooling rate, cooling time to temperature, cooling medium should be also considered. They are not as critical to the process compared to the parameters explained in the sections above. However, their optimized values can contribute to better quality of the final part.

2.4 FE Simulations of Polymer Forming Process

Many numerical simulations using the FE method have been employed to simulate polymer forming process in the past. Experimental and numerical investigations of vacuum forming process are described in [19]. Description of the process and FE simulation of blow molding process is introduced in [20]. Modeling of tube hydroforming or tube hot gas forming processes for metals is relatively well established in literature. Different models have been created, such as axisymmetric or 3D FE models [21; 22; 23]. The main interests in simulation of tube forming processes is prediction of the typical failure modes, such as wrinkling, bursting, buckling, folding back and tube wall thickness distribution. A lot of work has been done in optimization of the forming process via experimental trial and error or other optimization techniques such as sequential quadratic programming. However, the FE models of forming process for metals have been based on the metal plasticity theory and can not be applied to polymeric rubber-like viscoelastic nearly incompressible materials.

An increasingly rapid growth in applications of polymeric materials has created a need for developing FE models which can better describe the material response under different loading conditions. A number of FE models have been developed that

could predict the behavior of polymeric materials under stress with certain accuracy. Two of the most common hyperelastic models are by Mooney [24] and Ogden [25]. These models describe the behavior of incompressible solids or rubber-like elastomeric materials and are briefly discussed in section 2.4.5. The models are unable to simulate the shape change in the part resulting from part cooling and part removal from the die (i.e, part unloading).

Later research incorporated the viscous factor into the material models. A number of general viscoelastic-viscoplastic material models have been developed for the polymeric materials [26; 27]. In particular, a Hybrid Model (HM) has been developed by the orthopedic industry researchers for Ultra High Molecular Weight Polyethylene (UHMWPE) used in total joint replacements. Model is able to predict accurately the deformation of UHMWPE under multiaxial loading conditions. More recently, an Augmented HM (AHM) has been proposed [28]. Also, the model is able to predict the unloading behavior of the polymer. In this work, hyperelastic Ogden material model and AHM are applied to the forming of a commercial polypropylene tube.

2.4.1 FE Model Type

For numerical representation of the process different types of models can be used, such as three-dimensional (3D) or axisymmetrical. 3D model is required for representation of the more complex process and material properties. For example, 3D model should be utilized in case of non-axisymmetric part and/or material anisotropy. However, the input file to define the model geometry becomes rather large and computational time required is greatly increased. Thus, for a simpler axisymmetric part and for nearly isotropic tube cases, to make the modeling process more efficient in terms of computational time, a simpler axisymmetric FE model can be used. In some cases, such as straight axis tube hydroforming with the material anisotropy, a 2D axisym-

metric model can still be utilized.

In the work of Cherouat et al. [22], thin tube hydroforming process for producing spherical and complex shaped parts was introduced. The effect of ductility with respect to the fracture for the thin wall tube structures was investigated. The forming process was simulated with a 3D ductile damage FE model.

A rotational symmetric tube bulging with inside pressure and axial compression, was introduced in [21]. The process was investigated with regards to the common instabilities, such as buckling, wrinkling and tube wall thinning. Due to the symmetry the tube was modeled with 2D axisymmetric model (Figure 2.8). A comparison between the simulated and the real process showed that despite the initial symmetry of the process, the assumption of the longitudinal symmetry in the conditions of compression instability is not always justified.

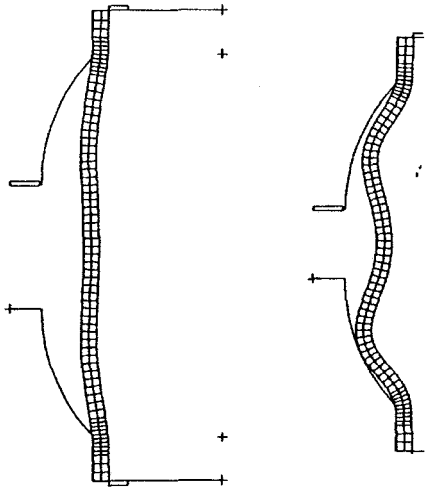

Figure 2.8: Deformed tube at the end of the first and second stage of forming [21]

2.4.2 Element Types and Meshing techniques

Discretization of the part geometry into small "finite" elements is a fundamental component of the FE model. Different types of elements can be used to represent the part with the different FE models. Each element is characterized by the following: family, degrees of freedom, number of nodes, formulation and integration [29].

There are different meshing techniques and element types that can be used in FE modeling. The size and uniformity of the mesh depends on the workpiece and rigid body geometries and the process parameters. The mesh should be adequate to capture all of the features of the objects accurately. When using a uniform mesh, the element size must be small enough to capture the smallest feature of the object.

For the modeling of the tube in [21], axisymmetrical elements of the second order with a reduced integration CAX8R in FE code Abaqus were used [29]. Axisymmetric elements, a "CAX" class of elements in Abaqus, are suitable for analysing structures with axisymmetric geometry subjected to axisymmetric loading.

In work of Cherouat [22], to investigate the hydroforming process, a three dimensional FEA was also performed in Abaqus/Explicit. The FE model utilized trilinear hexahedral eight-nodes elements with reduced integration points (C3D8R) in the analysis.

2.4.3 Contact and Friction Considerations

The contact area that develops between the inner surface of the die and outer surface of the tube walls during the tube forming process increases largely under the action of friction [13]. Wall thickness reduction may appear and the small radii of the formed

element could be shaped with correspondingly high internal pressures. The main parameters affecting the friction in tube hydroforming process are the lubricant, the tube material (metal, aluminium or plastic) and die surface (surface finish, hardness and surface treatment, coating). Friction calculations and various types of lubricants were described in [14].

Effect of friction coefficient on maximum expansion radius-axial displacement relation for aluminum alloy tube (A6063) has been investigated in [30]. Two friction coefficients (μ_k=0.10 and μ_k=0.06 with lubricating oil R303P and PG3740 respectively) have been considered. The results showed that the curve of maximum expansion radius to the required axial displacement shifts upward as friction coefficient μ increases (Figure 2.9). In other words, the results showed that the higher friction conditions result in a deformation process where local thinning occurs earlier.

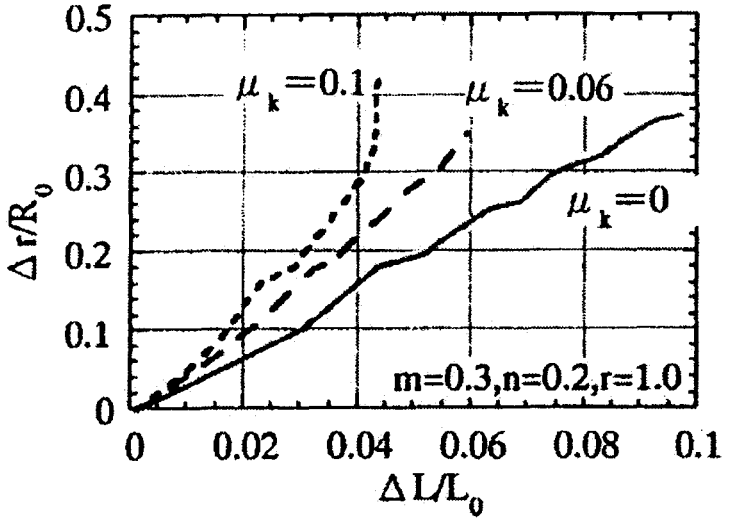

Figure 2.9: Influence of friction coefficient μ on maximum expansion radius-axial displacement relation [30]

The work reported in [22] describes the friction effect with respect to the thickness

distribution in FE simulation of thin aluminium alloy tube hydroforming. The FE model accounts for isotropic hardening and isotropic ductile damage of thin tubes. The effect of friction coefficient on the tube wall thickness distribution is shown for a complex shape part (Figure 2.10). Three values of friction coefficient μ have been compared. The maximum value μ=0.4 represented a "stick" metal-metal contact. $\mu = 0.2$ corresponded to a moderate friction coefficient and $\mu = 0.0$ represented a perfectly sliding contact between the tube and the die. In the first case ($\mu = 0.4$), the thickness expansion was the largest whereas in the case of sliding contact the thickness expansion was insignificantly small. As the results show, friction coefficient exerts a significant influence on part thickness uniformity.

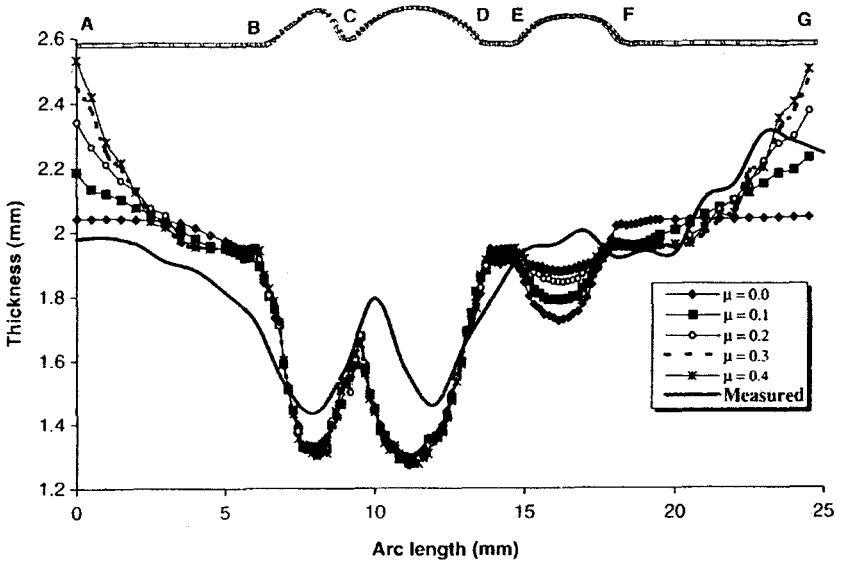

Figure 2.10: Thickness distribution along the axial feed for different friction coefficients [22]

A technique for the determination of the coefficient of friction in hydroforming of tubes was presented in [31]. The measuring principle is based on upsetting of a tube. The diagrams for the identification of the coefficient of friction were constructed via implementation of a FE simulation process model data.

2.4.4 Boundary Conditions

During the process, the workpiece is exposed to the different forces, loads and pressure. In tube forming as well as in thermoforming or blow molding, inner die walls define the boundaries of the formed part. Upper and lower dies represent the undeformable rigid master surface. Workpiece is subject to deformation and therefore represent the deformable slave surface. In tube forming, part side walls are also restricted from expansion by plugs which defines the final length of the tube part. Example of defining the boundary conditions in tube hydroforming is described in [32]. Experiments were conducted on the tube hydroforming machine located to form X- and T-branch components from straight copper tubes with different boundary conditions such as forming pressure and end feed (Figure 2.11).

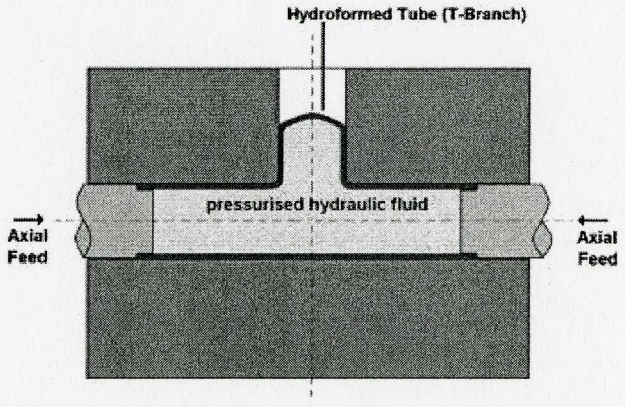

Figure 2.11: T-branch hydroforming setup (deformed) [32]

Different forming steps require the proper adjustment of boundary conditions. Two main steps in tube forming is part forming, part calibration and part removal process steps. In part forming, tube is expanded by internal pressure and tube ends simultaneously are fed into the die cavity. Boundary conditions in this step are defined by upper die, lower die and position of the side plugs. In part removal step, the side plugs are removed and part is free to adjust for material springback.

2.4.5 Constitutive Laws (Material Models)

There are different types of constitutive models for polymer processing modeling. The most utilized material models are hyperelastic material models. They have been successfully used for several decades. However, due to some limitations of hyperelastic models, more advanced viscoelastic-viscoplastic material models have been developed. Their use in simulating polymer forming processes has been limited due to luck of availability of these models in most commercially available FE programs and difficulty in obtaining the needed material parameters.

Hyperelastic Material Models

Hyperelastic material models are widely used in industry for simulation of the mechanical response of the elastomers and polymeric materials. The main polymer forming applications utilizing the hyperelastic material models are thermoforming and blow molding simulations. Technology of thermoforming and experimental stress-strain data for several types of polymers were presented by James L. Throne in [33]. Material coefficients were calculated based on the tensile, compression and creep test results. For prediction of the material response, different hyperelastic material models were utilized. The finite element simulation of response of hyperelastic materials and elastomeric solids is presented by several researchers [34; 35; 36; 37; 38; 39].

Hyperelastic materials are described in terms of a strain energy potential. The strain energy potential , U, defines the strain energy stored in the material per unit of reference volume (volume in the initial configuration) as a function of the strain at that point in the material. There are several forms of strain energy potentials that are used to describe the hyperelastic material behavior. The most widely used in industry and utilized by commercial software package Abaqus [29] are 8 chain hyperelastic mate-

rial model (so-called Arruda-Boyce), Mooney-Rivlin and Ogden hyperelastic material models.

The 8 chain hyperelastic material model is more suitable for the applications involving rubber-like incompressible solids [40]. The strain energy potential for the 8 chain hyperelastic model is expressed as:

$$\begin{aligned} U &= \mu\left\{\frac{1}{2}\left(\overline{I}_1-3\right)+\frac{1}{20\lambda_m^2}\left(\overline{I}_1^2-9\right)+\frac{11}{1050\lambda_m^4}\left(\overline{I}_1^3-27\right)\right. \\ &+ \left.\frac{19}{7000\lambda_m^6}\left(\overline{I}_1^4-81\right)+\frac{519}{673750\lambda_m^8}\left(\overline{I}_1^5-243\right)\right\}+\frac{1}{D_c}\left(\frac{J_{el}^2-1}{2}-\ln J^{el}\right) \end{aligned} \tag{2.2}$$

$$\overline{I}_1=\overline{\lambda}_1^2+\overline{\lambda}_2^2+\overline{\lambda}_3^2$$

$$K_0=\frac{2}{D_c}$$

where U is the strain energy per unit of reference volume, $\overline{I}_1$ is the first deviatoric strain invariant, $\mu = nk\theta$, n is the chain density, k is Boltzmann's constant, θ is absolute temperature, λ_m^2 is the number of rigid links composing a single chain, D_c is the coefficient of compressibility, λ_1, λ_2, λ_3 are the deviatoric stretches, J^{el} is the elastic volume ratio and K_0 is the initial bulk modulus.

The form of the strain energy function for Mooney-Rivlin model is:

$$U=C_{10}\left(\overline{I}_1-3\right)+C_{01}\left(\overline{I}_2-3\right)+\frac{1}{D_c}\left(J^{el}-1\right)^2 \tag{2.3}$$

$$\overline{I}_1=\overline{\lambda}_1^2+\overline{\lambda}_2^2+\overline{\lambda}_3^2; \qquad \overline{I}_2=\overline{\lambda}_1^{(-2)}+\overline{\lambda}_2^{(-2)}+\overline{\lambda}_3^{(-2)}$$

$$\mu_0=2(C_{10}+C_{01}); \qquad K_0=\frac{2}{D_c}$$

where C_{10} and C_{01} are temperature-dependent material parameters which are obtained by curve-fitting to the experimental data by means of multifunctional curve-fitting routine, D_c is a temperature-dependent coefficient of compressibility and μ_0 is

the initial shear modulus . The stress-stretch ratio function in Mooney-Rivlin model is determined by the derivatives of strain energy potential with respect to the strain invariants $\overline{I}_1$ and $\overline{I}_2$.

For a better predictions of material response, Ogden [25] proposed replacing the general Mooney-Rivlin strain energy function model. The form of the Ogden strain energy potential is:

$$U = \sum_{i=1}^{N} \frac{2\mu_i}{\alpha_i^2} \left(\bar{\lambda}_1^{\alpha_i} + \bar{\lambda}_2^{\alpha_i} + \bar{\lambda}_3^{\alpha_i} - 3 \right) + \sum_{i=1}^{N} \frac{1}{D_i} \left(J^{el} - 1 \right)^{2i} \tag{2.4}$$

where $\bar{\lambda}_i = J^{-\frac{1}{3}} \lambda_i$, $\bar{\lambda}_i$ are the deviatoric principal stretches, λ_i are the principal stretches; N is a material parameter; and μ_i, α_i, and D_i are temperature dependent material parameters.

The initial shear modulus and bulk modulus for the Ogden form are given by

$$\mu_0 = \sum_{i=1}^{N} \mu_i, \qquad K_0 = \frac{2}{D_c} \tag{2.5}$$

Viscoelastic-Viscoplastic Material Models

The first numerical models for analyzing deformation of polymer utilized the classical J-2 plasticity theory. J-2 plasticity theory is a deviatoric rate independent plasticity approach with a Mises yield surface and a flow rule with isotropic hardening [41; 42; 43].

However, the classic isotropic plasticity and elasto-perfectly plastic models were developed for metals and had several critical limitations utilized with polymers, such as rate and hydrostatic stress independency and linearly elastic recovery rule [44]. As a result, those models significantly over predict plastic strain upon unloading.

Furthermore, recent studies show that the J-2 plasticity model cannot predict the molecular anisotropy that evolves in polymers at large deformations (Figure 2.12 [26]). Consequently, in the last decade, several advanced constitutive theories have been developed.

The mechanical behavior of many semi-crystalline polymeric materials is time and temperature dependent. The stress-strain behavior in elastic and plastic regions are nonlinear due to the distribution in plastic shear strength with deformation. To predict the polymer behavior at large strain time-dependent deformations under the multiaxial stress conditions, a number of different constitutive material models have been developed.

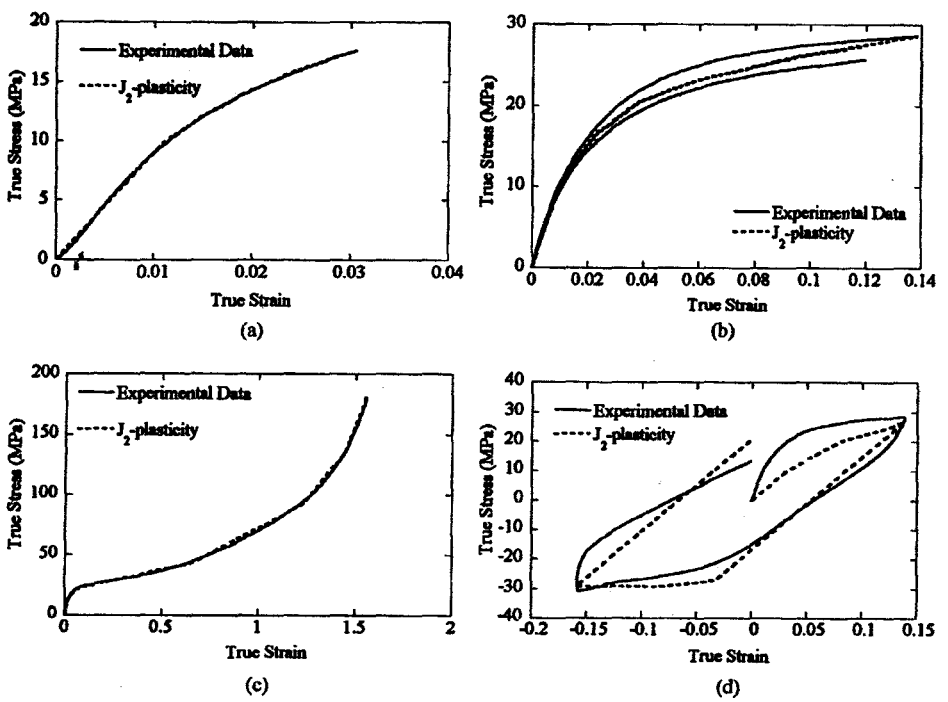

Figure 2.12: Comparison between the J2-plasticity model and experimental data [26]

These models are based on the physical behavior of the polymer microstructure and

incorporate continuous description of material response from elastic to viscoelastic/ viscoplastic state [26].

The Arruda-Boyce (AB) model was developed for the materials with initial linear elastic response followed by yielding and then strain hardening at large deformations. [45; 46; 47; 48]. It was able to predict the time and temperature dependent behavior of the glassy polymers at large strain deformations.

The total deformation gradient consists of elastic and plastic components, $F=F^eF^p$. A one-dimensional rheological representation of the AB model is given in Figure 2.13. This decomposition is illustrated by a spring element (E2) and a spring and dashpot element (E1, V1) in series. The spring E2 and the spring and dashpot element E1 represent elastic and plastic response of the material respectively.

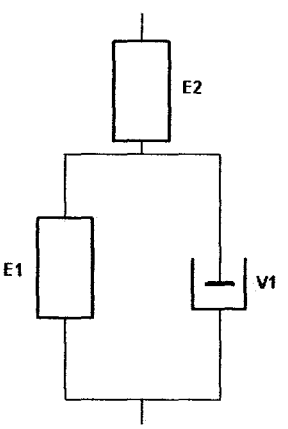

Figure 2.13: One-dimensional rheological representation of Arruda-Boyce model [26]

The Cauchy stress then can be calculated from the linear elastic response:

$$\mathbf{T} = \frac{1}{J^e}\left(2\mu^e\mathbf{E}^e + \lambda^e tr[\mathbf{E}^e]\mathbf{1}\right)$$

where $E^e=ln[V^e]$ is the logarithmic true strain, $J^e=det[F^e]$ is the elastic volumetric change, and μ^e, λ^e are Lame's constants. The stress driving the plastic flow is given

by the tensorial difference between the total stress and the convected backstress

$$\mathbf{T}^* = \mathbf{T} - \frac{1}{J^e}\mathbf{F}^e\mathbf{T}^p\mathbf{F}^{eT}$$

The deviatoric backstress $\mathbf{T}^p$ in the formula above is given by the incompressible eight-chain model

$$\mathbf{T}^P = \frac{\mu^p}{\overline{\lambda^p}}\frac{L^{-1}\left(\overline{\lambda^p}/\lambda^p_{lock}\right)}{L^{-1}\left(1/\lambda^p_{lock}\right)} dev\left[\mathbf{B}^p\right]$$

where μ^p, λ^p_{lock} are material constants, B^p=F^pF^{pT}, $\overline{\lambda^p}$=$\sqrt{tr(\mathbf{B}^p)/3}$ is the effective chain stretch based on the eight chain-topology assumption, and $L(x)$= $coth(x)$ -1/x is the Langevin function. The plastic flow rate is given by

$$\dot{\gamma}^p = \dot{\gamma}_0 exp\left[\frac{-As}{k_B\theta}\left(1 - \left(\frac{\tau}{s}\right)^{5/6}\right)\right]$$

where $\dot{\gamma}_0$, A, s are material constants, k_B is Boltzmann's constant, and θ is the absolute temperature. Difference between a stress component of 5/6 and 1 is very small. Thus, the expression for the plastic flow rate can be simplified to

$$\dot{\gamma}^p = \dot{\gamma}_0 exp\left[\frac{\tau - s}{\tau_{base}}\right] = \dot{\gamma}_i exp\left[\frac{\tau}{\tau_{base}}\right]$$

where τ_{base}=$k_B\theta/A$, and $\dot{\gamma}_i$= $\dot{\gamma}_0 exp(-s/\tau_{base})$. The scalar equivalent stress τ is taken as the Frobenius norm of the deviatoric part of the driving stress τ=$\| dev[\mathbf{T}^*] \|_F$.

The rate of plastic deformation is given by

$$\mathbf{D}^p = \frac{\dot{\gamma}^p}{\tau} dev[\mathbf{T}^*]$$

AB model predicts well both small strain and large strain monotonic loading, as well as monotonic intermediate strains at different strain rates (Figure 2.14). However, the nonlinear behavior of material prior to yield is not captured.

The Hasan-Boyce (HB) material model [49] is an extension of the AB model. HB is

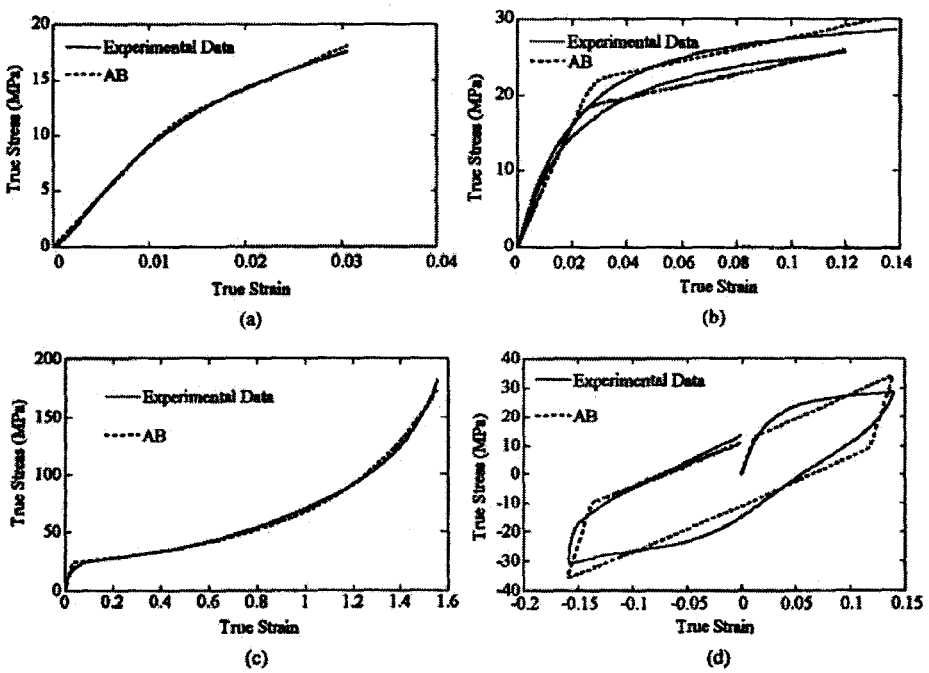

Figure 2.14: Comparison between the Arruda-Boyce (AB) model and experimental data [26]

based on the same kinematic framework with the addition of distribution and evolution of activation energies into the formula for magnitude of the plastic deformation rate ($\dot{\gamma}^p$). By including forward and backward flow in addition to the storage of inelastic energy, the following expression for the plastic deformation rate was obtained

$$\dot{\gamma}^p = \dot{\gamma}_0 \int_{-\infty}^{+\infty} \phi(x) \left\{ exp\left[\frac{-(x-\tau)}{\tau_{base}}\right] - exp\left[\frac{-(x+\tau)+U}{\tau_{base}}\right] \right\} dx$$

By integrating this equation, the following expression for plastic flow rate was obtained

$$\dot{\gamma}^p \approx \dot{\gamma}_i \frac{1 - e^{(-2\tau+U)/\tau_{base}}}{1 + 1.2(w/\tau_{base})^2} exp\left[\frac{\tau + w}{\tau_{base}}\right]$$

where U is an internal energy driving recovery during unloading and w is a midpoint of the activation energy distribution. Comparison between the Hasan-Boyce (HB)

model and experimental data is presented in Figure 2.15. HB model gives good predictions under monotonic loading independent of strain rates and final strain level.

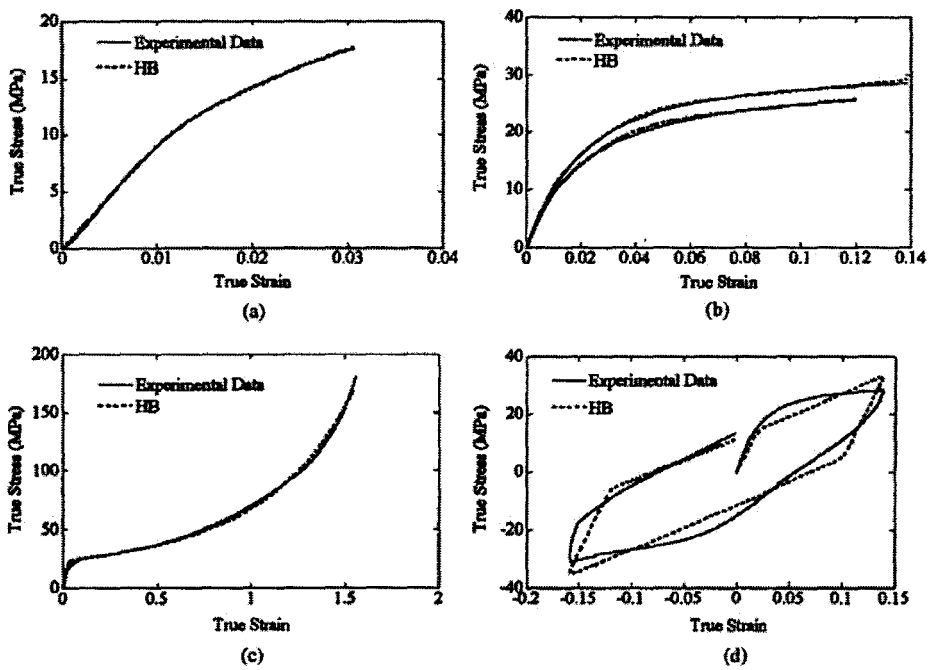

Figure 2.15: Comparison between the Hasan-Boyce (HB) model and experimental data [26]

Another recently developed is the Bergstrom-Boyce (BB) material model [50]. BB model is a new micromechanism inspired constitutive model, that allows for prediction of large strain time-dependent behavior of elastomeric material.

In a rheological representation of the BB model, the behavior of elastomeric materials can be decomposed into two networks acting in parallel: one network represents the equilibrium state of the material (E2), while the other network captures the time-dependent response of the material (E1, V1) (Figure 2.16). The first network can be modeled by any of the classical models based on hyperelasticity. The second network

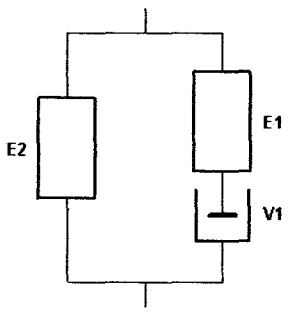

Figure 2.16: One-dimensional rheological representation of Bergstrom-Boyce model [26]

is modeled with a time-dependent element which acts to relieve the strain on the network with time and capture the material behavior observed during the experiments.

The effective strain rate is introduced by the equation

$$\dot{\gamma}_B = [\overline{\lambda_B^p} - 1]^C \left[\frac{\tau}{\tau_{base}}\right]^m \tag{2.6}$$

where $\overline{\lambda_B^p}=\sqrt{tr[\mathbf{B}_B^p]/3}$, and C, m, and τ_{base} are material parameters. The theoretical data from the model was then compared with the experimental data for UHMWPE and Chloroprene and Nitrile rubber. The results showed a good quantitative agreement for different strain rates and relaxational behavior (Figure 2.17 and 2.18).

The Hybrid Model (HM) is a further enhancement to the BB model and is able to account for the multiaxial mechanical response of conventional and highly crosslinked UHMWPE [26; 27]. The HM incorporates many features of the previously described theories. To improve the predictive capabilities of the model, the deformation state was decomposed into elastic, backstress and viscoplastic components.

$$T = \frac{1}{J^e}\left(2\mu_e E^e + \lambda_e \mathrm{tr}\left[E^e\right]\mathbf{1}\right)$$

where $E^e=ln[V^e]$ is the logarithmic true strain, $J^e=det[F^e]$, and μ_e, λ_e are Lame's constants. The backstress tensor is responsible for the large strain behavior and

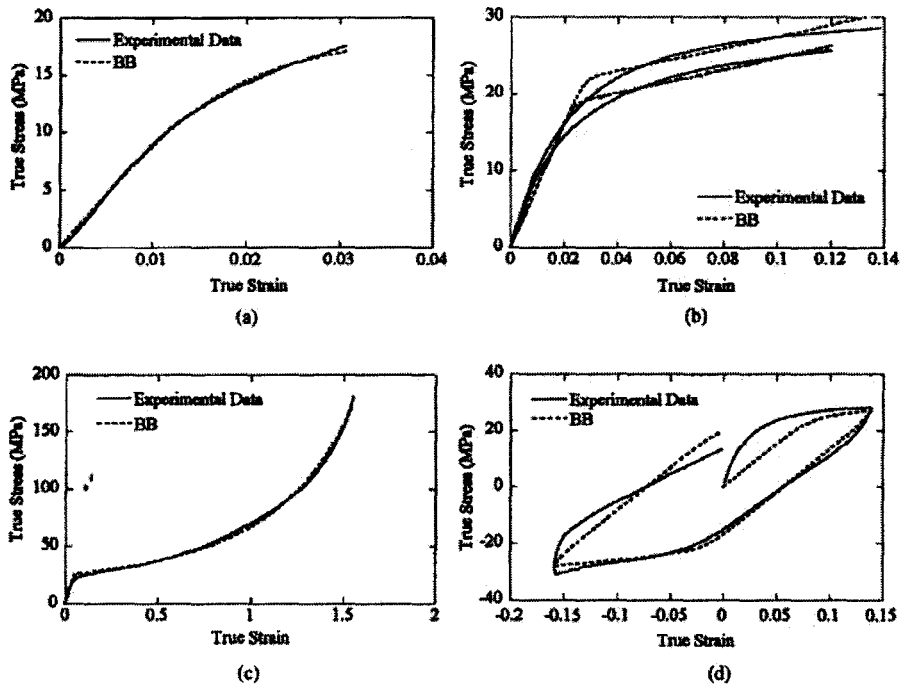

Figure 2.17: Comparison between the Bergstrom-Boyce (BB) model and experimental data for UHMWPE [26]

non-linear recovery during unloading. The total stress is representing the backstress tensor and consists of three terms: the first term ($\mathbf{T}_{8chain}$) is represented by the eight chain model, the second term ($\mathbf{T}_{12}$) is represented by a strain energy function and the third term ($\mathbf{T}_N$) is given from the nonlinear elastic process associated with the deformation of the crystalline phase.

$$\mathbf{T}^p = \frac{1}{1+s}\left[\mathbf{T}_{8chain} + s\mathbf{T}_{I2}\right] + \mathbf{T}_N \tag{2.7}$$

$$\mathbf{T}_{8chain} = \frac{\mu^p}{\bar{\lambda}^p}\frac{L^{-1}\left(\bar{\lambda}^p/\lambda^p_{\text{lock}}\right)}{L^{-1}\left(1/\lambda^p_{\text{lock}}\right)}\text{dev}[\mathbf{B}^p] \tag{2.8}$$

$$\mathbf{T}_{I2} = \mu^p\left[I_2^*\mathbf{B}^* - \frac{2I_2^*}{3}\mathbf{1} - (\mathbf{B}^*)^2\right] \quad I_2^* J^{2/3}\left[\lambda_1^{-1} + \lambda_2^{-1} + \lambda_3^{-1}\right] \tag{2.9}$$

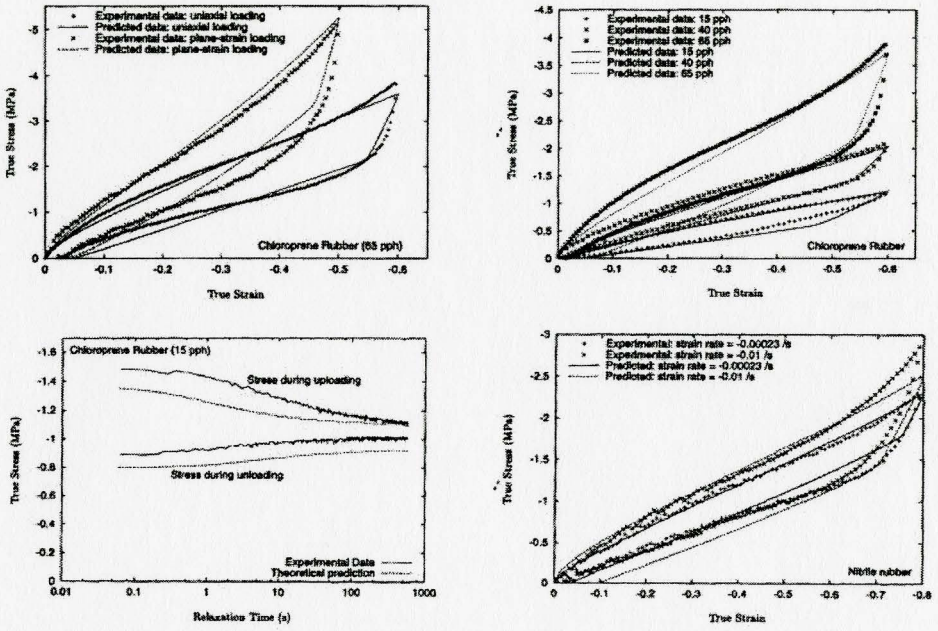

Figure 2.18: Comparison between the Bergstrom-Boyce (BB) model and experimental data for Chloroprene and Nitrile rubber [50]

$$\mathbf{T}_N = \frac{\hat{\varepsilon} E_i \left(1 - e^{-\varepsilon/\hat{\varepsilon}}\right)}{e^{2\varepsilon} - e^{-\varepsilon}} \mathrm{dev}[\mathbf{B}^p] \tag{2.10}$$

$$\mathbf{T}^* = \mathbf{T} - \frac{1}{J^e} \mathbf{F}^e \mathbf{T}^p \mathbf{F}^{eT} \tag{2.11}$$

$$\dot{\gamma}^p = \left(\frac{\tau}{\tau_{base}}\right)^{m(\varepsilon)} \tag{2.12}$$

Results from HM model are shown in Figure 2.19.

The constitutive models proposed by Boyce and co-workers have largely dealt with the loading behavior of the polymers. There has been no attention paid to the unloading behavior of such materials. The work of Bergstrom et al. [28], the so-called

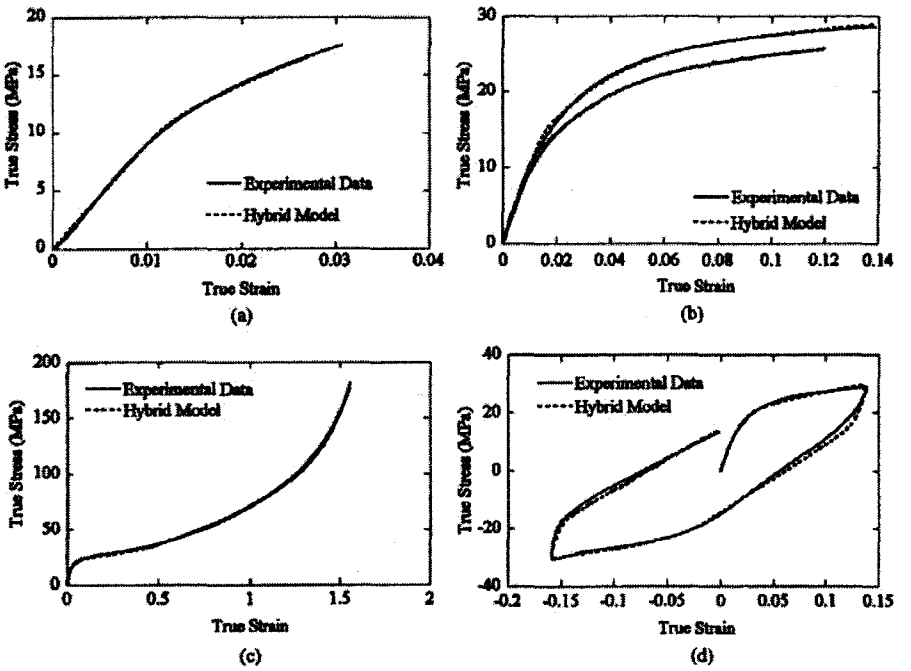

Figure 2.19: Comparison between the Hybrid model and experimental data [26]

"Augmented" Hybrid model deals with the unloading and cyclic loading of semicrystalline polymers. This model was utilized in the present work. It is perhaps the most advanced model for large deformations of semicrystalline polymers and includes nonlinear unloading. One-dimensional rheological representation of AHM is presented in Figure 2.20. The viscoplastic component in AHM incorporates time-dependent viscoplasticity to the backstress network.

The Cauchy stress is represented by the isotropic linear elastic relationship:

$$T = \frac{1}{J^e}\left(2\mu_e E^e + \lambda_e \mathrm{tr}\left[E^e\right]\mathbf{1}\right)$$

where μ_e and λ_e are Lame's constants that can be derived from the Young's modulus and Poisson's ratio:

$$\mu_e = E_e/(2(1+\nu_e))$$

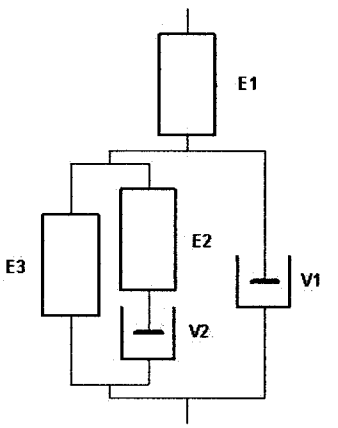

Figure 2.20: One-dimensional rheological representation of Augmented HM

$$\lambda_e = E_e \nu_e / ((1 + \nu_e)(1 - 2\nu_e))$$

$J^e = det[F^e]$ is the relative volume change of the elastic deformation, F^e is the deformation gradient, $E^e = ln[V^e]$ is the logarithmic true strain, and V^e is the left stretch tensor from the polar decomposition of F^e.

As it was mentioned earlier in Hybrid model formulation, the equilibrium part of the backstress network is described by the formulas:

$$T_A = \frac{1}{1 + q_A} \left[T_{8chain} \left(F^p; \mu_A, \lambda_A^{lock}, \kappa_A \right) + q_A T_{I_2} \left(F^p; \mu_A \right) \right]$$

where T_A is a tensor valued function of the viscoplastic deformation gradient F_p, λ_A^{lock} is the locking stretch, k_A is the bulk modulus, μ_A is the shear modulus and q_A is a material parameter. The viscoplastic flow of the backstress network is derived from the hyperelastic representation:

$$T_B = s_B \cdot T_A \left(F_B^e \right)$$

where s_B is a material parameter describing the stiffness of the backstress network.

$$\dot{s}_B = -p_B \cdot (s_B - s_{Bf}) \cdot \dot{\gamma}_C$$

where p_B is a material parameter specifying the transition rate of the distributed yielding event, s_{Bf} is the final value of s_B reached at fully developed plastic flow, and $\dot{\gamma}_C$ is the magnitude of the viscoplastic flow rate.

$$\dot{\gamma}_B^{\mathrm{v}} = \dot{\gamma}_0 \left(\frac{\tau_B}{\tau_B^{base}} \right)^{m_B}$$

The velocity gradient of the viscoelastic flow of the backstress network can be found as follows:

$$L_B^{\mathrm{v}} = \dot{\gamma}_B^{\mathrm{v}} F_B^{e-1} \frac{\mathrm{dev}\,[T_B]}{\tau_B} F_B^e$$

where $\dot{\gamma}_B^{\mathrm{v}}$ is the rate of viscoplastic flow of the time dependent network B, $\tau_B = ||\mathrm{dev}[T_B]||_F$, τ_B^{base} and m_B are material parameters.

$$L^p = \dot{\gamma}_C \left[R^{eT} \frac{\mathrm{dev}\,[T_C]}{\tau_C} R^e \right]$$

where $L^p = \dot{F}^p F^{p-1}$, $T_C = T - \left[F^e (T_A + T_B) F^{eT} \right] / J^e$ is the stress acting on the relaxed configuration convected to the current configuration. The magnitude of the viscoplastic flow $\dot{\gamma}_C$ is:

$$\dot{\gamma}_C = \dot{\gamma}_0 \left(\tau_C / \tau_C^{base} \right)^{m_C}$$

where τ_C^{base} and m_C are material parameters.

2.5 Process Optimization Studies

The ultimate goal for the tube forming applications is to prevent failure of the tube throughout the process, to ensure that the tube wall along the length of the tube is in contact with the die at the end of the process and to achieve the wall thickness distribution as uniform as possible. Different methods for control and optimization of the tube forming process can be utilized. Control and optimization of the process

is often performed by experimental trial and error approach. More precise determination of process conditions is possible the aid of more elaborate methods, such as the finite element method (FEM).

Optimization work on blow molding process was carried out by Tahboub and Rawabdeh in [9]. In particular, design of experiments was implemented to the extrusion blow molding process. The objective was to determine process parameters setting that yield the required volume and mass of the production bottles. The desired volume of produced bottles was determined from the specifications and fell within 407 - 415 ml (a target value of 411 ml). Analysis and optimization work utilized statistical data analysis of variance and regression analysis. Selected levels for the factors are shown in Figure 2.21 [9]. After the statistical data model was built, the result was validated with confirmation experiments. This data is presented in Figure 2.22 [9].

	Variable name		Low value (−)	High value (+)
X_1	A: Screw speed (rpm)	Controllable	425	455
X_2	B: Melting temp (°C)	Controllable	165	175
X_3	C: Cooling time (sec)	Controllable	20	23
X_4	D: Pressure (bar)	Controllable	4.5	6
X_5	E: Mold temp. (°C)	Uncontrollable	17	20
X_6	F: Ambient temp. (°C)	Uncontrollable	7	40

Figure 2.21: Selected levels for the factors [9]

Sample	Volume (ml)	Mass (gm)
1	408	38.8
2	409	38.7
3	408	38.8
4	408	38.9
5	409	38.8
6	409	38.7
7	409	38.7
8	409	38.8
9	408	38.9
10	409	38.9

Figure 2.22: Confirmation data [9]

Although the results of the volume were slightly less than the mean target, the statistical approach led to a very small variation in the volume and improved consistency of the data.

Hydroforming process requires precise and safe control of the process parameters to provide desirable properties to the formed item. For example, in tube hydroforming, intermal pressure and axial feed affect the resulting tube shape and wall thickness and the success of the forming process depends on the proper combination of both. The variety of possible combinations gives an opportunity to pose optimization problems. In such an optimization problem, optimal profiles for the manipulated process parameters are sought such that the value of a specified objective is either minimal or maximal. The specified objective must be a mathematically expressed function which depends on the process parameters explicitly or implicitly. Such an optimization problem can be solved using numerical simulations with a finite element model and an optimization solver. The other advantage of considering the hydroforming process as an optimization problem with a finite element model is the ability to implement sensitivity analysis. Sensitivity analysis provides important information on the correlations between changes in the solution and changes in the process parameters showing which process parameters most significantly affect the solution and which do not have large impact on it.

Sensitivity analysis and optimization of the tube hydroforming process were reported by Yang et al. [51]. Here, the authors posed an optimization problem of finding the optimum loading paths for internal pressure and axial feed which minimize the tube thickness variation which can be described as follows:

$$\min_{p} f(p) = \left(\sum_{i=1}^{N} \left| \frac{h_i - h_0}{h_0} \right|^2 \right)^{1/2}$$

subject to the constraint function:

$$g_i(p) = \left(\sum_{i=1}^{M} |d_i|^2 \right)^{1/2}$$

where p is a design parameter, h_0 is the initial thickness, h_i is the final thickness of element i, which is an implicit function of p and N is a number of elements. The parameter M is the total number of nodes and d_i is the distance of node i from the tool, which is also an implicit function of p. To describe the internal pressure and the axial displacement, B-splines were proposed and the cubic B-spline functions were used in the simulations presented in the paper.

The choice of the optimization solver depends on the posed problem constraints. For the unconstrained problem, the authors suggest quasi-Newton algorithm, while for the problems with equality and inequality constraints, the algorithms with Lagrangian multipliers or Sequential Quadratic Programming techniques should be used. The latter was employed in the paper.

The sensitivity analysis was accomplished by direct differentiation of the objective function with respect to the design parameters which appeared to be consistent with the finite difference approximation. The authors showed that the application of the optimal load paths for internal pressure and axial feed obtained from the numerical simulations resulted in improvement of the tube thickness distribution. Optimization algorithm of loading path was also introduced by Xing et al. [23]. Multivariate statistical data analysis of HGTF and optimization optimization of axial-feed HGTF process parameters was introduced by this author [52].

In this chapter, literature review relevant to the current research work was introduced. Common polymer processing techniques were discussed. Work of different researchers on polymer process simulations with similar process parameters was presented. A

brief description of constitutive material models for polymer process simulation including hyperelastic and advanced viscoelastic-viscoplastic models was presented.

In the following chapter, details of the experimental procedure for axial-feed hot gas tube forming of PP are presented.

Chapter 3

Experimental Procedure

Experimental part of present research consisted of controlled axial feed HGTF tests and uniaxial tensile tests. Tensile testing and HGTF experiments were carried out on extruded PP tube using two recently commissioned test systems in the Materials Forming Laboratory (MFL). Experimental procedures for the above tests are presented in this chapter.

3.1 Tube Material Description and Samples Preparation

The tube material investigated in this research was a INEOS polyolefin (formerly innovene) - polypropylene (PP) random copolymer of grade R01C-00. This PP tube was a low flow rate, high clarity random copolymer designed for extrusion, thermoforming and blowmolding. Applications that require good see-through clarity combined with good heat resistance and refrigerator temperature impact properties can benefit from the use of R01C-00. The tensile strength at yield of PP random copolymer (injection

molded) provided by the supplier was 4640 psi. The tensile strength was measured according to ASTM D638 standard by the supplier.

Two different sets of specimens, tensile and tubular, were cut from the initial extruded tube material. A photograph of a tensile test specimen before deformation is shown in Figure 3.1. The test specimens were cut according to type 5 of ASTM D638 Standard. The size of the specimen was chosen based on the material properties and dimensions of the high temperature environmental chamber utilized in the high temperature tests. To measure the specimen elongation, the gage length of the specimen was marked with two contrasting marks. The specimens preparation and dimensions are described in Appendix A.

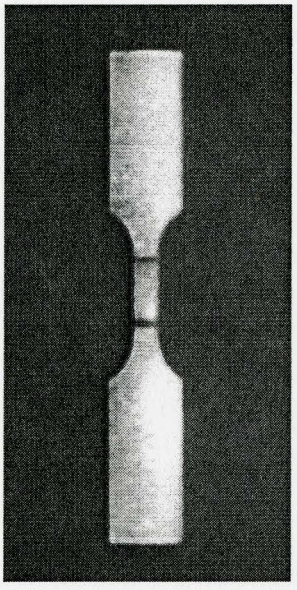

Figure 3.1: Tensile specimen with two contrasting marks

For axial-feed HGTF experiments, tubular specimens were cut into pieces of 215.9 mm length each. The outer diameter of each tube specimen as well as initial tube material was 50.8 mm and the inner diameter was 44.45 mm (Figure 3.2). The ends of the each tube piece were machined to smooth the edge to provide a good seal and

to prevent any gas leakage at the end plugs during the forming process.

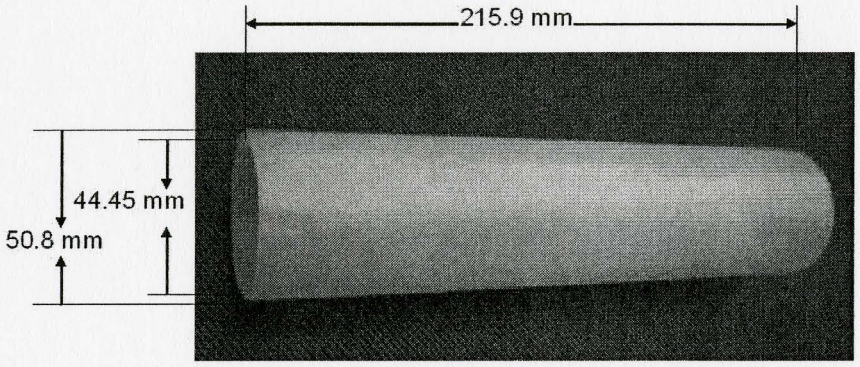

Figure 3.2: Tube specimen dimensions

For the measurement of strain distribution after the deformation process, a solid circular dot grid pattern was applied to the expansion area of the initial tubular specimens. In order to apply the grid pattern to the tube, a plastic stencil with precisely machined periodic circular holes was wrapped around the tube which was then sprayed with a mist of black ink using an air brush. On subsequent removal of the stencil, a grid pattern was obtained as shown in Figure 3.3.

After blow-drying the ink, the pattern was covered with a light coating of a powder and subsequently with a teflon tape (See Figure 3.4). This was done in order to increase the tolerance of solid circular dots to the high temperature environment and to protect them from the friction between the tube and die surfaces during the forming process. Effect of teflon tape cover on the process results assumed to be negligible since both materials are polymeric and thickness of the tape is very small.

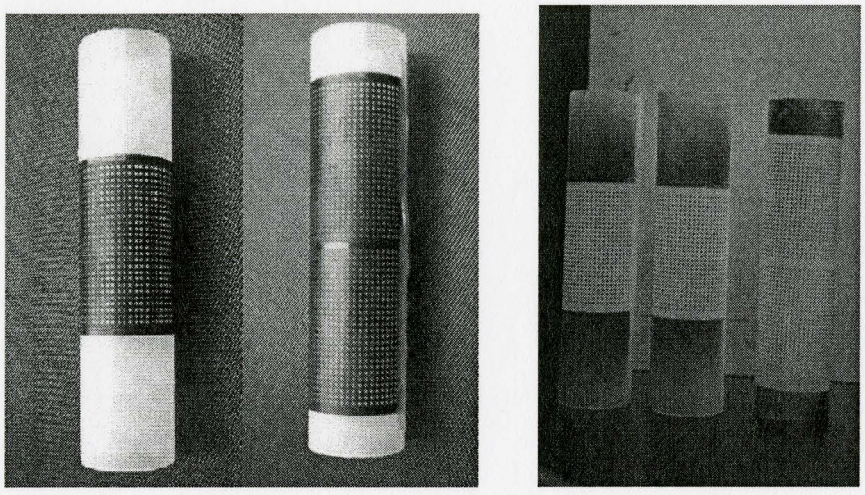

(a) Plastic stencil applied to the tube

(b) Solid circular dot grid pattern on the tube

Figure 3.3: Solid circular dot grid pattern application

3.2 Preliminary Tensile Testing Procedure

To evaluate the constitutive response of the material for the FE modeling work, i.e. thermal and rate dependencies, uniaxial tensile tests at three different rates and three different temperatures were conducted.

Uniaxial tensile tests were performed on a 25 kip (100 kN) MTS servo-hydraulic mechanical test system. A thermal chamber with high temperature test fixtures was installed on the test bed of the MTS machine to perform the tests at elevated temperatures (see Figure 3.5).

Specimens were placed in the grips of the MTS servo-hydraulic test machine at a specified grip separation (right at the beginning of the grip portion of the tensile

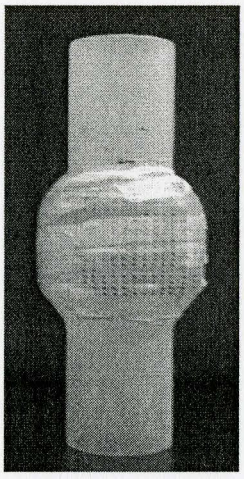

Figure 3.4: Tube covered with teflon

specimen) and tested under displacement control at 22°C, 100°C and 130°C and three actuator speeds of 2 mm/min, 10 mm/min and 50 mm/min. Digital calipers were used to measure the initial and final dimensions of the samples, gage length (l_0 and l), width (w_0 and w) and thickness (t).

To determine the strain, the initial gage length of the specimens was marked with two contrasting marks. The procedure for determining the strain during the elongation via marking technique, as well as tensile test results are presented in detail in Chapter 4. The procedure for obtaining constitutive model parameters is given in Chapter 5.

3.3 Hot Gas Tube Forming Experiments

HGTF experiments were performed on Interlaken 150 Ton Servo Press (Figure 3.6) equipped with Interlaken's UniPress control system for data acquisition and precise control of the forming process. A custom designed tube forming die with cartridge heating and rapid cooling capability were installed as the gas forming "tool pack". This tool pack was then mounted on the servo press.

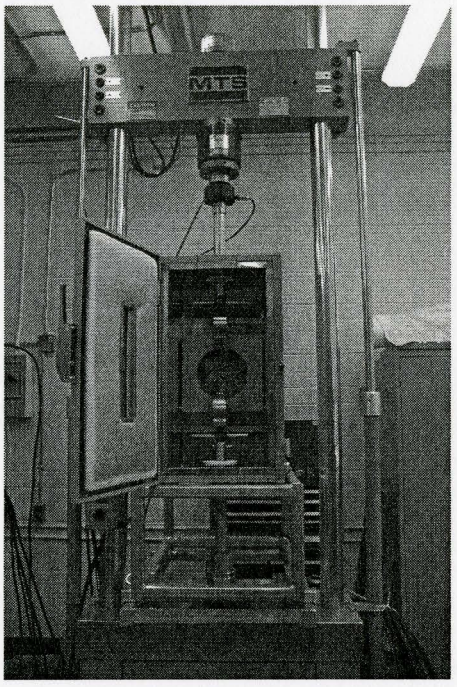

Figure 3.5: MTS tester with the environmental chamber used in tensile testing procedure

Accessories supplied for this test by Interlaken include a hydraulic actuator assembly that is mounted on the test forming bed, pressure intensifier, water tank and forming dies. For the particular HGTF of polymeric tubes application, a tube forming rig, equipped to carry out high temperature was designed in house. A nitrogen gas for tube pressurization is supplied by a pressurized cylinder fitted with a high pressure regulator. The HGTF process setup with the 150 Ton Servo press and accessories is illustrated in Figure 3.6. The press and the tool pack consisted of the following sub-systems:

1. Hydraulic press (Interlaken 150 Ton Servo Press)
2. Control and measurement system (UniPress system)
3. Actuators (front feed, back feed and clamp) and tooling (upper and lower die)

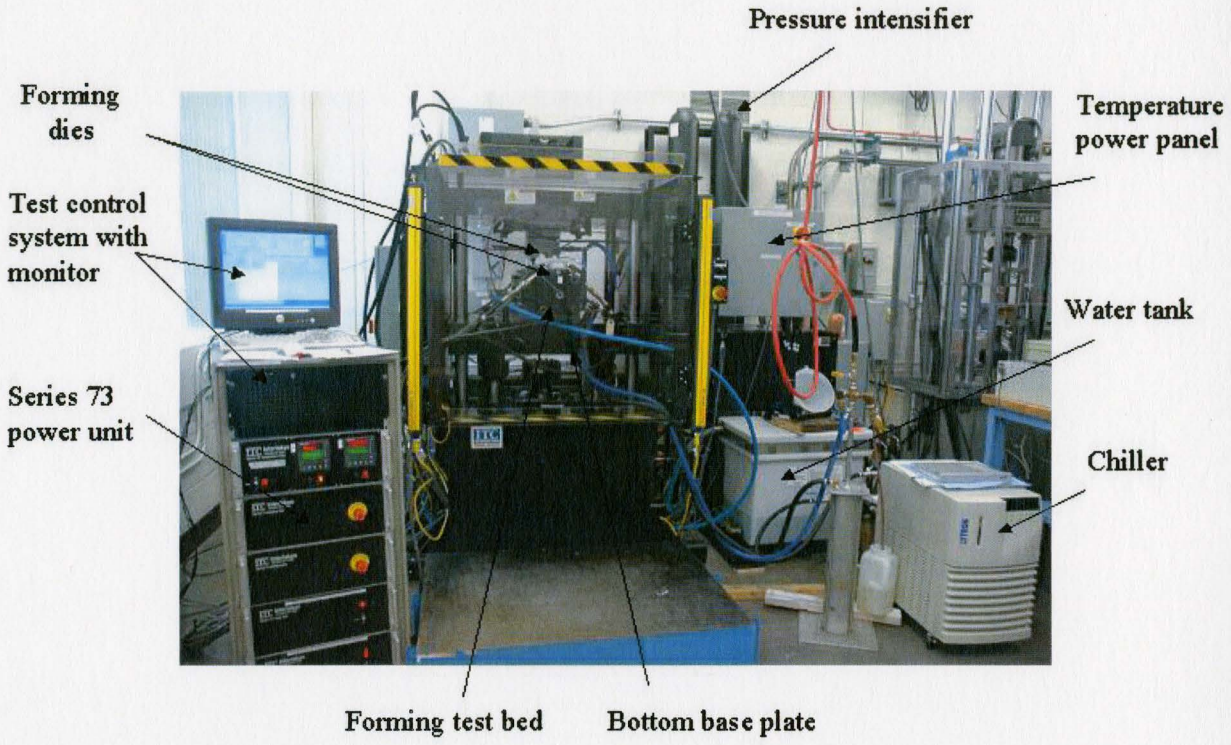

Figure 3.6: HGTF process setup

4. Heating and cooling systems

The subsystems are discussed in subsections below.

3.3.1 Interlaken 150 Ton Servo Press

Interlaken 150 Ton Servo Press is a high performance, double acting servo-controlled hydraulic press designed for laboratory use. The press dimensions are 62"x40"x76". The Servo Press 150 Ton is capable of simulating mechanical press speeds and velocity profiles at forces up to 150,000 pounds. The press is also equipped with actuator that apply a 150,000 lbf clamp load. The press is designed with T-slots on the top and bottom base plate that can easily accommodate various tooling designs.

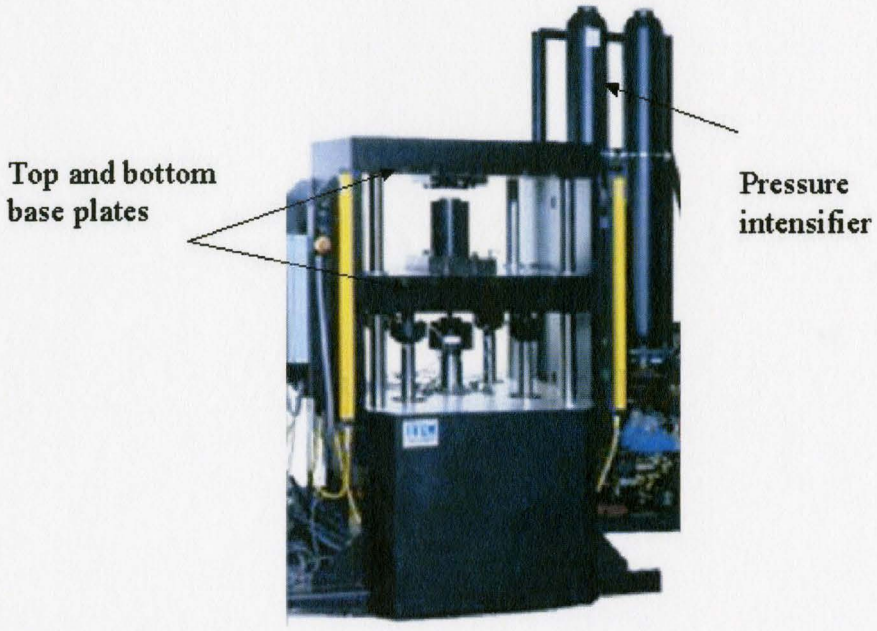

Figure 3.7: Interlaken 150 ton servo press

The process requires first clamping the initial tubular blank between the upper and lower die, then moving actuators in position control to seal the ends. Subsequent step involves forming a part by applying internal pressure and axial feed simultaneously.

3.3.2 Control and Measurement System

ProfileBuilder software available with the test control system was utilized to build displacement, pressure and force profiles using ramp, sine, dwell and other segments. The multi-channel closed loop control system was utilized to program events such as "axial done" or "dwell" as well as time dependencies.

The changes of process parameters in real time could be observed with a graphical interface (see Figure 3.8(b)). The step sequence could be performed in manual or automatic mode.

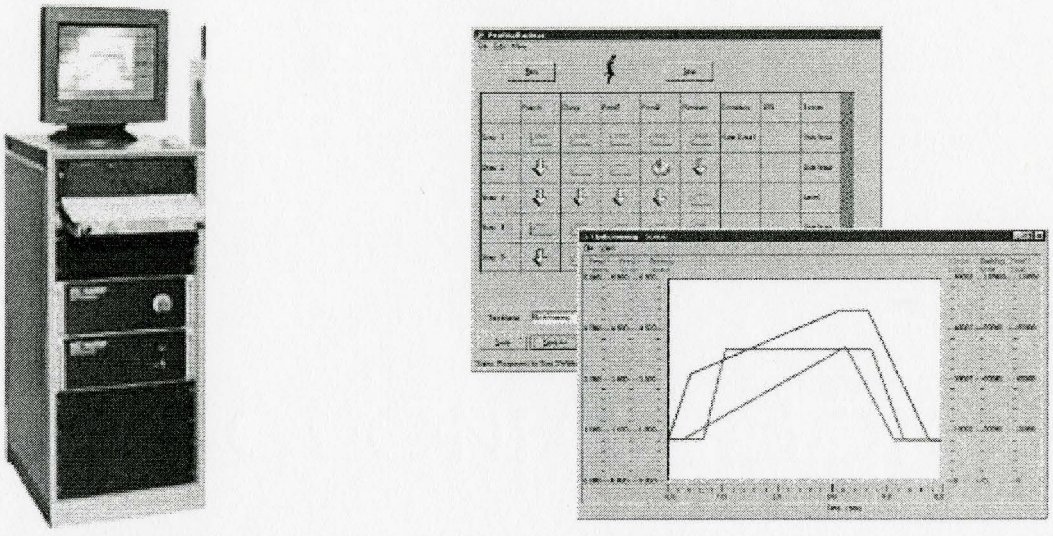

(a) UniPress Control System

(b) Screen operating window

Figure 3.8: UniPress control system and screen operating window for interlaken press

3.3.3 Actuators and Tooling

Actuators and tooling for the ServoPress 150 were designed originally by Interlaken for the purpose of the HGTF experiments. Subsequent modifications to the tooling to redesign the die heating system and an addition of the die cooling system were carried out by Dr. Mike Bruhis of MMRI. Design and operation of the actuators and tooling pack are explained in the subsections below.

Actuators

As mentioned earlier, the Interlaken press was equipped with three actuators: front feed actuator, back feed actuator and clamp actuators (see Figure 3.9). The bottom base plate of the Interlaken press was supported by four interconnected clamp actuators placed at four corners of the base plate. After placing the initial tube specimen

in the die cavity, the clamp actuators were moved to bring the bottom base plate to "close die" position. After the forming process, the clamp actuators were moved down to bring the bottom base plate back to initial "open die" position.

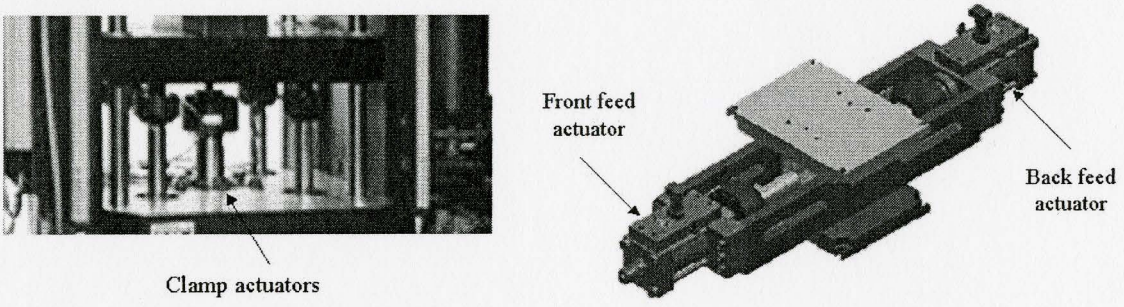

(a) Vertical actuators for lower die motion

(b) End sealing and feed actuators

Figure 3.9: Front feed and back feed actuators

Front feed and back feed actuators lay in the tube forming tool pack (forming bed) placed on the bottom base plate of the press and act simultaneously. At the beginning of the forming process, they move the docking rods towards the middle of the tube to the position "seal" with the tube ends. During the forming process, front and back actuators feed the tube material into the die cavity. At the end of the process, they are retracted to the initial position.

Tooling Setup

The HGTF die set consisting of upper and lower halves are shown in Figure 3.10.

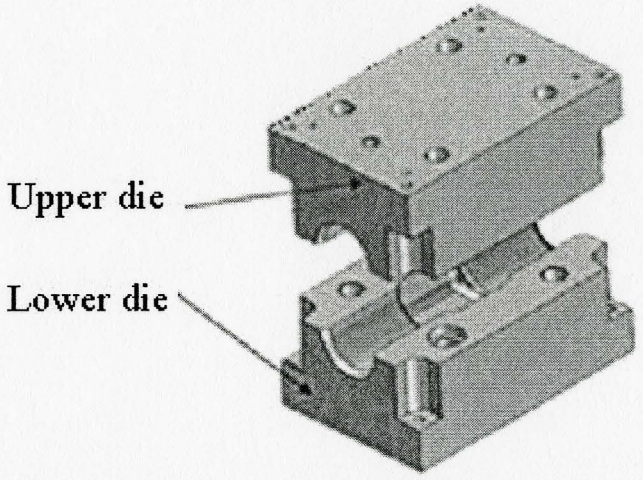

Figure 3.10: Upper and lower dies

The dies are positioned in the forming bed between the front feed and back feed actuators. The dies are also fitted with changeable inserts for different cavity shapes and can be run with or without end feed from the two end feed actuators. Using these dies, along with the control and data acquisition capability of the ServoPress, allowed a study of the effect of various pressures and end feeds for a specific component geometry (see Figure 3.11) to provide a good understanding of the material flow behavior in the die cavity. The die cavity of the tool pack utilized in the present research allowed the tube expansion ratio up to 60 percent. The total strains achieved in tensile tests showed that this is a reasonable expansion ratio for PP material used in this study.

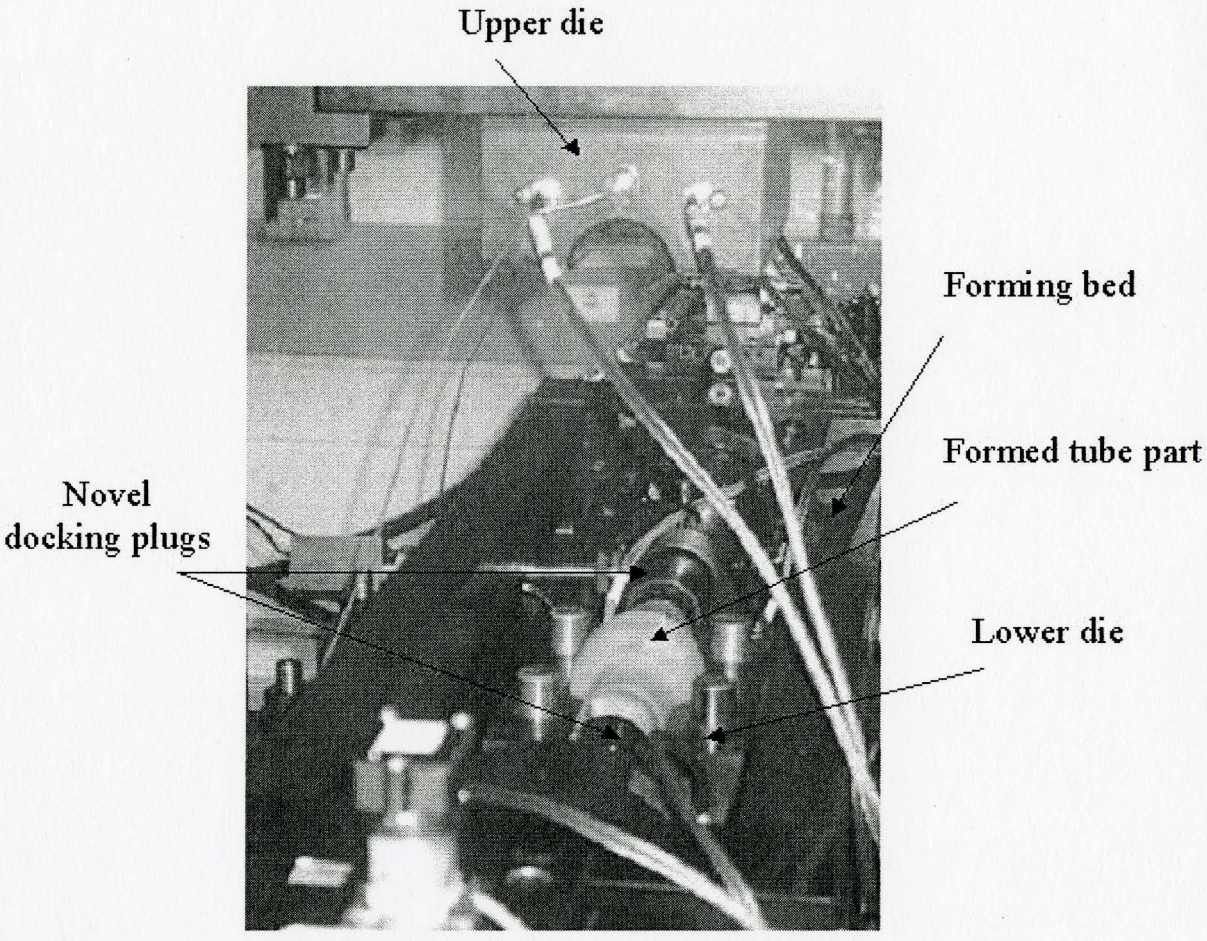

Figure 3.11: Tooling setup

3.3.4 Heating and Cooling System

For the purpose of the experiments, the tooling (upper and lower die) was equipped with a cartridge heating system from the supplier. During the experiments, to improve the quality of the final product, a cooling system was also added. Due to the custom installation of the cooling system, the heating system was also modified and reinstalled.

Heating System

As mentioned before, engineering polymeric material properties, in general, are highly temperature dependent. To achieve better formability and material flow for PP tube, the forming process was conducted at elevated temperature of 110°C. To serve this purpose, the system was equipped with a die heating capability with a working range up to 250°C. The dies were outfitted with two heating elements and thermocouple in the front and back side of each die. The front view of the upper die with heating elements and thermocouple is presented in Figure 3.12.

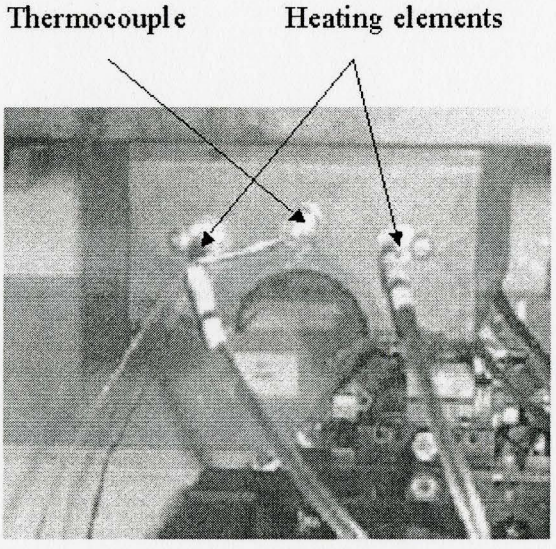

Figure 3.12: Die set with heating elements

Cooling System

To improve the quality of the final part and the process performance, the cooling step was added to the process sequence.

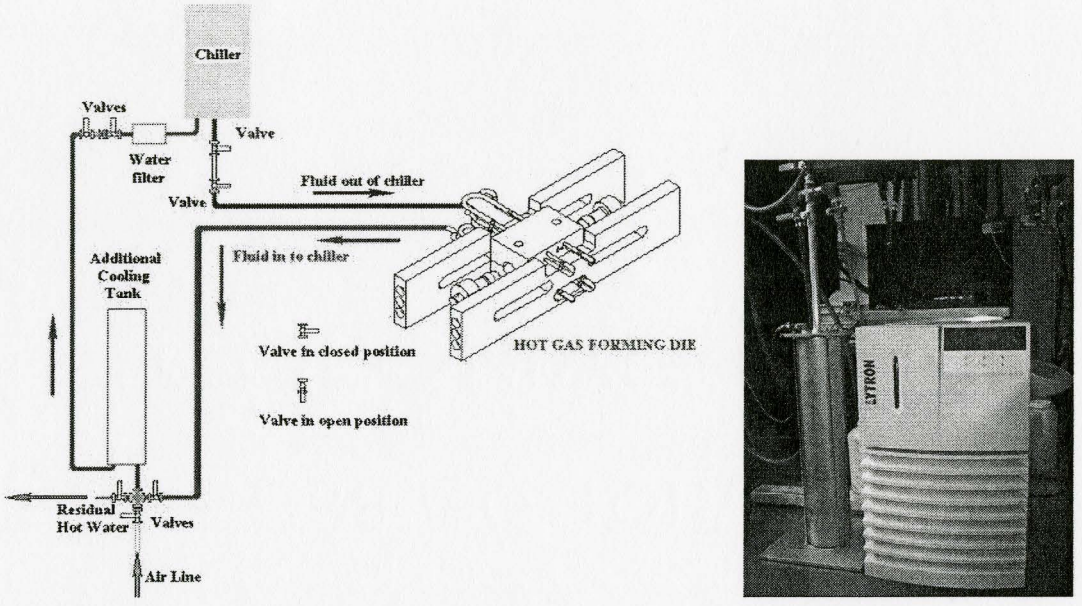

(a) Water Cooling System schematic diagram

(b) Kodiak Chiller 800W-6000W

Figure 3.13: Water cooling system

The cooling system consists of a chiller from Kodiak Chillers (Model 800W-6000W, Figure 3.13), a refrigeration system, a water line, associated controls and plumbing. The pump draws cold water from the internal reservoir and pumps it out to cool the hot gas forming die, and then the coolant flows back to the chiller. It flows through additional cooling tank and through the evaporator, where the heat is removed, and then flows back into the reservoir. Chiller is designed to operate with continuous coolant flow through a closed loop. This loop contains the system pump, temperature sensor, reservoir, internal and external plumbing lines and fittings (Figure 3.13(a)).

To provide rapid cooling to the tooling pack, initial die set was retrofitted with the several cooling channels that were placed close to the center of the die (see Figure

3.14). The positions of the cooling channels were selected based on the process flow understanding and previous experimental trials.

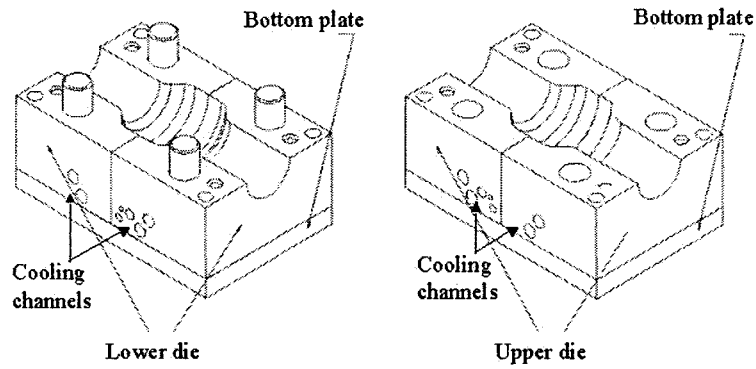

Figure 3.14: Tooling die set with cooling channels

3.3.5 Process Steps

At the beginning of the process, to achieve a more uniform temperature distribution in the tubular specimen through the tube wall thickness, the specimens were preheated in the oven. The prepared tubes specimens with the applied grid speckle and covered with the teflon were placed in the oven at 110°C for 20 minutes. The temperature of the tube specimens was also measured with an external thermocouple to assure the accuracy of the specimen temperature distribution.

The axial-feed HGTF process consisted of several steps:

1. Transferring preheated tube specimen from the oven tube into the die cavity, closing the die and applying the clamping force.
2. Moving the front and back feed actuators in position control towards the two ends of the tube for sealing.

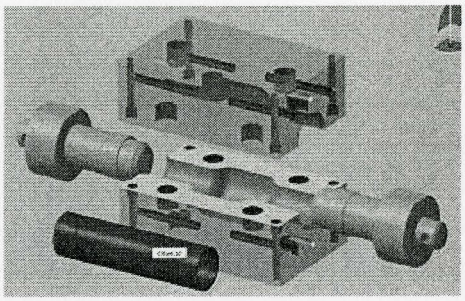

(a) Initial tube blank at the beginning of the process

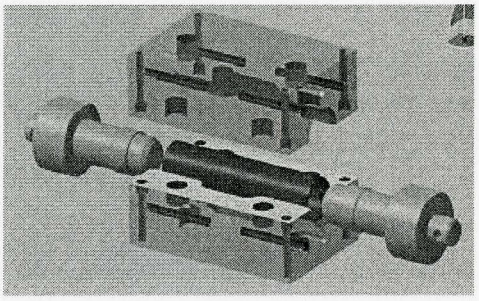

(b) Beginning of the forming process, tube placed into the die cavity

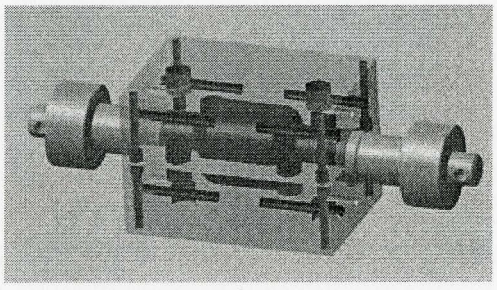

(c) Forming step of the process

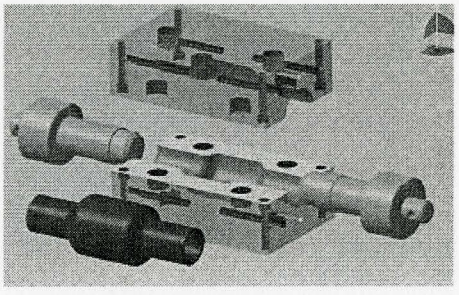

(d) End of the forming process, final formed part

Figure 3.15: Process steps (sketches are courtesy of Mike Bruhis, MMRI)

3. Applying initial sealing pressure at the ends of the tube by injecting nitrogen gas from a pressurized cylinder.

4. Simultaneously applying the internal pressure and actuator displacements to the tube ends feeding in a ramp step to carry out the forming of the part.

5. Calibration phase of the process with the simultaneous cooling of the die. In this step, the tube conforms to the die shape under constant internal pressure only. This is achieved by setting the dwell time in the event procedure. Rapid cooling is performed by the the circulation of the cold water through the die.

6. Depressurization of the tube.

7. Retraction of the end feed actuators to the initial position and moving the clamp actuators into "open die" position.

The major parameters of the forming process are the internal pressure and axial feed. The pressure is applied in two steps. The first step is initial pressurization of the tube or sealing. The necessity of this step is important because of the initial imperfections of the tube ends. It is undesirable to bring the docking rods too far in the sealing position. The material at high temperatures is very soft and any exceeding pressure will cause the buckling of the tube. However, if the tube is not sealed properly by the docking rods, the gas leakage might appear and the internal pressure will not be able to reach the set point. Applying initial sealing pressure and absence of leakage confirms that the tube ends are sealed properly. The axial feed is applied in displacement control. Feeding and retraction are controlled using the event control setting.

3.4 Argus Optical Measurements System

An optical strain measurement system (Argus system from GOM) was utilized to analyze post-formed component using the surface imprinted deformed grid pattern.

The Argus system consists of a PC with monitor, interconnecting cables and camera. In the Argus system, a camera takes digital images of the deformed tube from different angles and distances around the part. A PC-based dedicated software then calculates 3D coordinates for every dot on the surface of the specimen, and compares them with the coordinates of the undeformed state that can be synthetically generated by the computer due to the simplicity of the pattern. By calculating the shift of

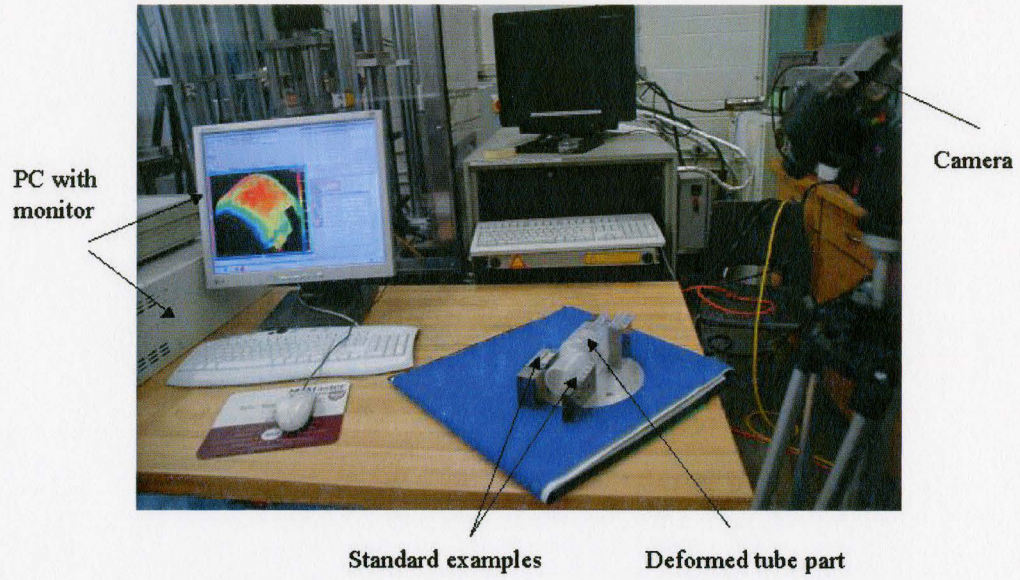

Figure 3.16: Argus optical strain measurement system

the object characteristics, the resulting strain can be derived using well established grid strain analysis procedures.

To take images and make proper measurements, the formed tube was placed at a certain distance from the camera. For the pattern comparison and grids deformation measurement, several pieces of standard examples with the initial standard dot pattern were placed at a particular distance from the deformed part (Figure 3.16). During the measurements, the part was rotated and the images were taken from the different angles and distances from the deformed tube. After the measurements, the images were analyzed and a plot of of major and minor strains distribution in the expanded region of the specimen was constructed.

In this chapter, experimental procedure of HGTF of PP, testing equipment as well as process steps were introduced. Preliminary tensile testing procedure and samples preparation are presented in the next chapter.

Chapter 4

Experimental Results

Test results consists of preliminary tensile stress-strain results and HGTF process results. HGTF tests were conducted according to the designed test matrix. Tests results in terms of tube wall thickness distribution after deformation were obtained manually using a micrometer whereas major and minor strain distributions at the surface were measured by Argus optical strain measurement system described earlier.

4.1 Tensile Tests Results and HGTF Test Matrix

A photograph of typical tensile specimen is shown in Figure 6.22(b) below. Procedure to determine the actual strain from the gage markings is explained in details in Appendix A.

True stress-true strain curves for three different temperatures and strain rates were obtained from tensile data. These curves are shown in Figure 4.2. The graphs show that at lower temperatures, material has a higher elastic modulus compared to higher temperatures.

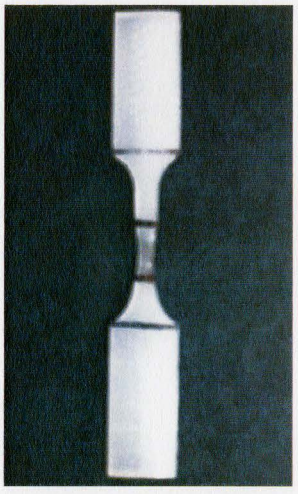

Figure 4.1: Tensile specimen after elongation

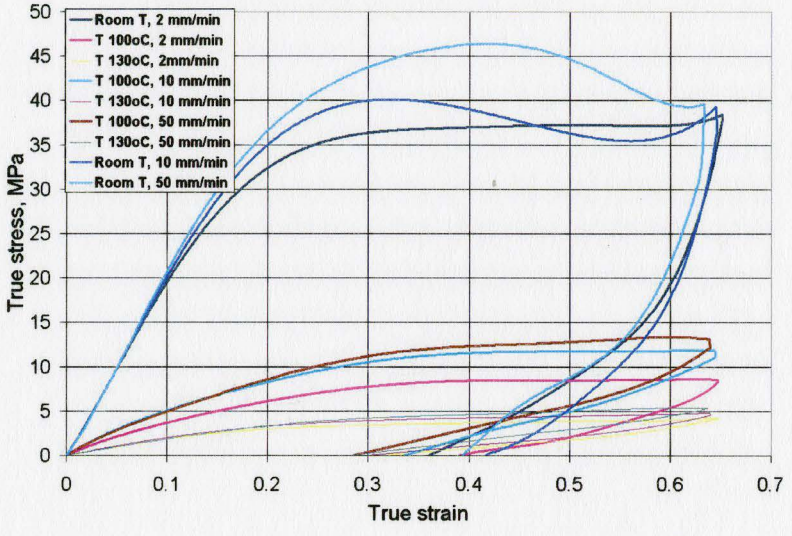

Figure 4.2: True stress-true strain input data curves

As the temperature increases, the material has a steady state flow stress. Also, higher the strain rate or actuator velocity, higher is the stress and vice versa. For the chosen test parameters, the highest material stress is at room temperature and at an actuator velocity of 50 mm/min. The lowest stress is at 130°C and at an actuator velocity

of 2 mm/min.

To develop a "window" with suitable range of process parameters the tube forming experiments were first conducted by trial and error based on the data from tensile tests. The main criteria were the minimization of the thickness deviation of the tube walls along the length of the tube and an acceptable final tube shape. Preliminary experiments showed that the acceptable tube expansion was achieved at 1.5 MPa to 2.5 MPa of internal pressure and 16 mm to 19 mm of axial feed (or displacement). To find the optimal combination of parameters based on the preliminary results, the following test matrix was constructed.

Case	**Internal pressure**	**Axial feed**
1	1.227 MPa	17.78 mm
2	1.227 MPa	25.4 mm
3	2.165 MPa	19.05 mm
4	2.165 MPa	29.21 mm
5	2.165 MPa	15.24 mm
6	2.165 MPa	17.78 mm

Table 4.1: HGTF test matrix

Six experimental cases with various combinations of internal pressure and axial displacement based on the preliminary trial and error results were carried out (See Table 4.1). The following subsection introduces the process parameters profiles and tube wall thickness and major and minor strain distribution for each of these cases.

4.2 Process Parameters vs. Thickness Distribution

The test cases were conducted with different combination of internal pressure and axial displacement as shown in Figure 4.3. In all cases initial sealing pressure of 0.207 MPa was applied to the tube specimens. Initial load was applied in a way of sealing pressure to ensure that there is no gas leakage and the tube ends are sealed properly. Summary with tests parameters with description of the formed tube shape results and photographs of the formed tubes are represented in Table 4.2 and Figure 4.4 respectively.

In case 1, Figure 4.4(a), the level of internal pressure was slightly lower than optimal pressure level, although the axial displacement was within an acceptable range. As a result, the tube walls did not come in contact with the die and tube diameter did not reach the full expansion. In case 2, the level of internal pressure was maintained the same, but the axial feeding was increased. With slightly over the range axial displacement, wrinkling formation started at the beginning of the process (Figure 4.4(b)). Since the level of internal pressure was not sufficient for the full tube expansion, the wrinkles remained on the final tube shape. In case 3, the value of internal pressure was increased to the optimal range, however, the axial displacement still remained slightly over the desirable level. In this case, buckling initiation was observed (Figure 4.4(c)). Although the tube seemed to have full expansion and acceptable shape, the critical tube wall points at the beginning of the expansion zone showed thickening which indicates the beginning of the buckling failure process.

In case 4, the internal pressure remained the same and within the optimal range, but the axial feed was increased significantly for the purpose of having a better visual results of the buckling failure. As it is demonstrated in the Figure 4.4(d), exces-

Case	Internal pressure	Axial feed	Description of formed tube
1	1.227 MPa	17.78 mm	Tube did not form the shape of the die
2	1.227 MPa	25.4 mm	Wrinkling
3	2.386 MPa	19.05 mm	Buckling initiation
4	2.165 MPa	29.21 mm	Buckling
5	2.275 MPa	15.24 mm	Thinning
6	2.165 MPa	17.78 mm	Part shape conforms to the die shape

Table 4.2: Test matrix results

sive tube feeding pushed the tube ends inside the die cavity and caused the common buckling failure. In Case 5, excessive thinning occurs at the same level of internal pressure and small axial feed, leading to strain localization and tube bursting (Figure 4.4(e)). Deviation between the wall thickness of the middle part of the tube and the wall thickness at the ends was slightly higher than acceptable. Finally, in case 6, the values of internal pressure was the same at 2.165 MPa and an axial displacement of 17.78 was applied. This case represents the best achieved result with respect to the tube wall thickness uniformity (Figure 4.4(f)).

A comparison of tube wall thickness distribution for the cases above is shown in Figure 4.5. To increase the accuracy and to avoid measurement mistakes due to the measurements errors, all the measurements were performed 3 times on each specimen. The final value was taken as a mean value of the three measurements. Calculation of mean value and standard deviation is shown, as an example of case 1, in Figure 4.6. Standard deviation and mean value for all cases are demonstrated in Appendix B.

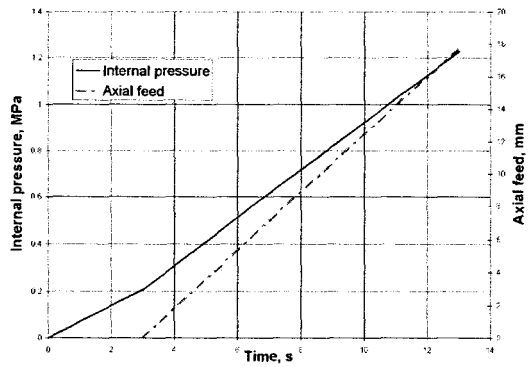

(a) Case 1

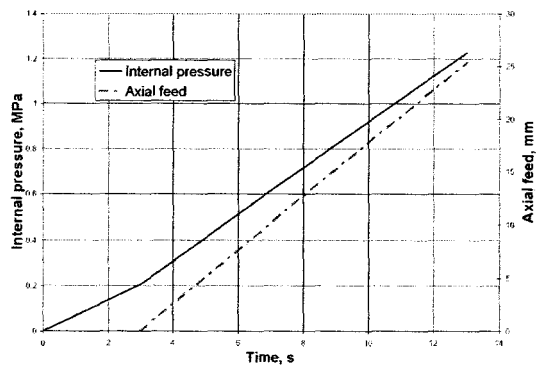

(b) Case 2

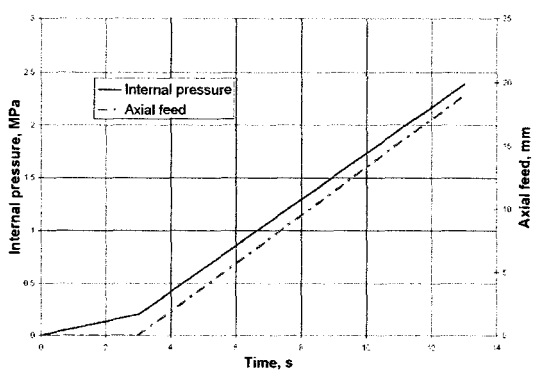

(c) Case 3

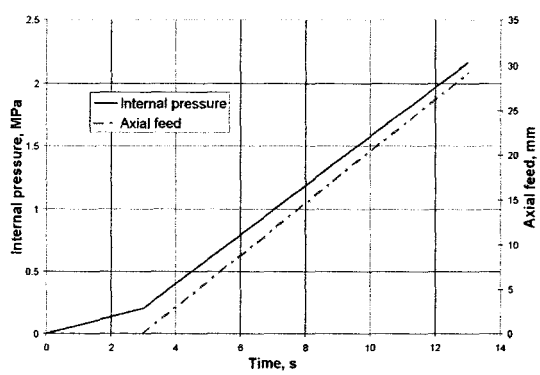

(d) Case 4

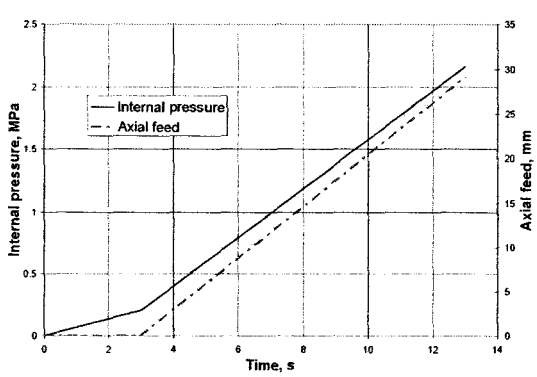

(e) Case 5

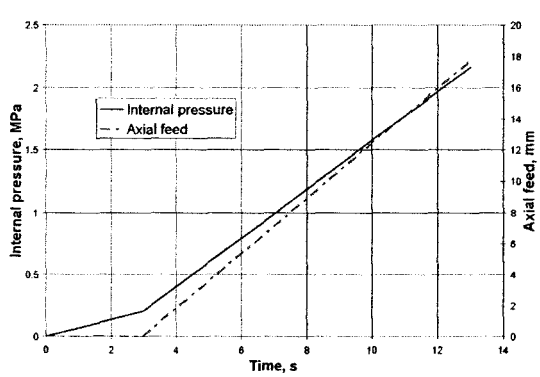

(f) Case 6

Figure 4.3: Internal pressure and axial feed versus time curves for the different test cases

(a) Tube didn't form the shape of the die (Case 1)

(b) Tube wrinkling (Case 2)

(c) Tube buckling initiation (Case 3)

(d) Tube buckling (Case 4)

(e) Tube Thinning (Case 5)

(f) Part shape conforms to the die shape (Case 6)

Figure 4.4: Experimental results

Case 1 is the case when the tube did not form the shape of the die due to insufficient amount of internal pressure. Despite the positive results, this case was not considered as the optimum, as the desired shape was not achieved. Case 2 resulted in wall tube wrinkling. The tube wall thickness in the middle part of the tube had a value of 3.5 mm, which indicated tube thickening. An increased tube wall thickness at the critical points was obtained for case 3. Those are the points of buckling initiation, when the displacement was not large enough to push the tube further into the die cavity.

Case 4 resulted in quite a uniform thickness distribution. However, this is the case of buckling failure and it is not considered in the estimation of the optimal process parameters. The minimum tube wall thickness of 1.9 mm in the center part of the tube specimen was measured in case 5. Case 6 shows an acceptable deviation in the 0.5 mm - 0.6 mm range in thickness distribution between the tube ends and the middle portion of the tube specimen. The region close to the ends has almost uniform tube wall thickness distribution of approximately 3.45 mm. The center of the tube specimen has uniform wall thickness distribution of approximately 2.85 mm. Experimental results and comparison of tube wall thickness distribution data with FE models are summarized in Chapter 6 (Table 6.2).

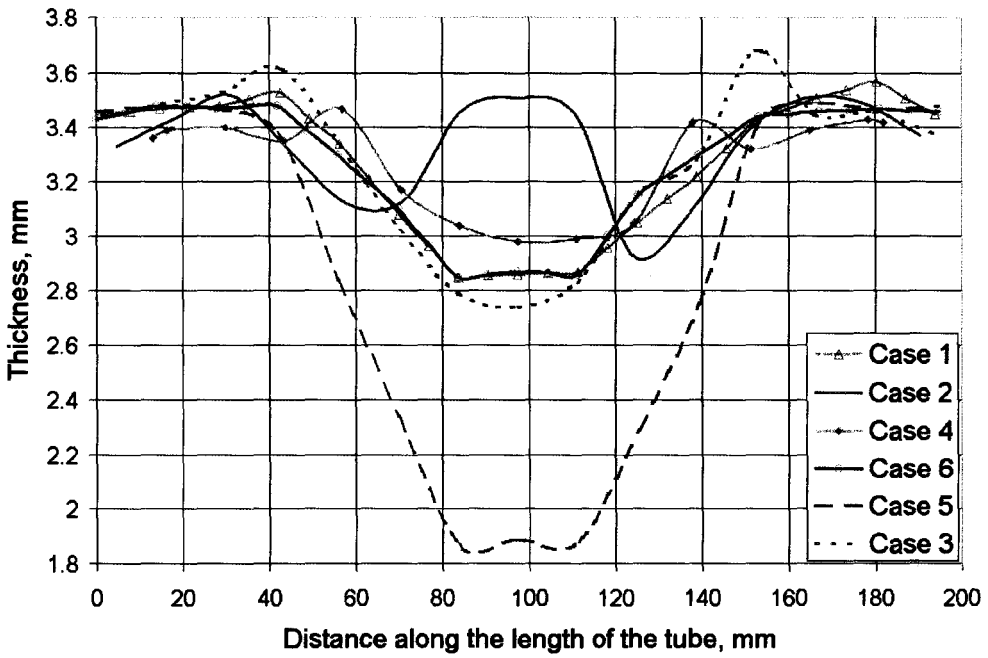

Figure 4.5: Comparison of the tube wall thickness distribution along the length of the tube

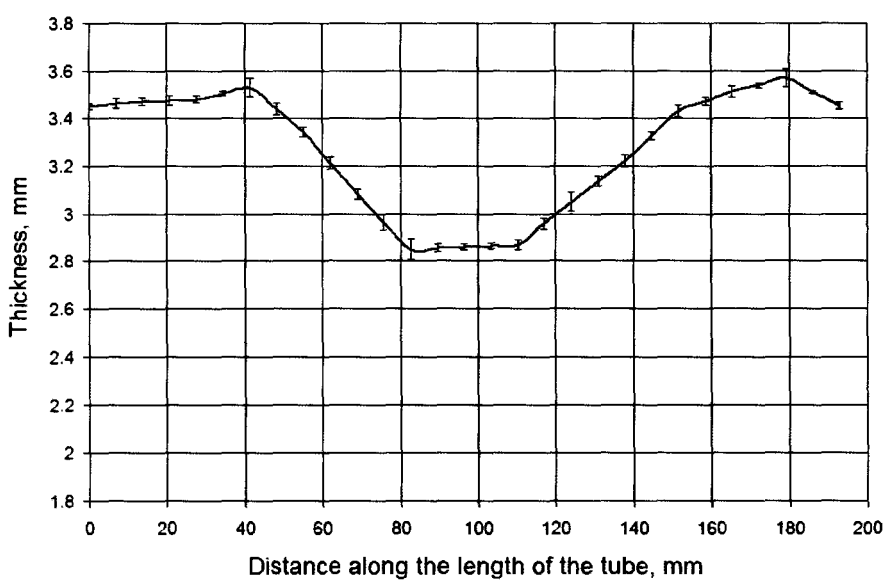

Figure 4.6: Relative measurement error and STD (case 1)

4.3 Process Parameters vs. Major and Minor Strain Distribution

Major and minor strain distributions were measured on the tube specimens after deformation in the central part of the tube, where the grids on the specimen were intact (or undamaged).

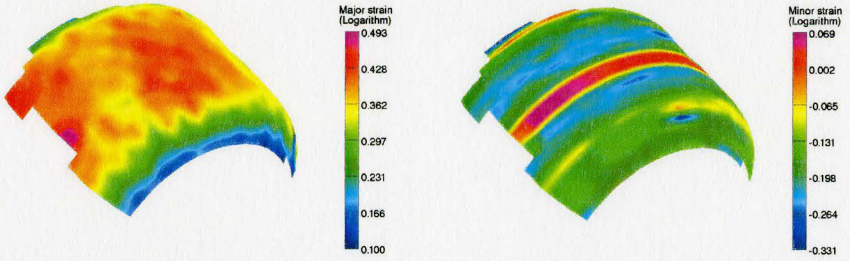

(a) Major strain distribution (b) Minor strain distribution

Figure 4.7: Experiment. Case 1 (pressure 1.227 MPa, feed 17.78 mm)

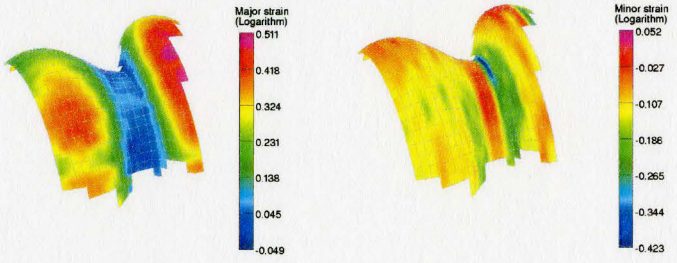

(a) Major strain distribution (b) Minor strain distribution

Figure 4.8: Experiment. Case 2 (pressure 1.227 MPa, feed 25.4 mm)

The results show that the strain distribution on the tube surface after deformation

is not quite uniform in many of the cases. There are visible areas of major strain concentration in the hoop direction, especially in cases with higher internal pressure (Cases 3 and 6). This phenomenon shows anisotropy of material and is perhaps due to microstructure inhomogeneity of tube samples. Case 2 shows a very small value of major strain of about 0.03 in the central part, where the tube was not able to expand due to the small amount of internal pressure and comparably large value of axial displacement. However, the wrinkles show a much higher major strain value of about 0.4.

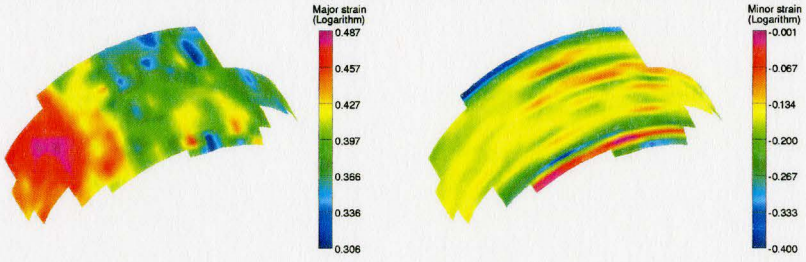

(a) Major strain distribution

(b) Minor strain distribution

Figure 4.9: Experiment. Case 3 (pressure 2.165 MPa, feed 19.05 mm)

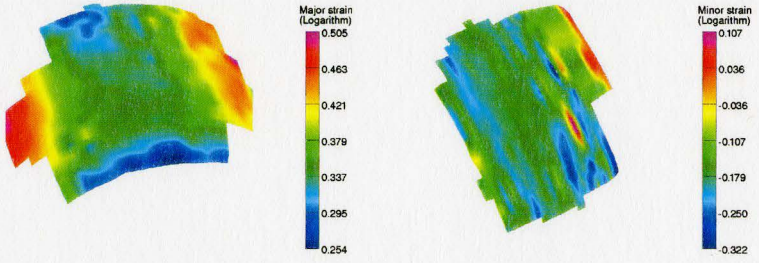

(a) Major strain distribution

(b) Minor strain distribution

Figure 4.10: Experiment. Case 4 (pressure 2.165 MPa, feed 29.21 mm)

Minor strain distribution shows more uniformity, than major strain distribution. However, there is an interesting phenomenon in Case 1, where the minor strain shows a stable small positive value of 0.002 across a narrow region in a hoop direction, while the majority of the expanded region shows a negative value of approximately -0.22. Experimental results and comparison of major and minor strain distribution data are summarized in Chapter 6 (Table 6.3) along with the results of numerical simulations.

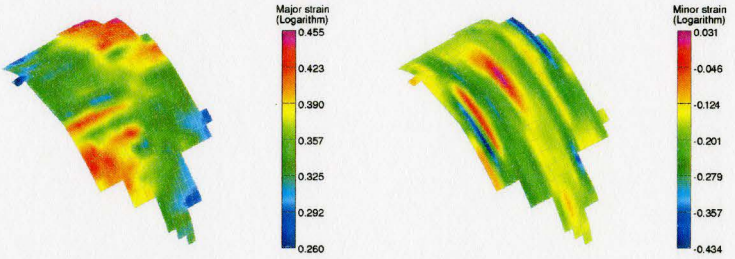

(a) Major strain distribution

(b) Minor strain distribution

Figure 4.11: Experiment. Case 5 (pressure 2.165 MPa, feed 15.24 mm)

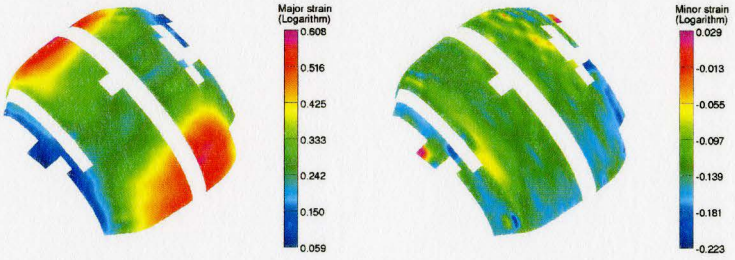

(a) Major strain distribution

(b) Minor strain distribution

Figure 4.12: Experiment. Case 6 (pressure 2.165 MPa, feed 17.78 mm)

Chapter 5

Numerical Simulations Procedure

5.1 Finite Element Formulation

Non-linear Explicit FE Method is employed to simulate the HGTF process. Non-linearities arise from material behavior at large deformations. The basic idea of the nonlinear FE formulation is to linearize the equations of the problem and to solve them for the FE discretized domain. This is done with implementation of incremental approach, which means that the solution at each step is being obtained from the solution at the previous step. By the definition of the step it is understood a load increment in static analysis, and a time step in transient analysis [53; 54; 55]. The time increment size depends solely on the highest natural frequencies of the model and is independent of the type and duration of loading. Generally, the problem requires many small increments to obtain a converged solution.

The explicit dynamic method was originally developed to analyze high speed dynamic events. However, for a variety of reasons, it is very efficient in solving certain types of quasi-static problems, such as in metal and polymer forming. The forming

analysis includes determination of stresses, strains and displacements in the deforming object, wrinkling, buckling and complex frictional contact conditions. The latter possibilities are better solved with Explicit FE method.

Commercial package, Abaqus/Explicit, is used to run the simulations. Abaqus/Explicit utilizes the central difference rule to integrate the equations of motion explicitly through time. Kinematic conditions at one increment are being used to calculate the kinematic conditions at the next increment. The first step of the algorithm involves solving for the dynamic equilibrium:

$$\ddot{u}_{(t)} = M^{-1}\left(P_{(t)} - I_{(t)}\right) \tag{5.1}$$

which states that the nodal mass matrix, M, times the nodal acceleration, $\ddot{u}$, equals the total nodal forces (P-I). The accelerations are integrated explicitly through time using the central difference rule, which calculates the change in velocity assuming that the acceleration is constant.

$$\dot{u}_{(t+\frac{\Delta t}{2})} = \dot{u}_{(t-\frac{\Delta t}{2})} + \frac{\left(\Delta t_{t+\Delta t} + \Delta t_{(t)}\right)}{2}\ddot{u}_t \tag{5.2}$$

Then the velocities are added to the displacements at the beginning of the increment to determine the displacements at the end of the increment.

$$u|_{(t+\Delta t)} = u|_{(t)} + \Delta t|_{(t+\Delta t)}\dot{u}|_{(t+\frac{\Delta t}{2})} \tag{5.3}$$

Next step is the computation of element strain increments ($d\varepsilon$) from the strain rate ($\dot{\varepsilon}$) and stresses (σ) from constitutive equations.

$$\sigma_{(t+\Delta t)} = f(\sigma_{(t)}, d\varepsilon) \tag{5.4}$$

The last step is assembling nodal internal forces $I_{(t+\Delta t)}$, setting $\sigma_{(t+\Delta t)}$ to σ_t and returning to the first step.

The process of building FE model in Abaqus consists of the preprocessing and post-processing mode. In preprocessing, the procedure is divided into several modules that are described in the following subsections. The following assumptions were made during the preparation of the FE model input.

1. The material of the tube follows one of the chosen constitutive material models (See Section 2.4.5)
2. The material of the die is rigid
3. The displacements of left and right actuators are equal
4. The temperature of the tube and the die is constant and uniformly distributed
5. The initial thickness of the tube is uniform
6. The internal pressure is applied in a ramp step and is distributed uniformly from the beginning

5.1.1 Die-Tool Geometry

The model geometry consists of 2 components: the die with a radius of the central cavity of 45 mm and the tube. The outer and inner diameters of the tube are 50.8 mm and 44.45 mm and the length is 215.9 mm. The die is modeled as a 3D or 2D discrete rigid body and the tube is treated as either a 3D or an axisymmetric 2D deformable solid respectively. Due to the symmetry, only one-eight of the 3D geometry is analyzed. For convention, different sets of surfaces were created, which were used in assigning loads, boundary conditions and contact properties to the two components. Die-tube geometry and corresponding loads and boundary conditions are presented later in Figure 5.1.

5.1.2 Material Model Implementation

Axial-feed HGTF process was simulated with two different FE material models: Ogden and AHM.

Ogden Hyperelastic Model

The hyperelastic Ogden material model was implemented into the FE model through tensile stress-strain data. Engineering tensile stress-strain curve was calibrated by Abaqus software [29] to determine the accuracy of curve fitting and material model coefficients (See Figure 6.1). Material model coefficients are presented in Appendix A.

Augmented Hybrid Model

In present work, Augmented Hybrid constitutive model has been utilized in the FE simulation of polypropylene. The loading and unloading behavior has also been investigated (See Chapters 6 and 7). Incorporation of AHM material model into the FE model was implemented through the user material model (VUMAT) in Abaqus Explicit code. Experimental tensile true stress-strain data was calibrated and calibration coefficients were received directly from Dr. Bergstrom [56] and integrated into FE model through the VUMAT. Experimental tensile true stress-strain data with the fitted AHM material model curves are shown in Chapter 6 (Figure 6.1). Material model coefficients and description are presented in Appendix C.

5.1.3 Tooling Motion and Boundary Conditions

A master slave contact approach was used in the analysis where the die (rigid surface) is considered as the master surface, and the outer surface of the tube (Outer tube) is considered the slave surface. This type of the surface contact is referred to as a "contact pair" in Abaqus with kinematic mechanical constraint.

The load was applied to the tube in three steps: The first step is the so-called pre-pressurization or application of the initial sealing pressure (0.207 MPa) to the inner side of the tube (Inner tube). The second step is the process expansion phase where a maximum pressure is applied. The third step is the process calibration phase with a constant maximum value of internal pressure. The axial load at the tube ends is applied during the process expansion phase with a linearly varying amplitude and referred to as "ramp" amplitude in Abaqus.

In 3D case, there are four parts where boundary conditions are applied initially. Due to the symmetry, the front surface of the tube (Front) is restricted in U_2 direction. The back surface of the tube (Back) is restricted in U_3 direction. The left side surface of the tube (Left side) is restricted in U_1 direction. The rigid surface (Die) is constrained in all directions by its reference point and has zero degrees of freedom. In the second step, various values of axial displacement are assigned to the ends of the tube in U_2 direction. The same value of axial displacement is utilized in the third step. Internal sets and surfaces of the tube and the die with the corresponding loads and boundary conditions are presented in Figure 5.1.

In axisymmetric 2D case, the first step of boundary conditions assignment consists of the restriction of front surface (Front) of the tube in U_2 direction and constraint with zero degrees of freedom of the die rigid surface through its reference point. In

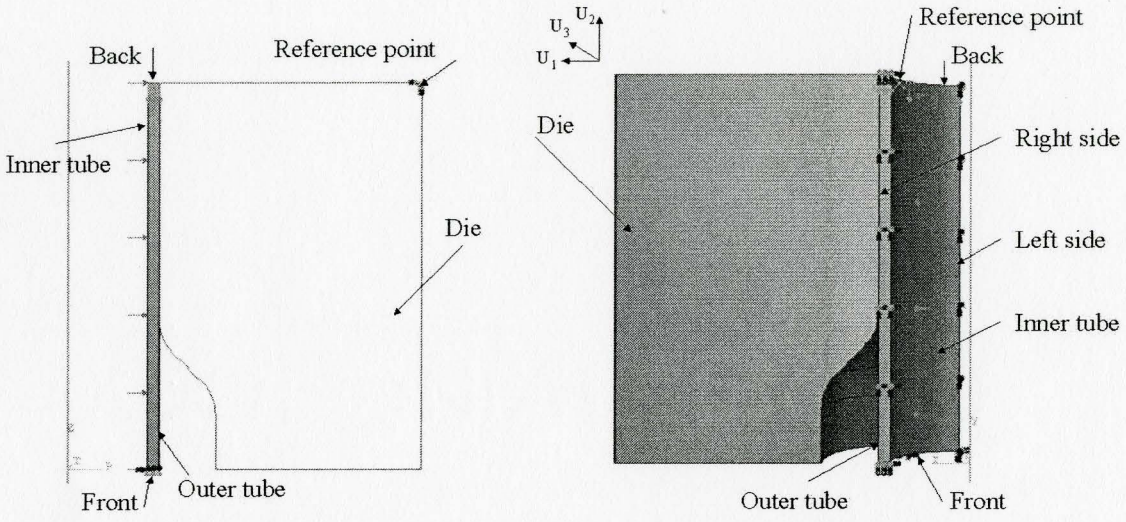

(a) Boundary conditions for 2D axisymmetric model

(b) Boundary conditions for 3D model

Figure 5.1: Boundary conditions

a second step, various values of axial displacement are applied to the back surface of the tube. In the third step, as earlier, all constraints are utilized with the same value as assigned in the previous step.

5.1.4 Finite Element Mesh

Finite element mesh was assigned to both: the tube and the die. In 3D case, tube was meshed with 3D stress structured an eight-node linear brick, reduced integration C3D8R elements with hourglass control. The die was meshed with a four-node 3D bilinear discrete rigid quadrilateral shell elements. In 2D axisymmetric model case, the tube was meshed with 2D axisymmetric stress a four-node bilinear axisymmetric quadrilateral, reduced integration CAX4R elements with hourglass control. The die was meshed with a two-node linear axisymmetric discrete rigid link RAX2 elements.

5.2 Unloading Step

Unloading step of HGTF has been incorporated for the first time with AHM material model (no such attempt has been noted in the literature). Process was simulated with four steps, as it is in the actual experiment.

1. Preloading step (initial sealing pressure is apllied internally to the tube to identify for gas leakage
2. Loading or process expansion (full value of internal pressure is applied together with the tube ends axial displacement)
3. Dwell or process calibration
4. Unloading or depressurization (Internal pressure is removed as well as tube ends constraints to account for the tube unloading and springback)

Simplifications were made in this case. Simulation did not account for the cooling step as it is in the actual process. Process unloading was simulated at the same elevated temperature as the forming (or loading) process.

In summary, this chapter introduced the FE simulation procedure of HGTF. Development of FE models and FE formulation of model parameters were discussed. Two different material definitions for hyperelastic and viscoelastic-viscoplastic materials were presented. Unloading step was added to the FE model with AHM material model formulation and the process steps with unloading were discussed. Results of FE simulations of HGTF process are presented in the next chapter.

Chapter 6

Numerical Simulation Results and Comparison with Experimental Data

This chapter deals primarily with FE simulations of HGTF tests. A set of FE models were developed based on careful consideration of numerical parameters from a sensitivity analysis of the FE models. For this purpose, comparisons were made of Abaqus Explicit vs. Implicit material model responses, 3D vs. 2D axisymmetric model, friction coefficient value, mass scaling, tube end displacement sensitivity as well as the effect of mesh size and mesh density. Various HGTF test cases presented earlier were simulated with 3D and 2D axisymmetric Ogden and AHM material models using the Abaqus FE code. Thickness distribution along the length of the tube and major and minor strain distribution for both models were obtained from the FE simulations and compared to the experimental results. In the first approximation, the first set of simulations was run with 3D model. The tube and the die set were modeled as 3D deformable and discrete rigid models respectively. 3D models can capture anisotropy

of material if it exists. 3D models can also predict strain localization and other instabilities of the material. Since in the present work, variation in strain along the hoop direction was not of primary concern, most of the simulations utilized only the axisymmetric models to decrease simulation time and to increase efficiency of the model (Fig 6.1). Therefore, simplifications were made and FE model does not account for the anisotropy of material. A comparison of 3D and 2D axisymmetric model results, as well as several other comparisons utilized in this set of simulations are presented in section 6.1.

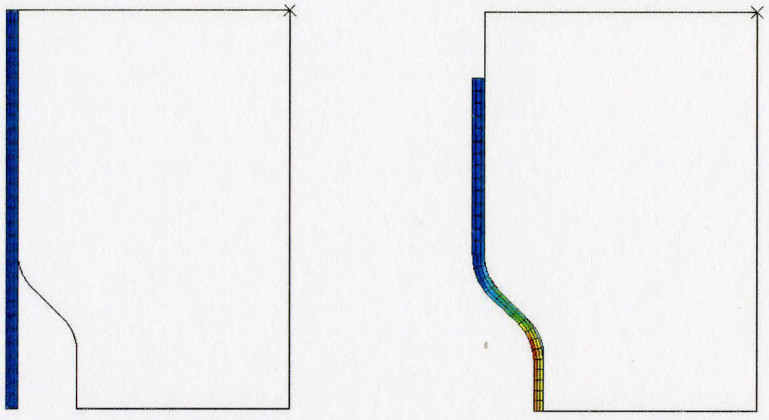

(a) 2D Axisymmetric Model Before Deformation

(b) 2D Axisymmetric Model After Deformation

Figure 6.1: 2D axisymmetric model before and after deformation

Set of simulations with 2D axisymmetric model showed very similar response to the response of 3D simulation set. An example of model type comparison is presented in section 6.1.2. Comparisons of tube wall thickness distribution of 2D axisymmetric model are presented in the following sections 6.1.1, 6.1.3, 6.1.4, 6.1.5. These simulations predict the material flow from initial tube configuration to the final tube configuration as shown in Figure 6.1.

6.1 Parametric Studies

Prior to experiment simulations, material model evaluation was performed. Material tensile data was fitted to Ogden hyperelastic model with N=3 order of strain energy potential. The material showed stable response for the rising part of stress-strain curve. Experimental stress-strain data curve with fitted Ogden material model curve is represented in Figure 6.2.

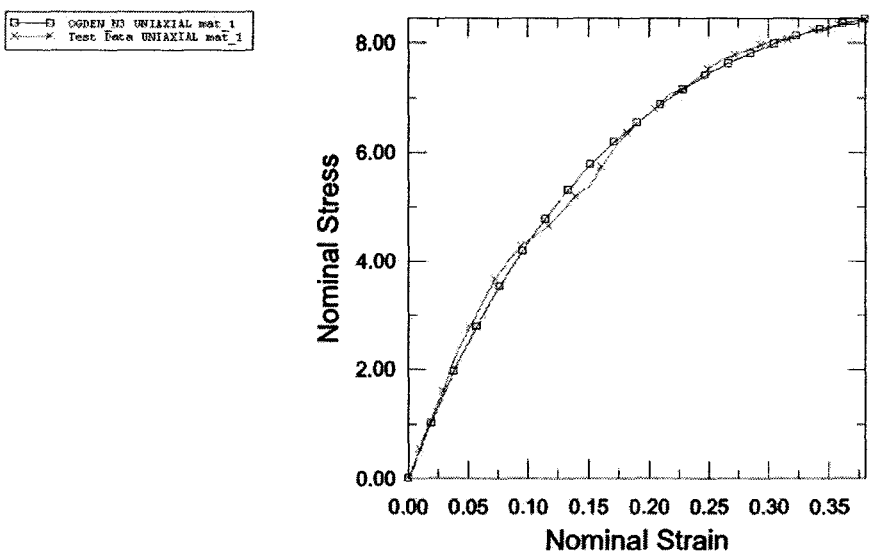

Figure 6.2: Experimental and fitted Ogden material model curves at 100°C

Fitted Ogden material model curve describes very close the experimental test data up to the nominal strain of 0.38.

To obtain AHM model coefficients, experimental test data was calibrated also for AHM material model. Due to the scope of the work to investigate the material formability at constant temperature of 100°C, only tensile stress-strain data for a constant temperature 100°C was selected. Material model curves were fitted to the tensile true stress-strain data with different strain rates. Description of obtained AHM material

model coefficients is presented in Appendix C2. Constitutive equations describing AHM were shown earlier in section 5.1.2. Fitted curves with the experimental test data are presented in Fig 6.3.

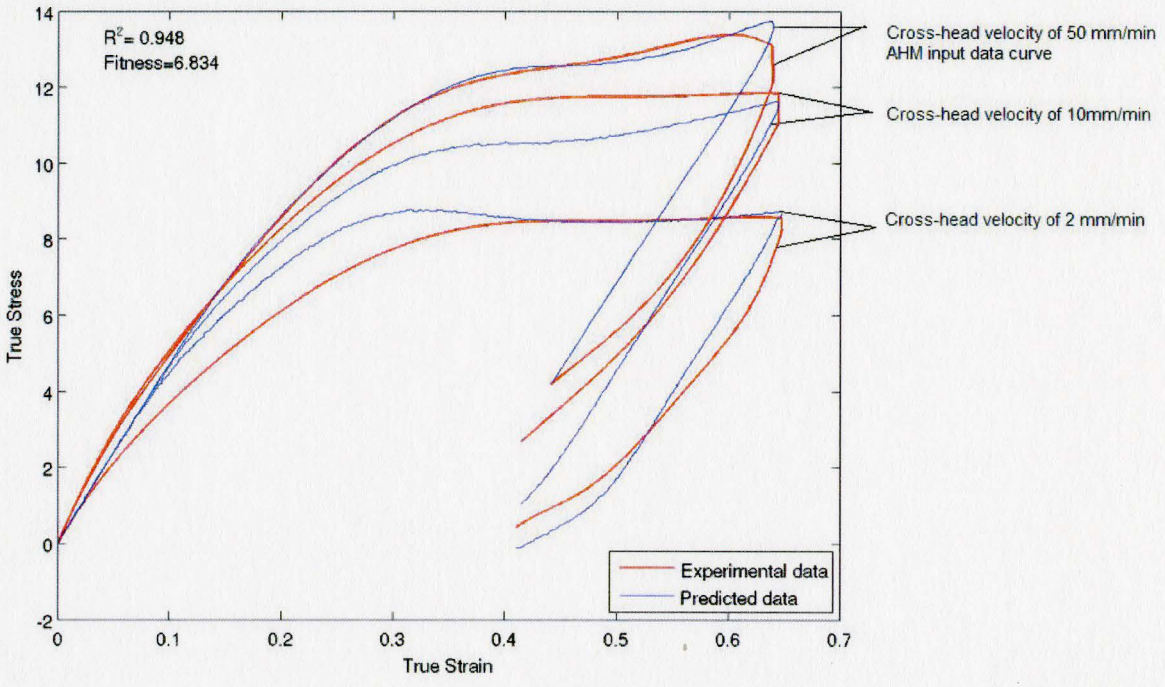

Figure 6.3: Experimental and fitted Ogden material model curves at 100°C

Material model fitted well the test data at 50 mm/min which was the actual strain rate of the experiment. Fitted curve is rather close to the experimental data up to a true strain value of 0.32, which corresponds to engineering strain value of 0.38. Model also has capability to predict unloading portion of the curve. Prediction of unloading does not follow very well the experimental curve due to the wide range of strain rates and insufficient amount of input data. However, that was not the main objective of this work and attention was mostly paid for the loading part of the curve. The results of unloading i.e, removal of the formed tube from the die, are presented in section 6.5.

6.1.1 Effect of Choice of FE Code Abaqus Explicit and Implicit on Material Response

Evaluation of chosen material models was first performed with a simple one element model simulation in Abaqus Explicit and Implicit Code. For this purpose, one element 3D model was created (Figure 6.4).

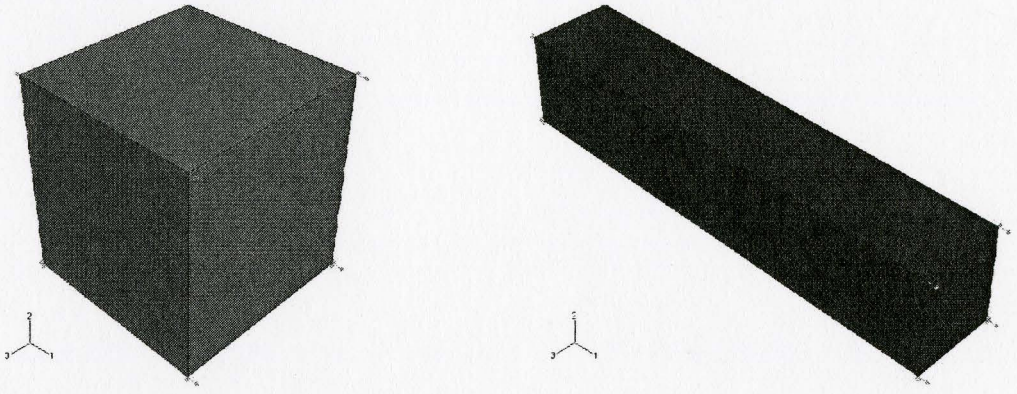

(a) Before deformation

(b) After deformation

Figure 6.4: One element FE model before and after deformation

One element was pulled with the same strain rate and at the same temperature as in the actual HGTF process. Experimentally obtained engineering stress-strain curve was used as an input data for the tensile test simulations. The output parameters were recorded after the process. Output true stress-strain curves were compared to the input true stress-strain data. The data curves match is almost identical, which demonstrates the accuracy of the model response prediction. However, all the later FE simulations cases was chosen to run in Abaqus/Explicit code. This code was the chosen, because it is able to better handle solution convergence problems that arise in multi body contacts, especially during forming operations involving dies. A

comparison of the input and output data for Ogden and AHM material models is shown in Figure 6.5.

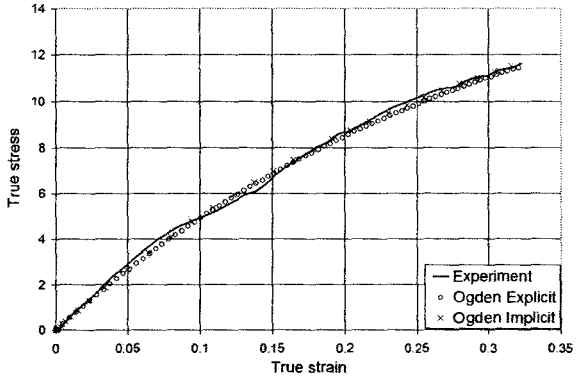

(a) Ogden Model

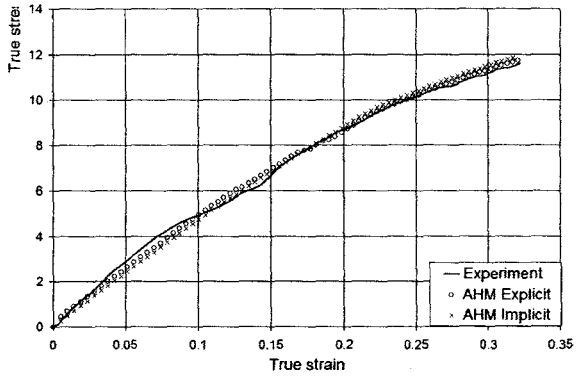

(b) AHM Model

Figure 6.5: Comparison of Explicit and Implicit codes for Ogden and AHM material models

6.1.2 Effect of Model Type on Thickness Distribution Results

For efficiency, it is better to run a 2D axisymmetric model. However, a 2D axisymmetric model does not account for the anisotropy of the material. A comparison of output results was made between 3D and 2D axisymmetric models as shown in Figure 6.6 using Ogden and AHM material models (Case 1). A comparison of thickness distribution showed that the difference between 3D and 2D axisymmetric model results was rather small, as it was initially expected from FE model simplifications that has been made, such as exclusion of material anisotropy effect. This small difference occured, perhaps, due to the different element formulation in these cases. Similar results were observed for the other cases. Therefore, to optimize the model running time with reasonable simplifications, all comparison cases were performed with 2D axisymmetric model.

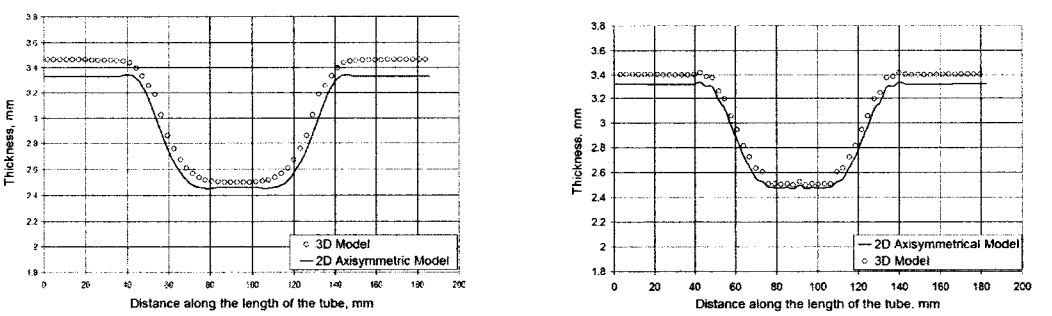

(a) Ogden Model

(b) AHM Model

Figure 6.6: Comparison of 3D and 2D Axisymmetric Ogden and AHM material models for Case 1

6.1.3 Effect of Element Size and Mesh Density on Thickness Distribution Results

The previous example demonstrated that it was more accurate and efficient to carry all of the simulations with 2D axisymmetric model. To test the accuracy of results, simulations were also conducted with a coarse and a fine mesh. The mesh refinement comparison was performed with Ogden material model. The tube was meshed with 30 and 90 elements along the length, while 3 elements were utilized in the thickness direction (Figure 6.7).

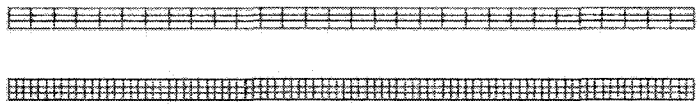

Figure 6.7: Mesh refinement in longitudinal direction

Another simulation was run for the same case with further mesh refinement in the thickness direction. The workpiece was meshed with 3 and 5 elements in thickness direction and 90 elements along the length of the tube. The FE model mesh is shown in Figure 6.8.

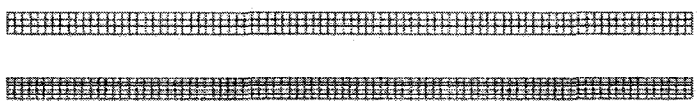

Figure 6.8: Mesh refinement in thickness direction

The comparison of the thickness distribution results for those three models is shown in Figure 6.9. With the mesh refinement, an improved thickness distribution compare to the experiment around the two end radii is noted. However, the thickness in the

expanded region in the middle of the formed tube remained unchanged.

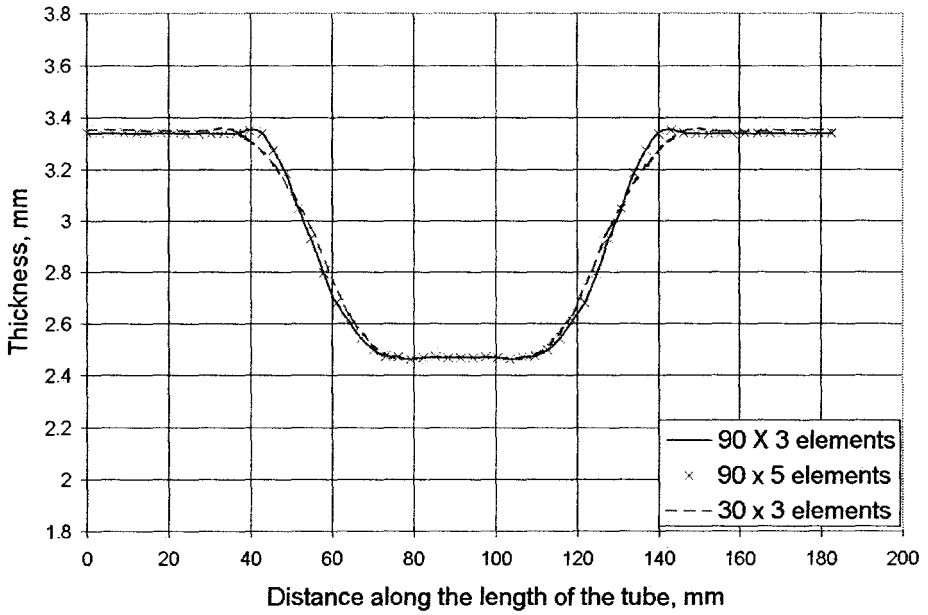

Figure 6.9: Results of mesh refinement in longitudinal direction (Ogden model, case 1)

Also, as evident from this graph, thickness distribution deviation between the models with 3 and 5 elements in thickness direction is negligible and simulations can be run faster with the same accuracy and with only 3 elements through the thickness of the tube.

6.1.4 Effect of Mass Scaling on Thickness Distribution Results

As mentioned earlier in Chapter 2, Abaqus Explicit FE code is based on explicit dynamic analysis of the deformed workpiece. Mass scaling is utilized to artificially decrease the run time. However, a penalty is paid due to inertial effects of mass scaling. Specifying mass scaling factor increases material density and decreases the simulation time. However, there are safe limits to mass scaling, where the simulations results are not affected. To identify the safe limits, simulation was run with no mass scaling factor and mass scaling factors of 2000 and 20000. Thickness curves were identical in case with no mass scaling factor and mass scaling factor of 2000. That showed that the sets can be run without affecting the output with mass scaling factor of 2000 (Figure 6.10(a)).

Another comparison was performed in Abaqus Explicit code with mass scaling of 2000 and 20000. As shown in Figure 6.10(b), increase of the mass scaling factor up to 20000 gave a small discrepancy between output results, particularly in the central part of test piece. That suggests that further increase in mass scaling will be out of the safe limits and affect the output results.

According to this comparison result, all previous simulations were run with mass scaling factor of 2000 which significantly decreased the run time of the simulations.

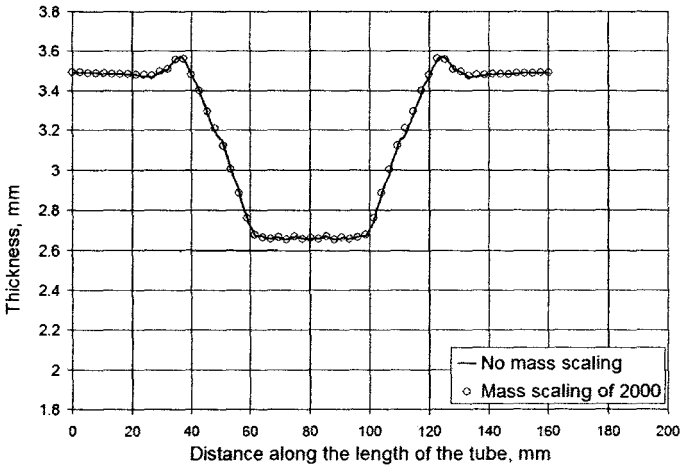

(a) No mass scaling vs. mass scaling factor of 2000

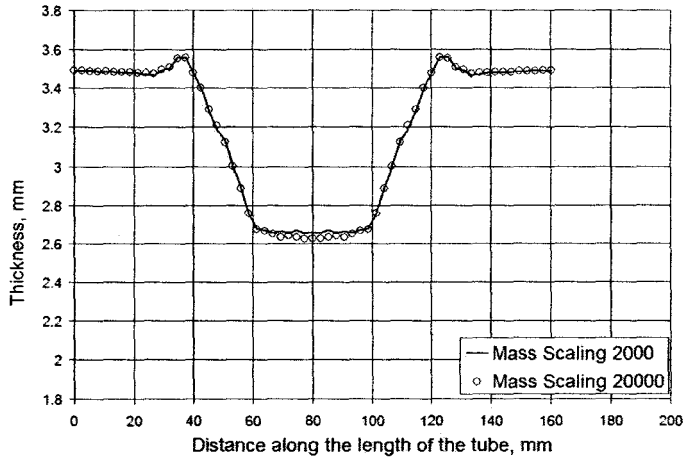

(b) Mass scaling factor of 2000 and 20000

Figure 6.10: Comparison of no mass scaling and mass scaling factors of 2000 and 20000

6.1.5 Effect of Coefficient of Friction on Thickness Distribution Results

Effect of friction coefficient on simulation results was investigated in this section. Fig 6.11 shows how tube wall thickness would be distributed if the value of friction coefficient would be increased to 0.1 (Case 4 and 6). As shown, the areas most affected by increase in friction coefficient are central part of the tube as well as the tube ends. An increased friction coefficient results in a reduced flow of material in

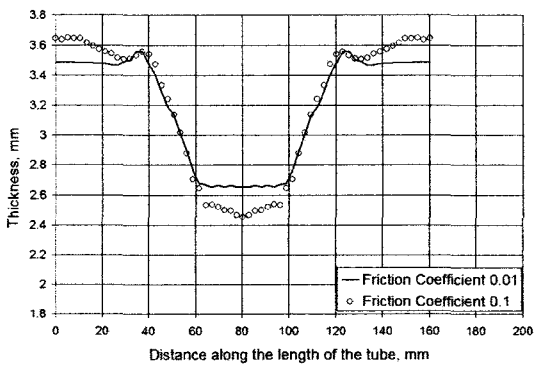

(a) Case 4

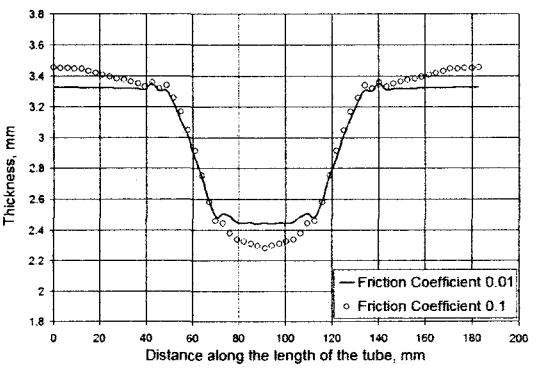

(b) Case 6

Figure 6.11: Comparison of coefficients of friction 0.1 and 0.01 for Case 4 and Case 6

the die cavity and consequently an increased thinning in the central region of the tube and an increased wall thickness non-uniformity. Although material is fed in die cavity with the same speed, less amount is actually distributed towards the centre of the tube due to the higher friction. This explain excessive thinning of the center of the tube and thickening of the tube ends at higher friction coefficients.

6.2 Evaluation of Numerical Simulations Results with Ogden Model

Evaluation of numerical simulation results with Ogden model is presented in this chapter. FE simulation time with this material model was approximately two hours for each case. Six cases were simulated from the initial tube to the fully loaded tube stage as shown in Figure 6.1. The process parameters for the different test cases were shown earlier in Table 4.1 in Chapter 4. Ogden material model parameters were explained earlier in Section 5.1.2 and material model coefficients are presented in Appendix C1.

6.2.1 Process Parameters vs. Thickness Distribution

As mentioned earlier in Chapter 5, all six experimental test cases were simulated with 2D axisymmetrical model. Simulations results, as presented in Figure 6.12, showed that experimental trends were captured rather well by the FE simulations. In particular, case 4 as well as case 3 illustrate an increase in wall thickness at the beginning of expanded tube wall area. This can be explained by excessive tube end displacement. In case 4, tube ends were fed by 29.21 mm from each side. Excessive tube end feed causes buckling and as a result thickening of the buckled portion of the tube wall. Case 5 showed thinning of expanded part of the tube wall. According to the experiment, this was a case of insufficient feeding, causing rapid thinning of the central part of the tube during the expansion process. Simulation results show that Ogden material model is able to capture the general deformation trends. A comparison of thickness distribution from Ogden material with that of AHM material and experiments is presented later in section 6.4.

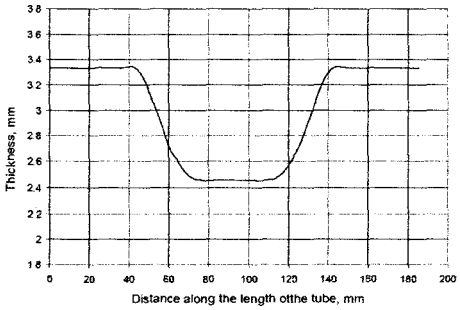

(a) Case 1 (Pressure 1.227 MPa, Feed 17.78 mm)

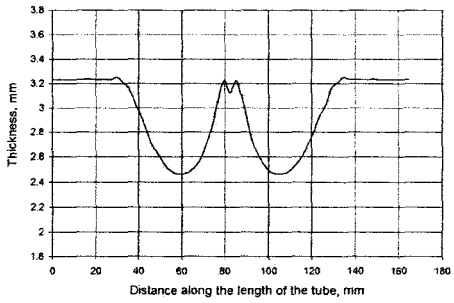

(b) Case 2 (Pressure 1.227 MPa, Feed 25.4 mm)

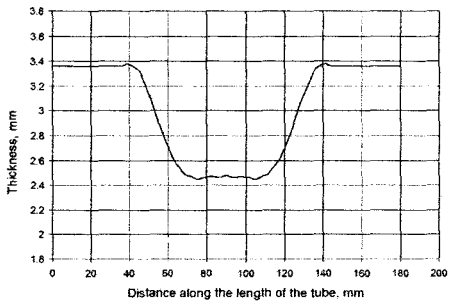

(c) Case 3 (Pressure 2.165 MPa, Feed 19.05 mm)

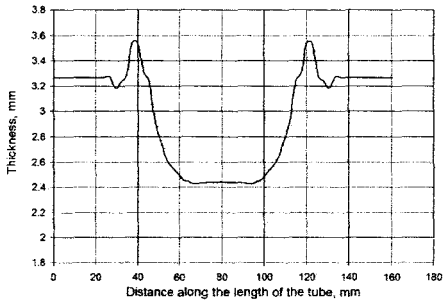

(d) Case 4 (Pressure 2.165 MPa, Feed 29.21 mm)

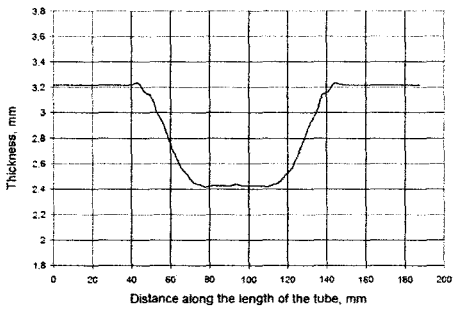

(e) Case 5 (Pressure 2.165 MPa, Feed 15.24 mm)

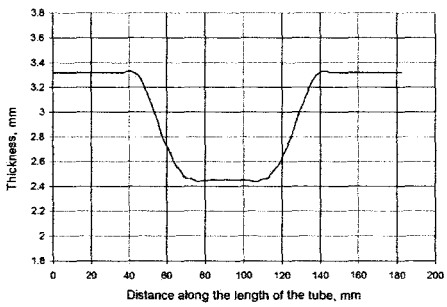

(f) Case 6 (Pressure 2.165 MPa, Feed 17.78 mm)

Figure 6.12: Tube wall thickness distribution results from 2D axisymmetric Ogden model

6.3 Evaluation of Numerical Simulations Results with Augmented Hybrid Model

Numerical simulation results for AHM material model are shown below. Six previous cases were simulated from the initial tube to the fully loaded tube stage as shown in Figure 6.1. The process parameters for the different test cases were shown earlier in Table 4.1 in Chapter 4. AHM material model parameters were explained earlier in Section 5.1.2 and material model coefficients are shown in Appendix ??. FE simulation time for AHM material model, due to complexity and large number of coefficients, was approximately three to four hours for each case, which is longer than FE simulation time with Ogden material model.

6.3.1 Process Parameters vs. Thickness Distribution

The same combination of process parameters as the Ogden model was applied to the AHM material model, as shown in Table 4.1. AHM model was also able to predict the general trends of the material deformation. Prediction of material thickening in cases 3 and 4, material thinning in case 5 and wrinkling thickness distribution instabilities in case 2 were all captured very well by AHM (Figure 6.13). A comparison of results from AHM and Ogden material model with experiments are presented later on in section 6.4.

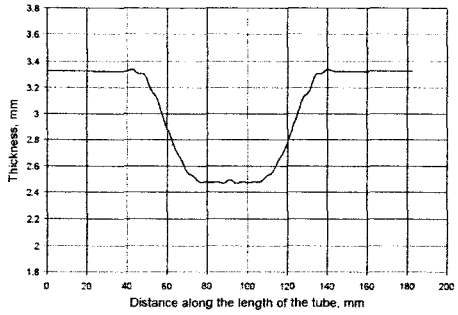

(a) Case 1 (Pressure 1.227 MPa, Feed 17.78 mm)

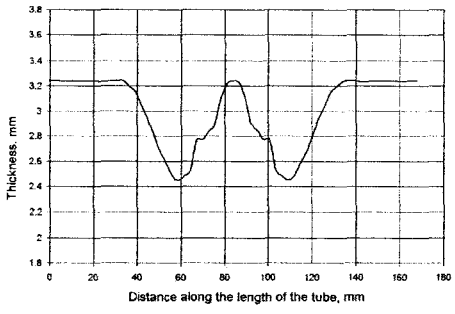

(b) Case 2 (Pressure 1.227 MPa, Feed 25.4 mm)

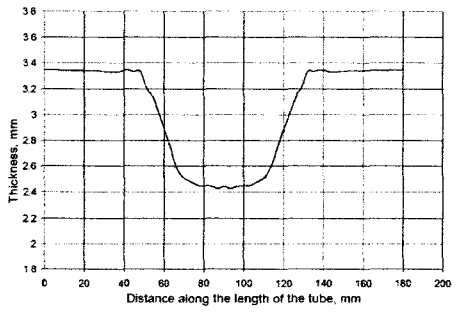

(c) Case 3 (Pressure 2.165 MPa, Feed 19.05 mm)

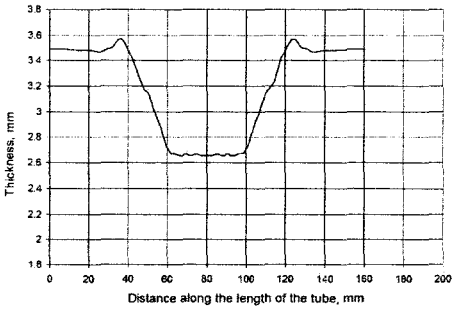

(d) Case 4 (Pressure 2.165 MPa, Feed 29.21 mm)

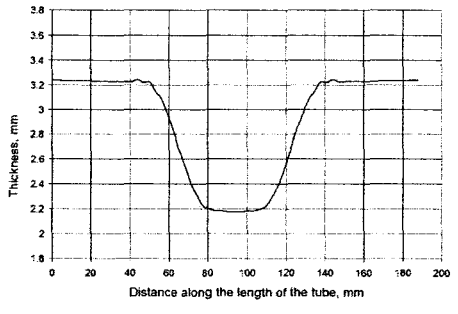

(e) Case 5 (Pressure 2.165 MPa, Feed 15.24 mm)

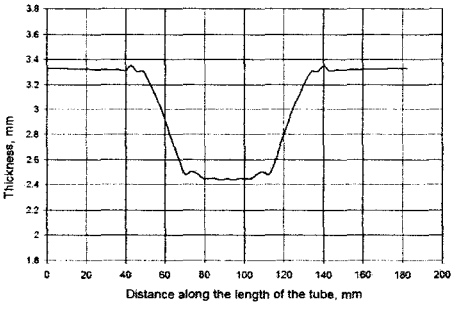

(f) Case 6 (Pressure 2.165 MPa, Feed 17.78 mm)

Figure 6.13: Tube wall thickness distribution results from 2D axisymmetric Augmented Hybrid model

6.3.2 Process Parameters vs. Major and Minor Strain Distribution

This subsection presents the results of major and minor strain distribution from 3D FE simulations for the AHM material model. Case 1 to 6 are described briefly and sequentially in Figures 6.14, 6.15, 6.16, 6.17, 6.18, 6.19 respectively. Ranges of values of major and minor strain distribution from FE simulation model are summarized in Table 6.1.

The tube piece is separated into three parts, symmetric center of the tube (AB), middle part (BC) and tube ends (CD) for comparison purpose. A range of major and minor strains obtained at these locations for the different test cases are shown in Table 6.1.

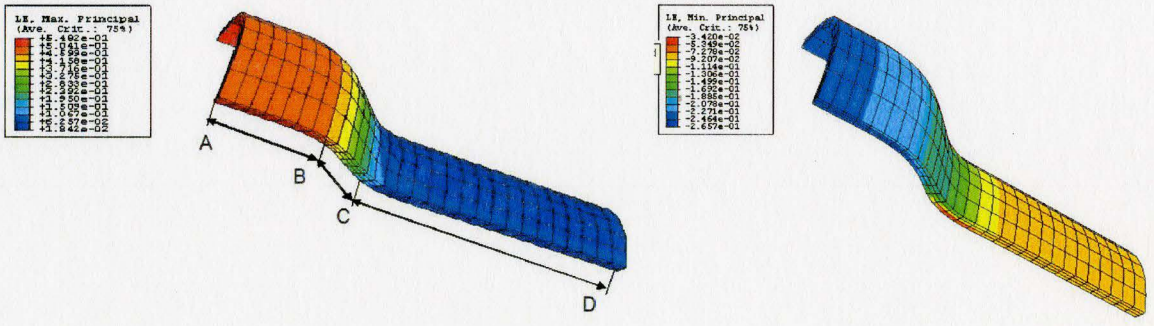

(a) Major strain distribution

(b) Minor strain distribution

Figure 6.14: FE simulation. Case 1 (pressure 1.227 MPa, feed 17.78 mm)

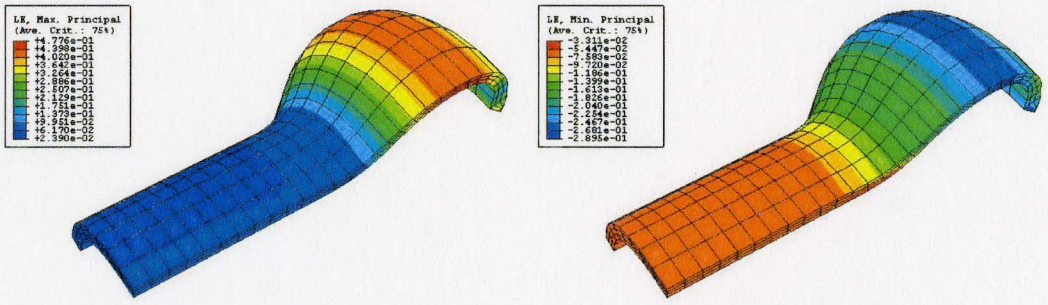

(a) Major strain distribution (b) Minor strain distribution

Figure 6.15: FE simulation. Case 2 (pressure 1.227 MPa, feed 25.4 mm)

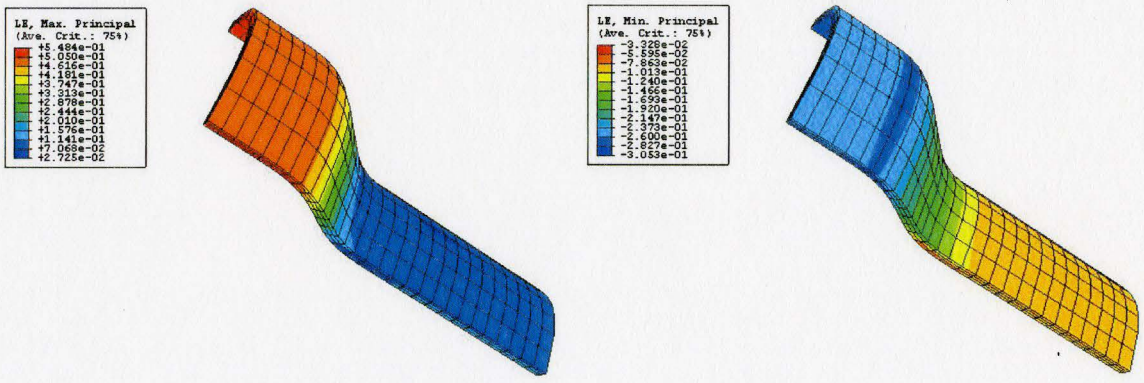

(a) Major strain distribution (b) Minor strain distribution

Figure 6.16: FE simulation. Case 3 (pressure 2.165 MPa, feed 19.05 mm)

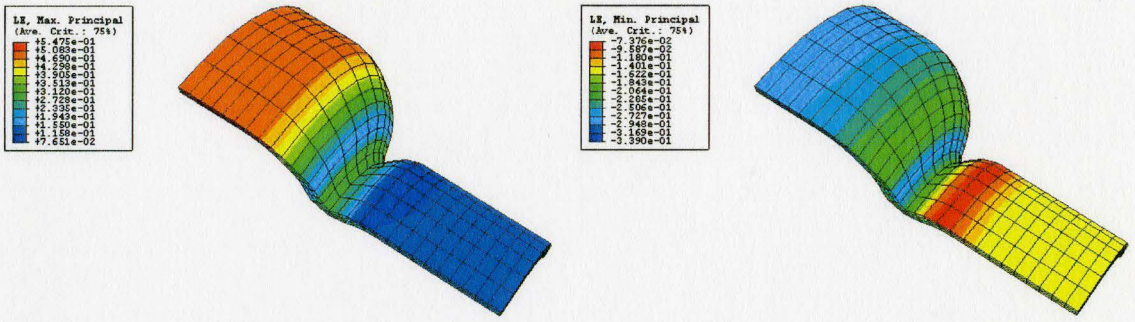

(a) Major strain distribution

(b) Minor strain distribution

Figure 6.17: FE simulation. Case 4 (pressure 2.165 MPa, feed 29.21 mm)

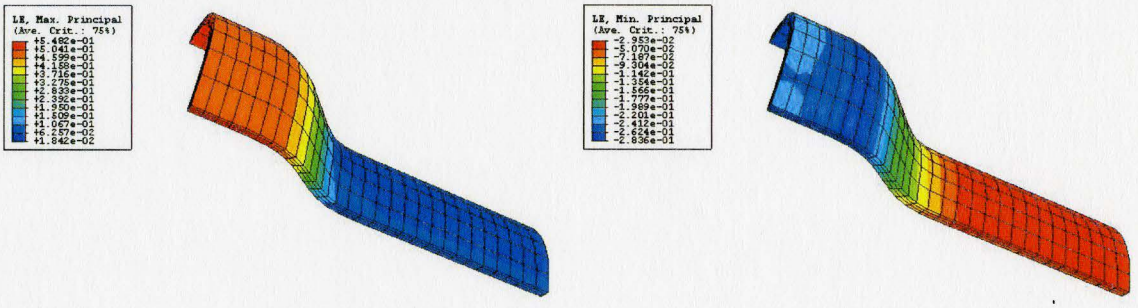

(a) Major strain distribution

(b) Minor strain distribution

Figure 6.18: FE simulation. Case 5 (pressure 2.165 MPa, feed 15.24 mm)

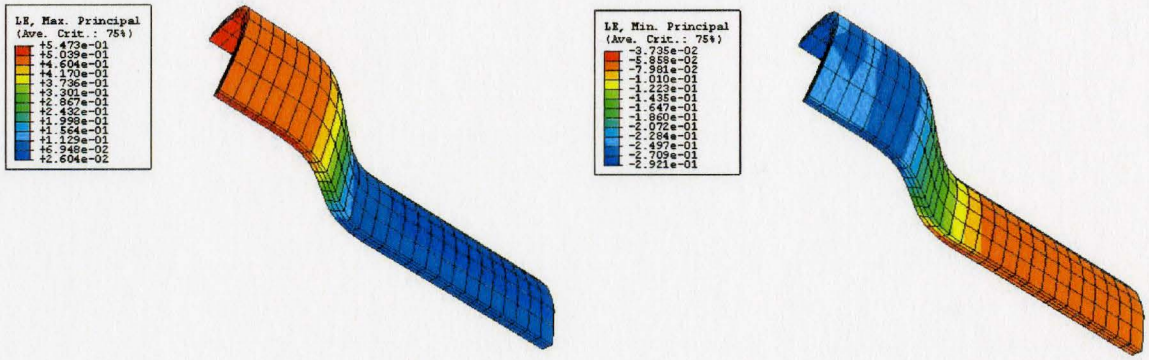

(a) Major strain distribution

(b) Minor strain distribution

Figure 6.19: FE simulation. Case 6 (pressure 2.165 MPa, feed 17.78 mm)

Case	Major Strain			Minor Strain		
	Center	Middle	Ends	Center	Middle	Ends
1	0.4	0.22-0.32	0.066	(-0.2)	(-0.18)-(-0.16)	(-0.092)
2	0.28-0.38	0.2-0.25	0.03-0.06	(-0.25)-(-0.15)	(-0.18)-(-0.13)	(-0.07)-(-0.04)
3	0.4-0.5	0.25-0.35	0.03-0.07	(-0.29)-(-0.26)	(-0.23)-(-0.21)	(-0.1)-(-0.08)
4	0.42-0.5	0.23-0.39	0.08-0.11	(-0.29)-(-0.25)	(-0.27)-(-0.2)	(-0.16)-(-0.12)
5	0.41-0.5	0.25-0.37	0.018-0.06	(-0.28)-(-0.22)	(-0.2)-(-0.13)	(-0.05)-(-0.029)
6	0.44-0.54	0.3-0.37	0.026-0.069	(-0.29)-(-0.24)	(-0.2)-(-0.14)	(-0.07)-(-0.05)

Table 6.1: Summary of major and minor strain distribution from six test cases

6.4 Comparison of Ogden and AHM Results with Experiments

In this section Ogden and AHM material model results are compared to experimental data. Comparisons are made in tube wall thickness over the entire tube profile and major and minor strain distribution over the expanded region of the tube. The experimental methodology and results were presented earlier in Chapters 3 and 4 respectively.

6.4.1 Thickness Distribution Comparison

In general for case 1, the overall tube wall thickness distribution shows an obvious thinning in the central part and thickening of the tube ends. The deviation between undeformed tube wall thickness of 3.175 mm and deformed tube varies along the length of the tube. In the central part, where experimental results show thinning, deviation between experimental results and undeformed tube wall thickness is approximately 0.4 mm. Deviation at the tube ends varies from 0.35 to 0.5 mm. Tube wall thickness approaches the initial value of 3.175 mm in the middle part, between the ends and the central part of the tube.

The shape of the formed tube was captured very closely by both, Ogden and AHM material models. In this case, although the shape of the tube did not show any failures, the amount of pressure applied in the tube forming process expansion was not enough to be able to reach the maximum tube diameter expansion. This result is shown in Figure 6.20.

The model shows very well the gap between the expanded tube at a fully loaded stage

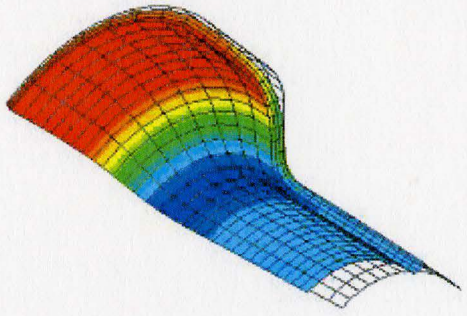

Figure 6.20: Case 1 (tube did not reach a full expansion)

and the die. Tube wall thickness distribution predicted by FE models and experiment deviates mostly in the central part and at the ends of the tube. However, the general trend of thickness distribution is predicted rather well by the models and especially the thinning of the central part of the tube. Deviation between FE model predictions and experiment at the central part of the tube is approximately 0.35 mm. Deviation between FE model results and experiment varies between 0.03 to 0.2 mm. Modeled thickness results at the ends of the tube show deviation of 0.15 to 0.25 from experimental measurements. Comparing between predictions of Ogden and AHM models, AHM model gives more accurate results in the expanded region.

In case 2, the amount of pressure was kept the same, but tube ends displacement increased resulting in wrinkling in both experiment and FE models. Abnormal thickness distribution in the experimental results verifies the presence of this kind of forming defect. Experimental deviation between deformed and undeformed tube wall thickness at wrinkles is approximately 0.2 mm up to the normal undeformed value. The ends and the central part of the tube show thickening of approximately 0.1 to 0.4 mm. FE models results show similar trend of thickness distribution. Deviation between tube wall thickness at wrinkles is quite large and is approximately 0.4 to 0.6 mm. Deviation in thickness at the center of the tube and tube ends varies from 0.15 to 0.35 mm. Between Ogden and AHM material model simulations difference

is negligible. Both of the models have about the same quality of prediction in this case.

Case 3 deals with the effect of process parameters resulting in buckling at the die corner radii. In this case, sufficient amount of pressure was applied but the tube ends received additional excessive feed into the die cavity. Displacement was increased in attempt to reduce thinning of the central part of the tube. However, at the particular constant speed of the process, material was not able to redistribute uniformly towards the center of the tube which accumulated an excessive material between the ends and expanded part of the tube resulting in tube wall thickening at the entrance to the die cavity for this case. However, tube did not have any visible deformation failures. Deviation from the uniform initial wall thickness and the tube wall thickness at the ends is approximately 0.2 to 0.3 mm. Deviation reached a maximum value of 0.55 mm at the tube ends. The central part of the tube had a lower deviation of 0.35 mm. In this case, as in case 1, AHM and Ogden showed similar results, however results of AHM material model provide a better wall thickness prediction at the expanded sides of the tube. Difference in wall thickness distribution between the models and experiments in the central part of the tube is approximately 0.3 mm. Difference in wall thickness at the ends of the tubes ranges between 0.1 to 0.3 mm.

The parameters of case 4 were based on the results of case 3. Further investigation of the effect of the value of axial displacement was conducted. Tube ends were pushed towards the center of the tube by 29.21 mm from both sides. Unlike the previous case, an excessive feed cause a visible buckling of the tube. However, the thickness of the central part improved and deviation approached its minimum value of 0.175 mm. Surprisingly, the sides points that indicated excessive thickening in the previous case did not show the same trend. This can be explained in terms of material movement towards the center in the beginning of the test resulting in more uniform central part thickness. At the same time, the excessive material left over at the thick-

ening points was pushed inside due to buckling which also showed as improvement at the tube ends. Material models prediction showed different results in this case. Although both models followed closely the general deformation trend, Ogden model showed a large deviation of approximately 0.6 mm from the experimental results in the central part of the tube. Prediction of AHM model is closer to the experimental results and difference in prediction is approximately 0.3 mm. At the tube ends, AHM model also showed better predictions than Ogden material model. Deviation between AHM model prediction and experimental curve at the tube ends is approximately 0.1 mm. Deviation between Ogden material model and experiments in the central part of the tube is 0.6 mm, while tube ends thickness prediction was underestimated by the Ogden model by approximately 0.15 mm.

Case 5 was conducted with a relatively small axial displacement to explore the effect of various process parameters and to introduce the possible excessive tube wall central part thinning. As it was expected, experimental deviation between the initial tube wall thickness and deformed tube wall thickness in the center of the tube reached its lowest value of 1.9 mm (Figure 6.21(e)). The ends of the tube did not experienced large deviation in thickness and differ from the initial thickness by 0.35 mm on each side. FE models were able to predict this experimental result rather closely. Although both material models described the thickness distribution very well, AHM material model was able to predict the thickness of the central part of the tube much better than the Ogden model. Difference between AHM prediction and experiments in the central part is only 0.28 mm, while Ogden model predictions deviate from the experiment for approximately 0.5 mm. Prediction of thickness distribution at the ends of the tube from both models is very similar and it deviates from the experimental by approximately 0.2 mm.

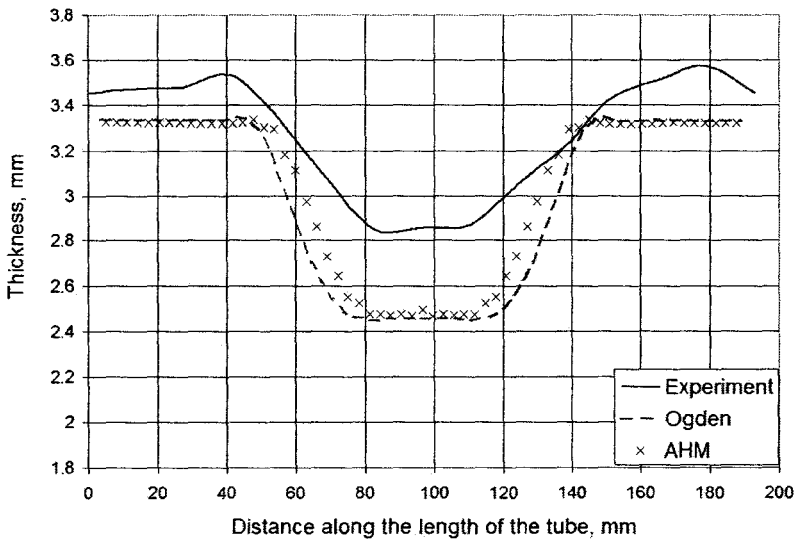

(a) Case 1 (pressure 1.227 MPa, feed 17.78 mm)

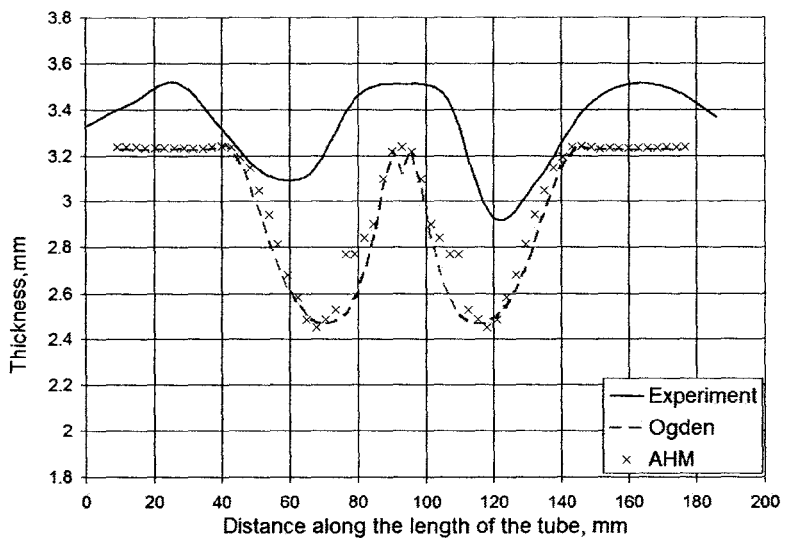

(b) Case 2 (pressure 1.227 MPa, feed 25.4 mm)

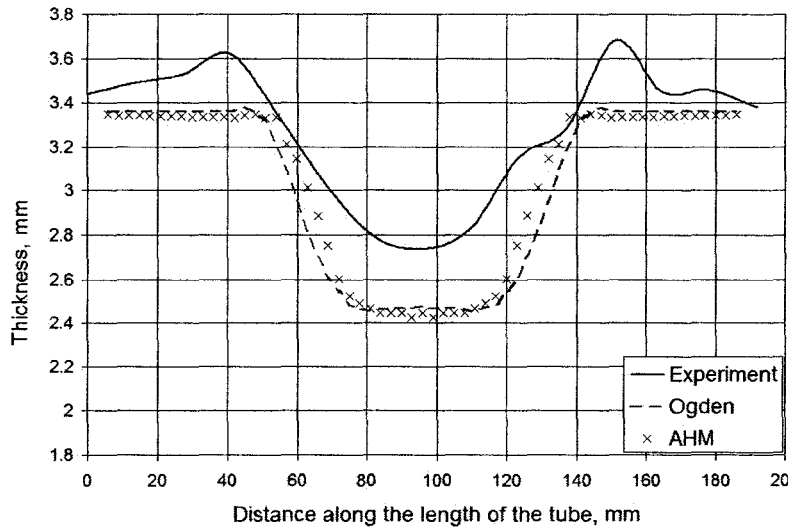

(c) Case 3 (pressure 2.165 MPa, feed 19.05 mm)

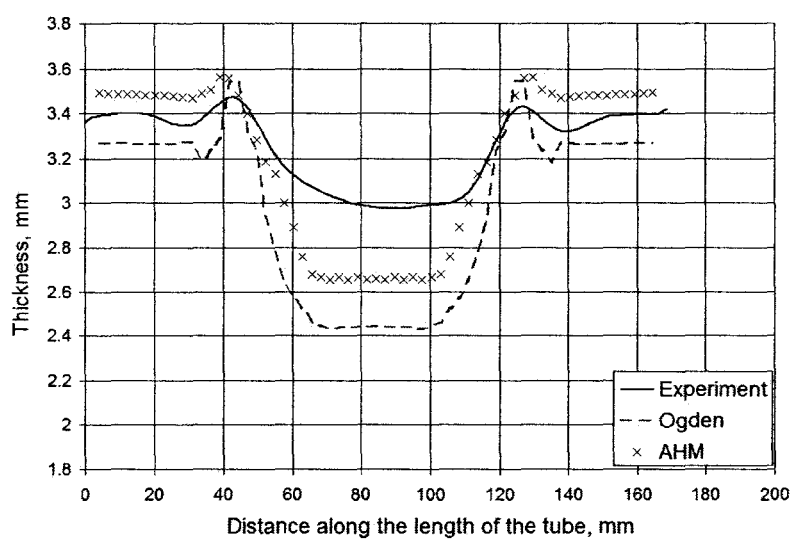

(d) Case 4 (pressure 2.165 MPa, feed 29.21 mm)

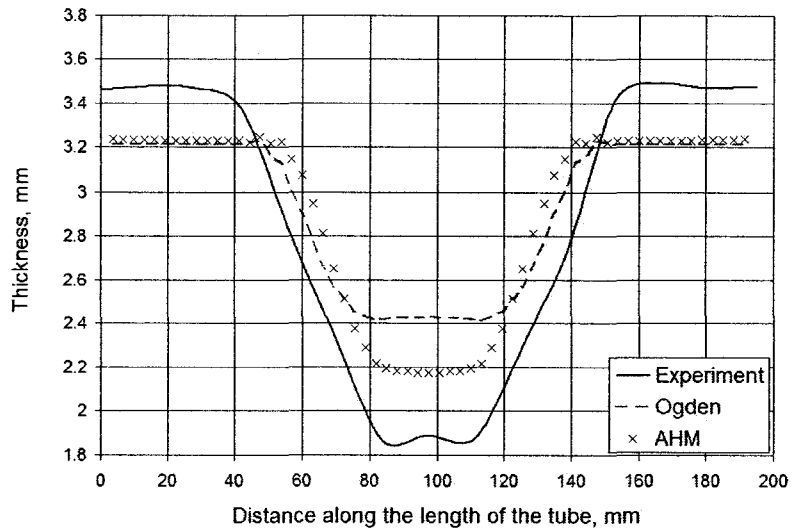

(e) Case 5 (pressure 2.165 MPa, feed 15.24 mm)

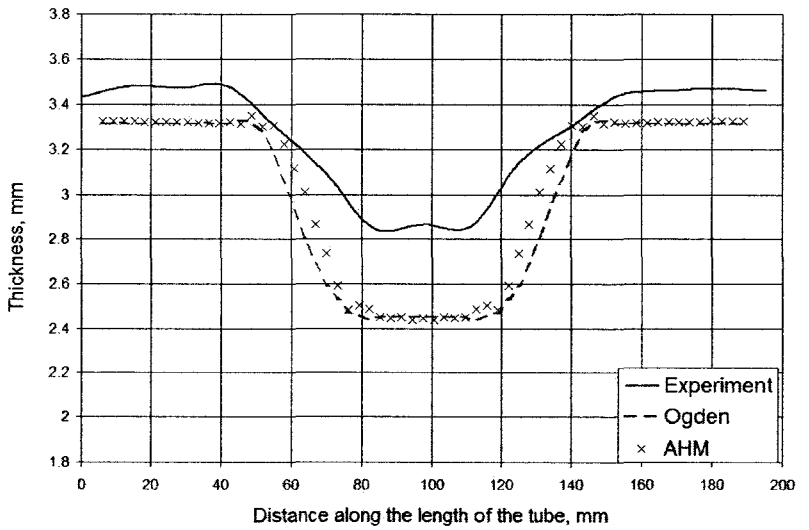

(f) Case 6 (pressure 2.165 MPa, feed 17.78 mm)

Figure 6.21: Tube wall thickness distribution comparison of Ogden, Augmented Hybrid model and experiments

Case 6, (Figure 6.21(f)), was designed to have an optimal process parameters based on the previous experiments. However, the speed of the process as well as temperature remained the same. The shape of the tube did not show any visible failures or imperfections. With the optimal process parameters, thickness distribution results approached the minimum possible deviation from the initial tube wall thickness for the same temperature and same process speed. Tube wall thickness distribution in the central part showed very promising results and approached very close the initial tube wall thickness with the difference approximately 0.3 mm. At the tube ends, experiment showed slight thickening with a deviation of 0.3 mm from initial thickness. Similar to the case 1 and case 3, AHM model better predicted the thickness distribution at the expanded sides of the tube with improvement of 0.1 mm from the Ogden model.

Tube wall thickness distribution comparison between experiment and FE models is summarized in the Table 6.2. All Thickness values are in mm.

	Experiment		Ogden		AHM	
Case	Center	Ends	Center	Ends	Center	Ends
1	2.84	3.5	2.48	3.33	2.47	3.325
2	3.5	3.44	3.18	3.24	3.22	3.24
3	2.76	3.5	2.44	3.285	2.43	3.28
4	2.99	3.4	2.43	3.27	2.67	3.5
5	1.9	3.47	2.42	3.23	2.17	3.27
6	2.87	3.32	2.42	4	2.44	3.32

Table 6.2: A comparison of thickness distribution between experiment and FE models

6.4.2 Major and Minor Strain Distribution Comparison

FE simulation results with 3D AHM models provide major and minor strain distribution over the tube surface and these values were compared with similar experimental data. Experimental measurements of major and minor strain distribution were performed with Argus optical strain measurement system and compared to the major and minor strain distribution received via FE simulation model. Due to the nature of experiments, only central expanded part of the tube was able to retain the applied grid pattern (Section 4.3). Therefore, major and minor strain distribution of FE material models and experiments were compared only at the expanded part of the tube. Furthermore, the area over the samples where the results are reported is different from case to case due to poor image quality and disappearance of grids in some regions. Also, strain distribution shows inhomogeneity of various degrees in different cases over the strain measured tube surface. This could be explained that 3D FE model predicts the same value of circumferential strain due to use of isotropic model. Effect of anisotropy is not incorporated in FE model. Also, the models do not account for microstructure induced inhomogeneity of the material.

For Case 1, major strain distribution over the expanded part of the tube in experiment is 0.3 - 0.4 and minor strain distribution is approximately -0.2 at most of the expanded area. However, it showed that a small area in the center experienced higher level of minor strain of 0.002. This phenomenon did not show in the simulation results due to the simplifications made in FE model. Uniform value of minor strain in simulation is approximately -0.2, which is the same as in experimental results obtained my optical strain measurement technique. Major strain is very close to the experimental value at 0.4 as well.

Wrinkling is observed in case 2 in terms of oscillations in tube wall thickness along

the length of the tube. Experimental results at wrinkles show the major strain distribution at 0.3 - 0.4. Simulation results show very similar value of approximately 0.4. Central unexpanded part of the tube show major strain distribution at approximately 0.1 which is very close to that of the experiment of 0.15. Minor strain distribution at wrinkles in experiment -0.1, while simulation model shows a slightly larger value of -0.2. In the central part of the tube, experiment show minor strain of -0.05 while the simulations show a minor strain of -0.1.

Major strain distribution in case 3 shows unusual pattern in a way of very inhomogeneous major strain distribution with a strain value ranging from 0.33 to 0.45. This phenomenon shows effect of inhomogeneous microstructure of the tested material. Simulations indicate major strain in a range of 0.45 to 0.5 over the measured area. Minor strain in experiments varies from -0.2 to -0.15 and in FE simulation results is approximately -0.25. Overall, the models slightly overestimate major and minor strain values.

Experimental major strain distribution in case 4 ranges from 0.3 to 0.35, while simulation major strain distribution measurements show a value of approximately 0.46. Minor strain in experimental case ranges from -0.2 to -0.1 and minor strain indicated by FE simulation model is approximately -0.29. In this case, as measurements show, both values of major and minor strain are slightly overestimated.

In case 5, major strain distribution from experiment varies from 0.3 to 0.42 with the average value of 0.35 in most of the measured tube surface area. FE simulation model show the major strain distribution in the range 0.45 - 0.5 indicative of a higher level of hoop loading of the tube compare to the experiment. Minor strain distribution in experiment is approximately -0.23 in most of the area. FE simulations results of minor strain distribution are at value of -0.22, which is in a good agreement with

the experimental results.

In case 6, major strain distribution from the experiment exhibits a wide range from 0.25 to 0.5. FE simulation model shows a value of major strain of 0.5. Thus, the values of major strain distribution in both cases are in the same range and show good agreement. Minor strain distribution in experiment varies from -0.17 to -0.09, while FE simulation results show a value approximately of -0.22, which indicates slight difference between measurements.

A summary of major and minor strain distribution comparison between experiment and FE model is presented in Table 6.3.

Case	Major Strain			
	Center		Middle	
	Exp	FE Sim	Exp	FE Sim
1	0.27-0.33	0.22-0.32	0.32-0.4	0.066
2	0.3-0.35	0.28-0.38	0.35-0.4	0.2-0.25
3	0.33-0.44	0.4-0.5	0.38-0.45	0.25-0.35
4	0.3-0.33	0.42-0.5	0.3-0.35	0.23-0.39
5	0.35-0.42	0.41-0.5	0.3-0.38	0.25-0.37
6	0.25-0.5	0.44-0.54	0.3-0.5	0.3-0.37
Case	Minor Strain			
	Center		Middle	
	Exp	FE Sim	Exp	FE Sim
1	(-0.2)	(-0.2)	(-0.2)	(-0.18)-(-0.16)
2	(-0.05)	(-0.25)-(-0.15)	(-0.15)	(-0.07)-(-0.04)
3	(-0.13)-(-0.15)	(-0.29)-(-0.26)	(-0.14)-(-0.18)	(-0.23)-(-0.21)
4	(-0.2)-(0.16)	(-0.29)-(-0.25	(-0.14)-(-0.2)	(-0.27)-(-0.2)
5	(-0.2)-(-0.23)	(-0.28)-(-0.22)	(-018)-(-0.22)	(-0.2)-(-0.13)
6	(-0.17-(-0.09)	(-0.29)-(-0.24)	(-0.17-(-0.09)	(-0.2)-(-0.14)

Table 6.3: A comparison of major and minor strain distribution between experiments and FE simulations via AHM material model

6.5 Effect of Unloading on Thickness Distribution Results

Effect of unloading was studied with AHM material model. Fully loaded and unloaded tube is presented in Figure 6.22 for case 3. Results show that thickness distribution after unloading is more uniform compared to fully loaded stage. The overall deviation in thickness distribution after unloading between center of the tube and tube ends is approximately 0.6 mm. Meanwhile, this deviation approach 1.0 mm in fully loaded stage. This indicates that material is able to redistribute during the unloading stage.

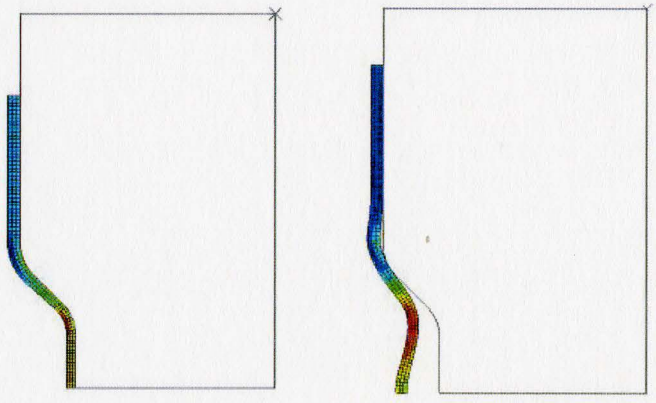

(a) Fully loaded (b) Unloaded

Figure 6.22: Tube profile at a fully loaded stage and after unloading for Case 3

Another effect is captured by the full length of the tube. In the fully loaded stage the tube length is 180 mm compared to the 192 mm length in experiment. Unloading results show the tube full length at 184 mm.

The difference of 4 mm demonstrate the effect of unloading or springback during the

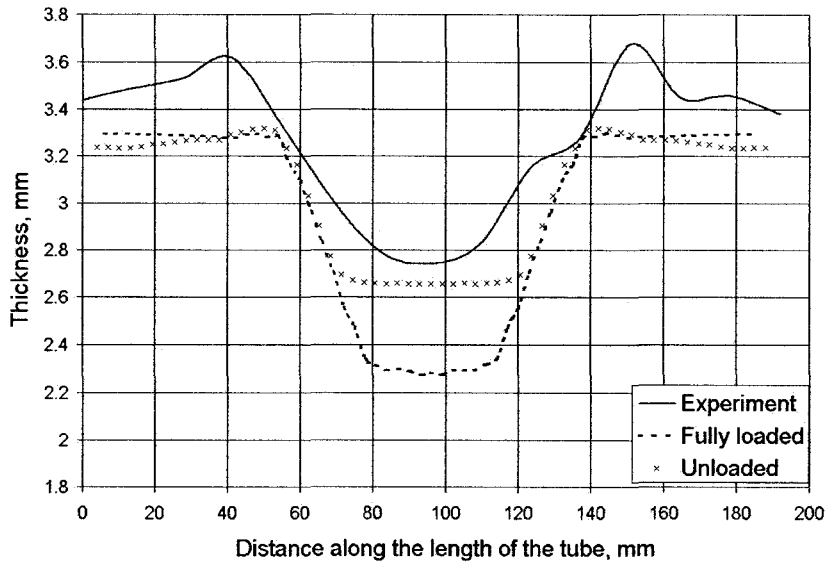

Figure 6.23: Thickness distribution comparison with unloading (Case 3)

unloading part of the tube forming process. Nonetheless, the thickness distribution in unloading stage was improved, the tube was not able to retain the appropriate shape, which is shown by springback effect in the central part. This analysis shows that unloading should be modeled to accurately predict the final part length, thickness distribution and other geometric characteristics of the part.

Chapter 7

Discussion

Process parameters play a major role in the quality of the final shape of the tube. Application of high internal pressure and insufficient tube ends feeding causes the tube wall thinning. Excessive thinning is observed in the center portion of the tube, while the tube ends experience slightly thickening. Thickness non-uniformity has an effect on product in-service performance. Simulations results of tube wall thickness distribution from Ogden and AHM material models respectively were presented earlier in sections 6.2 and 6.3. In summary, both, Ogden and AHM material models give acceptable results for HGTF process. Results are close to experimental and show the tube shape and general trends of tube wall thickness and major and minor strain distribution. AHM, as well as Ogden model, were able to capture very closely tube wall thickening in excessive end feed case 4. Models also predicted very well tube thinning with insufficient end feed in case 5. Simulations results also exhibited tube wrinkling failure in case 2 with low pressure and excessive tube end displacement. Case 1 showed insufficient expansion due to low pressure.

In a comparison of results from 3D and 2D axisymmetric models, 3D model gives slightly better results of tube wall thickness distribution. In FE modeling, by defini-

tion, 3D models use brick elements and 2D axisymmetric models use solid elements. FE models element type could be a contributing factor in the discrepancy observed. Although the discrepancy is rather small, more accurate results would be obtained with 3D model.

Further, majority of the simulations were performed only up to the loaded stage of the formed component. Unloading stage was not incorporated. As a result, the model result does not account for the possible material springback. Nevertheless, it was not of high importance for the conventional plastic forming processes. High temperature polymer forming processes typically involve rapid cooling of the die at end of the forming stage to retain the part shape, without having undesirable effects, such as shrinking or springback. In simulating HGTF at high temperatures, both unloading and cooling part of the process should be incorporated. More advanced viscoelastic- viscoplastic models that incorporate both unloading and cooling capabilities will need to be employed to fully simulate the experimental method to achieve better agreement with the experimental results.

Friction coefficient is another factor that could have contributed to the discrepancies between the experimental and simulation results. The value of friction coefficient, as noted in [14] and [13] depends on tube material (metal, aluminum, plastic), die surface (surface finish, hardness and surface treatment, coating) and various types of lubricant utilized. Friction coefficient used in this work was taken from the literature and represent the general approximation of the real coefficient. Meanwhile, the material parameters of the polymeric materials and output results are heavily depend on the process temperature. Variation of the temperature can give discrepancies observed in section 6.1.5.

Proper mesh has to be applied on the tube piece in FE simulation of tube form-

ing process. Coarse mesh can decrease simulation time. However, it will lead to mesh distortion during forming step and modify significantly thickness distribution results. The change is more severe at the critical points of the tube where the coarse mesh does not allow the material to fill out the small radii of the deformed shape. Comparison of slightly coarse mesh and refined mesh were presented earlier in Section 6.1.3. As shown in Figure 6.9, the results are more accurate with the refined mesh and tube was able to fill out small radii of the deformed tube shape better, than with the slightly coarse mesh.

Material models can be further improved to give a better explanation of material behavior. In case of Ogden material model, input parameters were introduced by experimental engineering tensile stress-strain curve. Model fit gave a very close explanation of material behavior up to strain value of 0.38. Attempt to fit Ogden material model to higher strains, gave an instability effect due to unstable nature of experimental data. AHM material model also showed very close fit up to the same value of strain. In addition, the model incorporated viscoelastic-viscoplastic material description capabilities. However, for the material model calibration only experimental tensile stress-strain curve was used, though for the best prediction of material response, compression and punch tests should have been incorporated. Additional experiments could give more detailed explanation of material behavior under different combination of applied stresses. Temperature limits could also been narrowed down. Narrowing down temperature and strain rate windows would give AHM smaller forming data limits window, which increase the efficiency and model calibration results. It leads to more accurate parameters obtained and better material response prediction.

Material microstructure can also be incorporated in material model definition. Simplifications made for material anisotropy and microstructure in the present simulations accounted for discrepancy between the experimental and FE major and minor

strain distribution results. FE model does not show strain localizations and inhomogeneous strain pattern distribution captured by Argus optical system. Integration of microstructure properties of material in the FE simulation model can give more accurate results and better prediction of material behavior.

For the experimental part, there have been several limitations. HGTF process incorporates a closed die during the process. Therefore, part strain measurements could be carried out only at the end of the process when the die is open. Inability to do continuous measurements and record tube wall thickness at fully loaded stage, gave discrepancy in results between FE models and experiments. To improve the process performance and to better understand the various factors affecting the final quality of the tube piece in a time based scale, different process improvements could be incorporated. This limitation could be overcome with a transparent die. The process would be easily observed at different forming stages and an on-line optical strain measurement system could be incorporated for the continuous strain measurements during the forming process. It would give the ability to obtain strain measurement results through the transparent die at any forming stage and compare these experimental results with the results obtained from FE model at different time steps.

Sample preparation before the experiment play also an important role. Tube ends should be carefully cut and machined. Any imperfection at tube ends edges will result in a loose contact between the tube ends and side actuators plugs. In a turn, it will lead to gas pressure drop, which consequently contribute to inaccurate pressure readings and as a result to a poor final quality part. Utilization of gas intensifier in this case in place of a gas pressure system, would add control capabilities during the tube pressurization forming step.

Use of lubricant would be another factor to consider. Use of different types of lubri-

cant can ease material flow into the die cavity during forming. It enables material to flow faster towards the center once pressure is applied. Tube wall thickness distribution in this case will have more uniformity which improve the final tube quality.

As it was discussed earlier in Chapter 3, cooling rate contributes significantly to the final shape and tube wall thickness distribution. Increasing the cooling rate will help to retain the formed tube shape after unloading and cooling as close as possible to the fully expanded shape in a fully loaded stage without any undesirable effect such as shrinkage. This can be achieved by adding extra cooling channels throughout the die and as close as possible to the tube surface. Improved capabilities of chiller can also speed up the cooling process.

Another factor is a process temperature. In FE models was assumed that process is conducted at a constant temperature and final tube wall thickness distribution is a tube thickness at a loaded stage and at elevated temperature. However, in a real process, the temperature is not uniform and final part pass through a cooling stage before measurements are made. The same applies to major and minor strain distribution. These factors can contribute to discrepancy between FE simulation and experimental measurements. In this case, more accurate process control would be recommended, as well as ability to incorporate cooling stage in FE model parameters.

As it was presented earlier in Section 6.4.2, major and minor strain distribution were obtained in the formed part surface via FE model and validated by experiment via optical strain measurement system. As it was discussed, grid retention is one of the major problems that lead to the poor image quality. Although the tube before deformation was covered with tape to protect grid pattern, friction and other environmental parameters such as high temperature, made impossible to retain the full tube length grid pattern. It disappeared completely at the ends of the tube and

remained mostly in the central part of the tube, where the friction was significantly lower. This can be considered for the future similar experiments in terms of finding a way to retain a grid pattern on the tube surface. It can be done by careful selection of the applied ink or material to cover the tube piece before deformation. Another technique or material, instead of ink, can be considered to apply for grid retention. Tape cover in this case is one of the factors that might affect the final results. However, the difference between plastic tape and tube behavior in contact with the die was assumed to be negligible and was simplified in FE simulation models.

Nonetheless, Ogden and AHM models gave very good results for PP HGTF process. Ogden model has been intensively employed for the plastic forming process simulation in the past. It describes very well material behavior, though it does not have the ability to describe unloading part of the process. Taking it into consideration, more advanced AHM material model was used in attempt to incorporate the significant changes on tube wall thickness distribution during the unloading stage.

AHM material model is more advanced and has capability of describing unloading part of material response. Although it showed tube shape change after unloading, it still gives a positive feedback in terms of ability to observe the final result changes. Final results can be improved by further exploring AHM model capabilities and by incorporating more coefficients in material model description.

Finally, it is to be noted, that present work involves a close comparison of results from experiment and FE simulations. While this is useful, once a valid FE model is developed, the real value of the modeling activity lies in optimizing the HGTF process by carrying out a large number of FE simulations outside of the range of experimental test conditions. This way, the model can capture most of the possible variations of process parameters and conditions without involving costly experimental part. The

consequent application of data analysis and different optimization techniques, such as sequential quadratic programming or model inversion, may lead to better part shape and mechanical properties with minimum effort. Various optimization techniques have been employed for establishing an optimal forming window for polymer process parameters and conditions. As it was mentioned earlier in literature review, sequential quadratic programming was used in [51], to optimize the loading path and minimize the tube thickness variation. Similar work has been done by this author in [52], where single set of process operating variables and conditions, such as internal pressure, axial displacement, load path, temperature and strain rate was established. Data received from the batches was analyzed by implementation of multivariate statistical data analysis, such as principal component analysis and projection to latent structures. Optimized variable trajectories and operating conditions yielded into desired quality characteristics in terms of tube wall thickness uniformity. In that case, 25 different batches with different process variables and conditions were analyzed. For better results, larger number of batches could be included as well as more components could be incorporated in data analysis. Another improvement would be the inclusion of additional process information as a variable or constraint, such as initial states of thickness, stress and strain in the tubular material produced in the previous stages. Also, final tube shape can be included as constraint in optimization algorithm, as a way of minimization of distance between the outer tube wall and the inner surface of the die.

Chapter 8

Conclusions and Recommendations

8.1 Conclusions

The present work conclusions are summarized with the following points:

1. Axial-feed hot gas tube forming (HGTF) process developed at McMaster, has been experimentally and numerically analyzed. Various characteristics of the process have been reported.

2. FE models were able to capture material failure such as wrinkling and buckling and also predicted a case of incomplete tube expansion due to the low pressure and tube buckling initiation.

3. Tube wall thickness distribution obtained via Ogden and AHM material models followed closely the experimental trends.

4. Augmented Hybrid model, a viscoelastic-viscoplastic model, has been used for the first time in finite element simulation of plastic tube forming. AHM model gave better prediction of the overall tube wall thickness distribution than Og-

den material model in a fully loaded stage. Major and minor strain distribution results with AHM in a fully loaded stage are in a good agreement with experimental results.

5. Unloading part of HGTF was incorporated for the first time in FE simulation with AHM in an attempt to describe the final tube forming process results. Unloading results with AHM show improvement in tube wall thickness distribution as well as captured full tube length recovery.

8.2 Recommendations

Presently, forming process modeling capabilities of plastics are limited because of the lack of accurate constitutive material models with abilities to predict plastic behavior at high temperatures and high strain rates in loading and unloading stages. Increasing use of advanced viscoelastic-viscoplastic models will allow to modelers predict material behavior with higher degree of accuracy in FE simulations of plastic forming processes.

The following approach is recommended to further improve FE simulation results of HGTF.

1. To incorporate compression and dome test data along with tensile stress-strain data into material model calibration

2. To increase number of experimentally measured coefficients in AHM material model, which will result in more accurate material behavior prediction

3. To incorporate anisotropy in material model definition which will give better ability to capture strain distribution in the hoop direction of the tube

4. To include aspects of material microstructure in the material models

5. To perform design of experiment and narrow down the temperature and strain rate limits window of testing material to approach the real process environment

6. To perform multivariate statistical data analysis on the data in conjunction with an optimization method to obtain optimal process parameters

List of References

[1] The McGraw-Hill Companies Inc. *Business Week.* `http://yahoo.businessweek.com/technology/content/sep2003/tc2003094_1278_tc127.htm`.

[2] James L. Throne. *Understanding Thermoforming.* Hanser Publishers, Munich Vienna New York, 1999.

[3] R. E. Christensen. Thermoforming Behavior of Polypropylene. *American Society of Mechanical Engineers*, 37:256–259, 1979.

[4] G. Frolich. Twin-sheet and high pressure thermoforming. *Kunststoffe Plast Europe*, 87:16–17, 1997.

[5] M. Tabrizi. Twin sheet thermoforming using "TAB" technique. *Annual Technical Conference - ANTEC*, 1:706–709, 1998.

[6] Z. Tadmor and C. G. Gogos. *Principles of Polymer Processing.* John Willey & Sons, New York, 1979.

[7] Design inSite. *The designer's guild to manufacturing.* `http://designinsite.dk/htmsider/pb2001.htm`.

[8] Donald V. Rosato and Dominick V. Rosato. *Blow Molding Handbook.* Hanser Publishers, Munich Vienna New York, 1989.

[9] K. Tahboub and I. Rawabdeh. A design of experiments approach for optimizing an extrusion blow molding process. *Journal of Quality in Maintenance Engineering*, 10:47–54, 2004.

[10] Engineer's handbook. *Manufacturing: Plastic Molding and Forming.* `http://www.engineershandbook.com/MfgMethods/blowmolding.htm`.

[11] L. H. Lang, Z. R. Wang, D. C. Kang, S. J. Yuan, S. H. Zhang, J. Danckert, and K. B. Nielsen. Hydroforming highlights: Sheet hydroforming and tube hydroforming. *Journal of Materials Processing Technology*, 151:165–177, 2004.

[12] M. Kos and T. Altan. An overall review of the tube hydroforming (THF) technology. *Journal of Materials Processing Technology*, 108:384–393, 2001.

[13] F. Dohmann and Ch. Hartl. Tube hydroforming - research and practical application. *Journal of Materials Processing Technology*, 71:174–186, 1997.

[14] M. Ahmetoglu and T. Altan. Tube hydroforming: State-of-the-art and future trends. *Journal of Materials Processing Technology*, 98:25–33, 2000.

[15] B. R. Gardner. The Business Case for the Use of Hot Metal Gas Forming. *http://archive.metalformingmagazine.com/2001/10/HotMetal.pdf*, 35:10, 2001.

[16] B. Dykstra. Hot Metal Gas Forming for Manufacturing Vehicle Structural Components. *Poly Eng Sci*, 35:9, 2009.

[17] H. Singh. *Fundamentals of hydroforming.* Society of Manufacturing Engineers, 2003.

[18] W. Rimkus, H. Bauer, and M. J. A. Mihsein. Design of load-curves for hydroforming applications. *Journal of Materials Processing Technology*, 108:97–105, 2000.

[19] C. A. Taylor, Delorenzi H, G, and D. O. Kazmer. Experimental and Numerical Investigations of the Vacuum-Forming Process. *Polymer Engineering and Science*, 32:1163–1173, 1992.

[20] K. Chung. Finite Element Simulation of PET Stretch/Blow-Molding Process. *Journal of Material Shaping Technology*, 7:229–239, 1989.

[21] J. Pipan and F. Kosel. Numerical simulation of rotational symmetric tube bulging with inside pressure and axial compression. *International Journal of Mechanical Sciences*, 44:645–664, 2002.

[22] A. Cherouat, K. Saanouni, and Y. Hammi. Numerical improvement of thin tubes hydroforming with respect to ductile damage. *International Journal of Mechanical Sciences*, 44:2427–2446, 2002.

[23] H. L. Xing and A. Makinouchi. Numerical analysis and design for tubular hydroforming. *International Journal of Mechanical Sciences*, 43:1009–1026, 2001.

[24] M. Mooney. Theory of Large Elastic Deformations. *Journal of Applied Physics*, 11:582–592, 1940.

[25] R. W. Ogden. Large Deformation Isotropic Elasticity - on the Correlation of Theory and Experiment for Incompressible Rubberlike Solids. *Proc. Roy. Soc. London*, A326:565–584, 1972.

[26] J. S. Bergstrom, S. M. Kurtz, C. M. Rimnac, and A. A. Edidin. Constitutive modeling of ultra-high molecular weight polyethylene under large-deformation and cyclic loading cohditions. *Biomaterials*, 23:2329–2343, 2002.

[27] J. S. Bergstrom, C. M. Rimnac, and S. M. Kurtz. Prediction of multiaxial mechanical behavior for conventional and highly crosslinked UHMWPE using a hybrid constitutive model. *Biomaterials*, 24:1365–1380, 2003.

[28] J. S. Bergstrom, C. M. Rimnac, and S. M. Kurtz. An augmented hybrid constitutive model for simulation of unloading and cyclic loading behavior of conventional and highly crosslinked UHMWPE. *Biomaterials*, 25:2171–2178, 2004.

[29] Hibbitt and Karlsson and Sorensen, Inc. *ABAQUS User's Manual.* `http://www.abaqus.com`, 2004.

[30] K. Manabe and M. Amino. Effect of process parameters and material properties on deformation process in tube hydroforming. *Journal of Material Processing Technology*, 123:285–291, 2002.

[31] F. Vollertsen and M. Plancak. On possibilities for the determination of the coefficient of friction in hydroforming of tubes. *Journal of Materials Processing Technology*, 125-126:412–420, 2002.

[32] P.Ray and B. MacDonald. Experimental study and finite element analysis of simple X- and T-branch tube hydroforming processes. *International Journal of Mechanical Sciences*, 47:1498–1518, 2005.

[33] J. L Throne. *Technology of Thermoforming.* Hanser Publishers, Munich Vienna New York, 1996.

[34] K. Kouba, O. Bartos, and J. Vlachopoulos. Computer simulation of thermoforming in complex shapes. *Polymer Engineering and Science*, 32:699–704, 1992.

[35] B. Koziey, J. Pocher, J. J. Tian, and J. Vlachopoulos. New results in finite element analysis of thermoforming. *Annual Technical Conference - ANTEC, Conference Proceedings*, 1:714–719, 1997.

[36] F. Erchiqui, A. Gakwaya, and M. Rachik. Dynamic Finite Element Analysis of Nonlinear Isotropic Hyperelastic and Viscoelastic Materials for Thermoforming Applications. *Polymer Engineering and Science*, 45:125–134, 2005.

[37] E. D. George Jr., G. A. Haduch, and S. Jordan. The integration of analysis and testing for the simulation of the response of hyperelastic materials. *Finite Elements in Analysis and Design*, 4:19–42, 1988.

[38] G. A. Holzapfel. On large strain viscoelasticity: continuum formulation and finite element applications to elastomeric structures. *International Journal for Numerical Methods in Engineering*, 39:3903–3926, 1996.

[39] D. A. Nutter. Comparing actual injection blowmolded parts to computer generated injection blowmolded parts. *Annual Technical Conference - ANTEC, Conference Proceedings*, 3:3544–3547, 1994.

[40] E. M. Arruda and M. C. Boyce. A three-dimensional constitutive model for the large stretch behavior of rubber elastic materials. *Journal of the Mechanics and Physics of Solids*, 41:389–412, 1993.

[41] M. Levy. C. r. hebd seance acad. sci. *J. Math. pures appl*, 16:369–372, 1871.

[42] R. Von Mises. Nachr ges wiss gottingen. *Z. angew. Math. Mech.*, 8:161–185, 1928.

[43] W. F. Hosford. *Mechanical Behavior of Materials.* Cambridge University Press, 2005.

[44] S. M. Kurtz, L. Pruitt, C. W. Jewett, R. P. Crawford, D. J. Crane, and A. A. Edidin. The yielding, plastic flow, and fracture behavior of ultra-high molecular weight polyethylene used in total joint replacements. *Biomaterials*, 19:1989–2003, 1998.

[45] E. M. Arruda and M. C. Boyce. Evolution of plastic anisotropy in amorphous polymers during finite straining. *Int J Plast*, 9:697–720, 1993.

[46] M. C. Boyce, A. S. Argon, and D. M. Parks. Mechanical properties of compliant particles effective in toughening glassy polymers. *Polymer*, 28:1680–1694, 1987.

[47] M. C. Boyce, D. M. Parks, and A. S. Argon. Large inelastic deformation of glassy polymers, Part I: rate-dependent constitutive model. *Mech Mater*, 7:15–33, 1988.

[48] E. M. Arruda and M. C. Boyce. Effects of strain rate, temperature and thermo-mechanical coupling on the finite strain deformation of glassy polymers. *Mech Mater*, 19:193–212, 1995.

[49] O. A. Hasan and M. C. Boyce. A constitutive model for the nonlinear viscoplastic behavior of glassy polymers. *Poly Eng Sci*, 35:331–344, 1995.

[50] J. S. Bergstrom and M. C. Boyce. Constitutive modelling of the large strain time-dependent behavior of elastomers. *J Mech Phys Solids*, 46:931–954, 1998.

[51] J. B. Yang, B. H. Jeon, and S. I. Oh. Design sensitivity analysis and optimization of the hydroforming process. *Journal of material processing technology*, 113:666–672, 2001.

[52] G. Gavrilidou and J. Mukesh. FEA and Multivariate Statistical Data Analysis of Polypropylene Tube Forming Process. *NUMISHEET 2005: Proceedings of the 6th International Conference and Workshop on Numerical Simulation of 3D Sheet Metal Forming Process.*, 778:162–166, 2005.

[53] I. Axinte. *Finite Element Analysis of the Deformation of a Rubber Diaphragm.* PhD thesis, Department of Engineering Science and Mechanics, Virginia Polytechnic Institute and State University, VA, USA, 2001.

[54] K. J. Bathe. *Finite Element Procedures.* Prentice Hall, 1996.

[55] O. C. Zienkiewcz. *The Finite Element Method.* McGraw-Hill, 1982.

[56] J. Bergstrom. *Personal Communication.* e-mail, 2005-2007.

Appendix

A Material Property Tests

A1 Sample Dimensions

Tensile samples were cut and machined in the Engineering machine shop at McMaster. Tensile sample type V with the smallest dimensions according to D638-03 was chosen as a better fit for the purpose of experiments (Figure A1). Below is a graphical representation of the tensile sample.

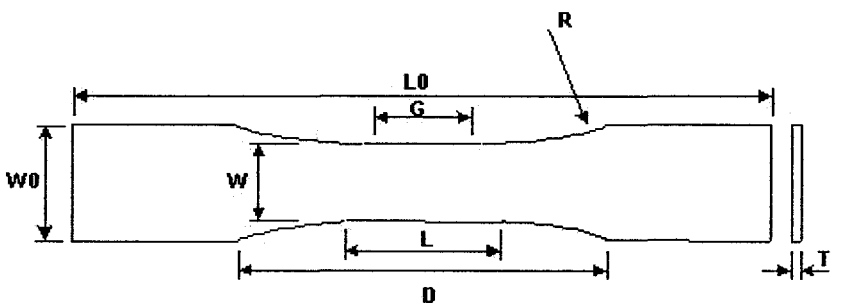

Figure A1: Tensile sample type V

All dimensions are in *mm* as well as in *inches* with acceptable tolerances. Sample dimensions and tolerances are shown in Table A1. Tensile samples were machined along the length of the tube. The thickness of the tensile sample was kept the same as initial tubular material wall thickness.

Dimensions	**Type V**	**Tolerances**
W - width of narrow section	3.18 [0.125]	±0.5 [±0.02]
L - length of narrow section	9.53 [0.375]	±0.5 [±0.02]
W0 - width overall	9.53 [0.375]	+3.18 [+0.125]
L0 - length overall	63.5 [2.5]	no max
G - gage length	7.62 [0.300]	±0.25 [±0.010]
D - distance between grips	25.4 [1.0]	±5 [±0.2]
R - radius of fillet	121.7 [0.5]	±1 [±0.04]
T - thickness	3.175 [0.13]	±0.4 [±0.02]

Table A1: Tensile sample dimensions

A2 Engineering Strain Calculations

As it was mentioned in Chapter 4, specific procedure was employed to determine engineering strain. It would be inaccurate to calculate engineering strain form the displacement of grips. Although the samples were clamped right at the end of specimen's shoulder, slightly non-uniform width of the shoulder (dL) could result in significant error in the calculation of engineering strain (Figure A2).

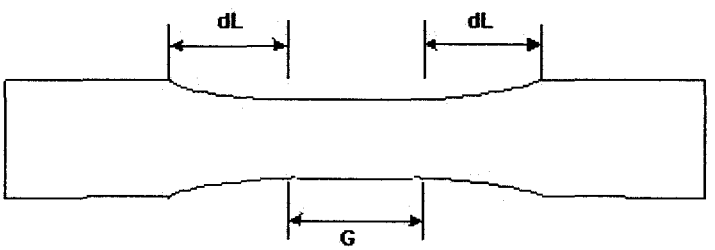

Figure A2: Gage length G and shoulders dL of tensile sample

For this purpose, tensile samples were marked at a specific gage length before deformation using a permanent marker. After deformation, marked gage length elongation was measured. Final gage length elongation was compared with the grips displacement measured by acquisition system. Discrepancy between final gage length elongation and displacement of the grips introduced non-uniform elongation of the sample's shoulder. Discrepancy between measurements was evenly distributed between data points to account for the samples non-uniform width.

B Part Thickness Variation Along the Length

Repeat measurements of the tube wall thickness distribution was performed with a standard micrometer. Deformed tubes were cut in longitudinal direction and wall thickness was measured at several points along the length of the tube. Accuracy of the results in this case was affected by measurement imperfections. Due to the possible measurement errors, tubes were measured 3 times and standard deviation (STD) was calculated. Mean value of the measurement sets was taken as a representation of the final thickness distribution. Standard deviation of all cases is shown in Figure B1.

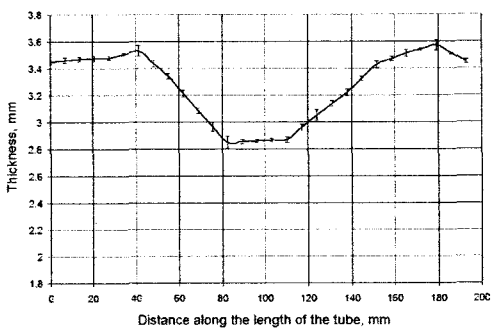

(a) Case 1

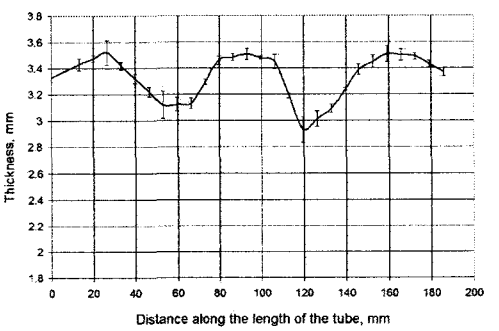

(b) Case 2

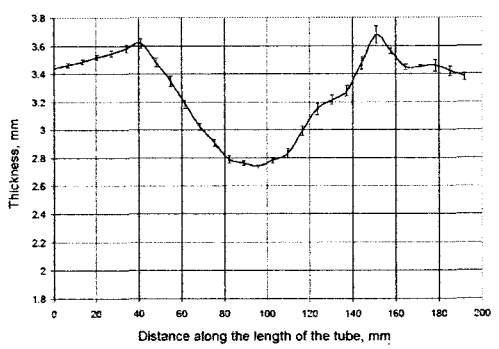

(c) Case 3

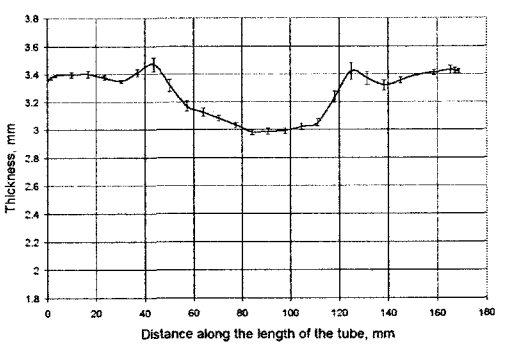

(d) Case 4

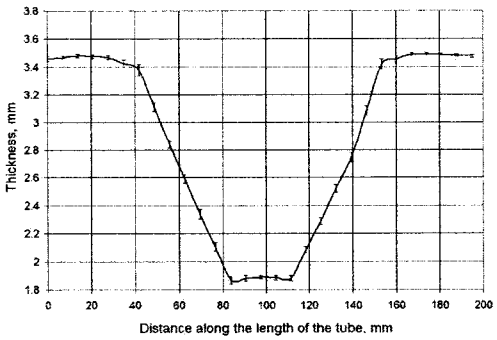

(e) Case 5

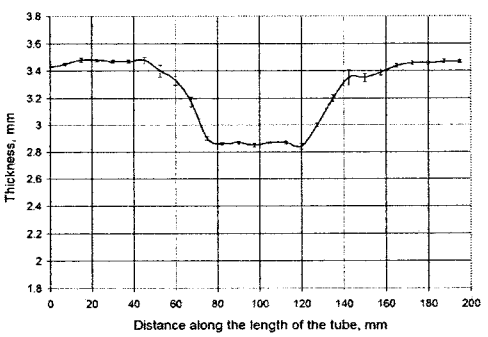

(f) Case 6

Figure B1: Relative measurement error and STD

C Material Models Input Data

Material coefficients for Ogden and AHM material models are presented in sections C1 and C2 respectively.

C1 Material Coefficients for Ogden Model

Ogden material model coefficients were determined by experimental tensile stress-strain data calibration in Abaqus/Explicit software. Ogden material model coefficients for N=3 are presented in Figure C1.

HYPERELASTICITY - OGDEN STRAIN ENERGY FUNCTION WITH N = 3

I	MU_I	ALPHA_I	D_I
1	-23.5255251	2.00024294	0.00000000
2	4.19099015	4.00006825	0.00000000
3	38.4766926	-1.99915593	0.00000000

Figure C1: Ogden material model coefficients

C2 VUMAT Coefficients for AHM

User material (VUMAT) subroutine was obtained directly from Dr. Bergstrom of Exponent Inc. Dr. Bergstrom is the developer of the AHM material model. Coefficients of the constitutive model are intended to describe material response as close as possible. Larger number of coefficients generally results in a better material description. AHM material model utilizes 30 coefficients in Abaqus. They account for viscoelastic-viscoplastic material properties. Coefficients used in the AHM material

model are described in Table C1. Flags explanation is presented in Figure C2. The values of some of the coefficients were obtained by fitting experimental stress-strain curve to AHM material model equations by Dr. Bergstrom using a special purpose program.

Coefficient	**Description**	**Value**
Flags *	UMAT Flags	4010
alpha	Coefficient of thermal expansion	0
T0	Reference temperature	373.15
effMu	Effective Shear modulus	500
EffKappa	Effective Bulk modulus	4000
rTol	Relative error tolerance, used by ODEPACK	1e-06
aTol	Absolute error tolerance, used by ODEPACK	1e-08
**** Network E spring ****		
Ee0	Young's modulus of Network E	48.4118
dEdT	Change in modulus with temperature	0
nuE	Poisson's ratio of network E	0.4
**** Network A spring ****		
muA0	Shear modulus	1.04128
dMuAdT	Change in shear modulus with temperature	0
lamLockA	Chain locking stretch	10
kappaA	Bulk modulus	1000
qA	I2 scaling factor	0.146

**** Network B spring ****		
sB0	Initial scaling factor	29.1701
sB1	Final scaling factor	3.65001
pB	Rate of change of sB	9.31249
**** Network B dashpot ****		
tauBasB0	Initial flow resistance of network B	72.2924
tauBasB1	Final flow resistance of network B	14.8767
aBasB	Transition rate of flow resistance of network B	7.97952
mB	Stress exponent of network B	3.16623
TBdouble	Temperature increase to double flow rate	1e+09
**** Network C dashpot ****		
tauBasC0	Initial flow resistance of network C	11.4641
tauBasC1	Final flow resistance of network C	7.11241
aBasC	Transition rate of flow resistance of network C	7.21219
mC	Stress exponent of network C	5.38639
TCdouble	Temperature increase to double flow rate	1e+09
**** Damage evolution ****		
damD0	Damage evolution pre-factor	290
damA	Damage evolution factor	4.1

Table C1: AHM material model coefficients

```
* flags = abcd (a 4 digit integer)

    a: ODE solve method
        0: explicit Euler
        1: RK4
        2: lsode10 (non-stiff)
        3: lsode22 (stiff)
        4: lsoda (automatic stiff - nonstiff)

    b: calcJ (how to calculate the Jacobian)
        0: don't calculate Jacobian
        1: elastic Jacobian
        2: small symmetric approximate Jacobian
        3: full symmetric approximate Jacobian
        4: full unsymmetric Jacobina

    c: errRm (error recovery method)
        1: print error message and crash
        2: try to fix the problem and continue
        3: exit to the main procedure and set pnewdt = 0.5
        9: quit after the umat finishes its first calculation

    d: verb (verbosity level of debug messages)
        0 : no messages
        1 : umat (in & out)
        2 : umat (summary of calculation results)
        3 : all functions (in & out)
        4 : all detail
```

Figure C2: Flags description